Dipl.-Ing. Dipl.-Ing. Peter Loidolt BSc

Modeling of Powder Compaction

DOCTORAL THESIS

to achieve the university degree of

“Doktor der technischen Wissenschaften”

submitted to

Graz University of Technology

Supervisor

Univ.-Prof. Dipl.-Ing. Dr.techn. Johannes G. Khinast

Institute for Process and Particle Engineering

Graz, September 2018

AFFIDAVIT

I declare that I have authored this thesis independently, that I have not used other than the declared sources/resources, and that I have explicitly indicated all material which has been quoted either literally or by content from the sources used. The text document uploaded to TUGRAZonline is identical to the present doctoral thesis.

Date

Signature

To my family

Ich habe keine besondere Begabung, sondern bin nur leidenschaftlich neugierig.

Albert Einstein

CONTENTS

ABSTRACT

In this thesis powder compaction is modeled by means of two different particle-based methods. The discrete element method in this work is used to model the filling behavior of powder during the dosator process. In this process the powder is mainly compacted due to rearrangement of the particles. Cohesive powders form loose packed powder beds which are far more compressed during processing compared to free-flowing powder which results in a different qualitative filling behavior.

The multi-particle finite element method is used to model powder compaction with deformable spherical particles which are compacted up to a relative density of 0.95. The high computational costs of this method are reduced by introducing an efficient representative volume element which allows to compute the homogenized stress and strain of a small sample of compacted powder. Based on the stress and the strain it is possible to determine the mechanical properties such as the elastic constants and the yield strength of the compacted powder. An extensive parameter study demonstrates the convergence behavior of the model with respect to the mesh fineness and the number of particles in the representative volume element as well as the time step size and the mass scaling of the explicit solver. A second parameter study is performed to describe the mechanical properties of the powder as function of the contact cohesion strength, the strain path and the relative density.

The contact cohesion is important to get a solid material and it governs the mechanical properties for tension load. The anisotropy of the mechanical properties is correlated with the anisotropy of the strain path. The elastic constants and the yield strength increase with the relative density of the powder. Analytical regression curves are defined which correlate the model parameters and the mechanical properties. In this way it is possible to describe the continuous distribution of the material properties in a macroscopic model of a heterogeneous deformed part.

KURZFASSUNG

In dieser Arbeit wird Pulverkompaktierung mit zwei partikelbasierte Methoden modelliert.

Die Diskrete-Elemente-Methode wird verwendet um den Dosator Prozess zu modellieren, bei welchem das Pulver hauptsächlich durch Umordnung der Partikel kompaktiert wird. Dabei bilden kohäsive Pulver lose Pulverpackungen, welche während des Prozesses wesentlich stärker komprimiert werden als freifließende Pulver und wodurch sich ein qualitativ unterschiedliches Füllverhalten ergibt.

Die Multi-Partikel-Finite-Elemente-Methode wird zur Modellierung von Pulverkompaktierung verformbarer, kugelförmiger Partikel verwendet, die zu einer relativen Dichte von maximal 0.95 kompaktiert werden. Der hohe Rechenaufwand dieser Methode wird durch ein effizientes repräsentatives Volumenelement reduziert, welches die homogenisierte Spannung und Dehnung einer kleinen Probe berechnet. Darauf basierend können mechanische Eigenschaften wie die Elastizitätskonstanten und die Fließfestigkeit des Pulvers bestimmt werden. Um das Konvergenzverhalten des Modells bezüglich der Netzfeinheit und Anzahl der Partikel sowie des Zeitschrittes und der Massenskalierung des expliziten Lösers zu demonstrieren wird eine umfassende Parameterstudie durchgeführt. In einer weiteren Parameterstudie werden die mechanischen Eigenschaften als Funktion der Kontaktkohäsion, des Dehnungspfades und der relativen Dichte bestimmt.

Die Kontaktkohäsion wird für die Modellierung eines festen Materials benötigt und ist für die mechanischen Eigenschaften unter Zugbelastung entscheidend. Die Anisotropie der mechanischen Eigenschaften korreliert mit der Anisotropie des Dehnungspfades. Die Zahlenwerte der mechanischen Eigenschaften nehmen mit der relativen Dichte des Pulvers zu. Analytische Regressionskurven geben den Zusammenhang zwischen Modellparametern und mechanischen Eigenschaften an, wodurch kontinuierliche Verteilungen von mechanischen Eigenschaften in heterogen verformten Bauteilen beschrieben werden können.

ACKNOWLEDGEMENT

I want to thank Prof. Johannes Khinast who was the supervisor of this thesis. He gave me the great opportunity to explore a very interesting topic during the last years. He supported me during the painful process of scientific publishing and encouraged me during setbacks.

I also want to thank Prof. Manfred Ulz for the scientific discussion and his input during publishing. His alternative view helped me to improve the quality of my work.

I have enjoyed the work at the Institute for Process and Particle Engineering and I want to thank all my colleagues for the relaxed atmosphere and the obligatory coffee breaks. Special thanks go to all my students I had the honor to supervise during the last years. In particular, I want to mention my master students Andreas Bramböck, Stefan Madlmeir, Daniela Fiedler and Andreas Kottlan. They inspired me during long discussions and I enjoyed to work with them in a team.

Finally, I want to thank my family and all who supported me during my whole education starting from elementary school up to my PhD.

Peter Loidolt

Graz, September 2018

1 Introduction

The thesis at hand consists of three self-contained papers which are presented in sections 2 to 4. This introduction gives a motivation of these three papers which all deal with modeling powder compaction. Compaction of powder is an important issue during processing of bulk materials. During compaction the bulk density of the powder increases, while the flowability decreases. This may be disadvantageous in some cases as for example compacted powder inside a hopper can inhibit hopper outflow. On the other hand, in some cases highly compacted powder is desired e.g. during tableting, during production of green bodies before sintering or during production of food or fuel pellets.

To get a basic idea about powder compaction we have a look at the compaction of powder in a container (see Figure 1). Starting from a loose packing in picture (A) the particles are settled due to gravity in (B) and (C). The packing density of the particles inside the container after settling depends on the size and shape of the particles and the interaction forces between the particles as it is discussed in section 2 of this thesis. After settling a lid is inserted at the top of the container and starts to compress the powder in (D). Depending on the initial packing density of the powder, densification first takes place solely by rearrangement of the particles inside the powder. At some point particles are not able to rearrange anymore and they start to deform to allow more compaction as it is shown in (E) and (F). The change of the color from blue to red describes the increasing local stress inside the particles. If the particles are compressed further, then the shape of the particles changes dramatically as can be seen in (G) to (I). Depending on the material properties the particles can deform plastically as it is shown in Figure 1 or they can break in case of a brittle material.

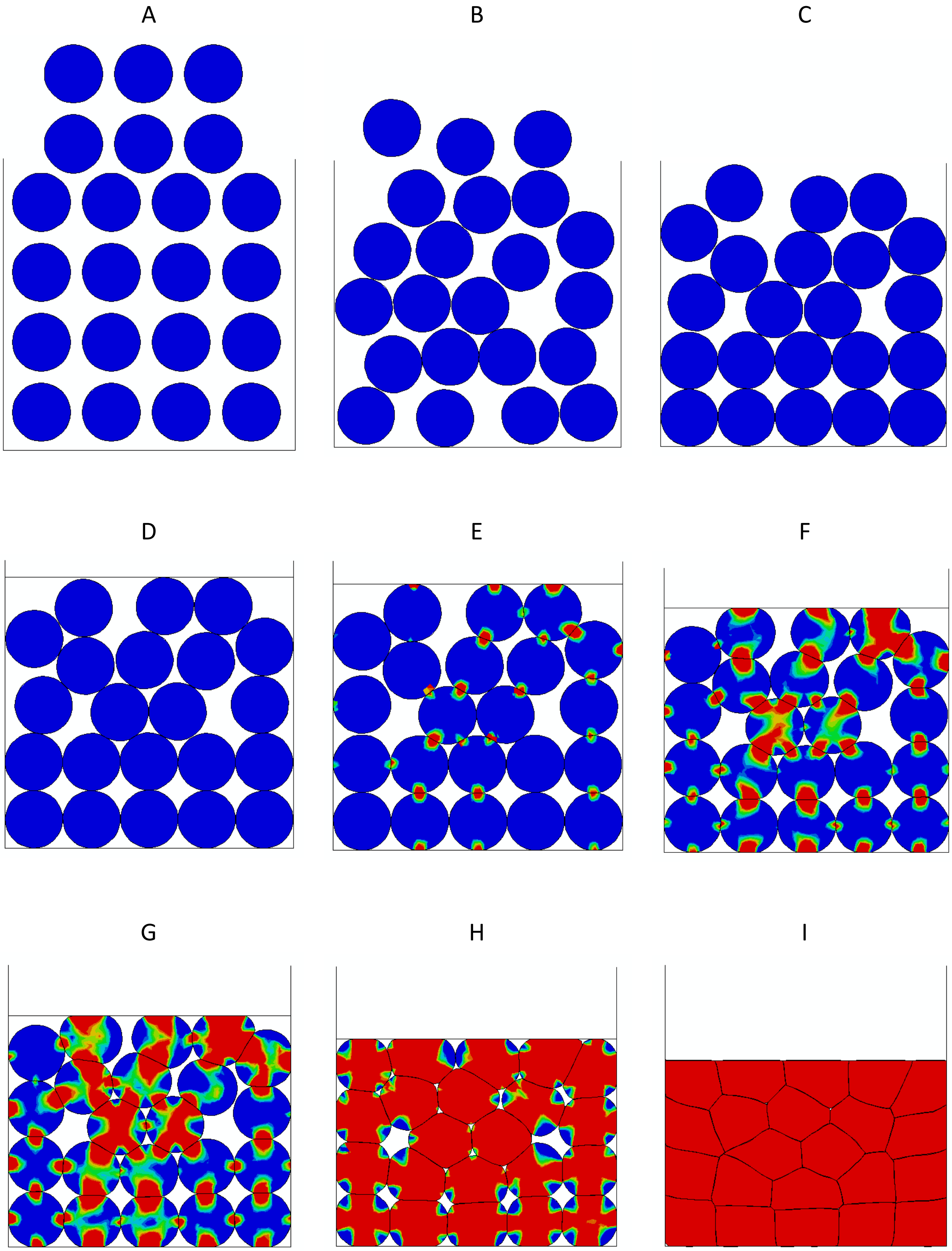

Figure 1: Compaction of powder inside a container

Based on the observations in Figure 1 the two different approaches considered in this thesis are justified:

If the forces acting on the particles are low and the particles are only slightly deformed as it is shown in Figure 1 (A) to (E) then the discrete element method DEM can be used to model the flow behavior of the powder. DEM is a very efficient method to model a high number of particles and to track their position during powder processing. In section 2 the DEM method is used to model the dosator filling process with up to 3.5 million particles. During the dosator process the powder is compacted only slightly to obtain a stable powder plug which is filled into a capsule.

If the forces acting on the particles are very high as it can be seen in Figure 1 (F) to (I) then the change of the particle shape and the formation of contact area have to be considered in the model. In section 3 and 4 of this thesis the multi-particle finite element method MPFEM is used to model the compaction of powders for high packing densities. With this method the deformation of each particle is considered in addition to the interaction of the particles. The drawback of this method is the high computational effort which limits the number of particles in the model to several hundreds. In contrast to the illustrated process in Figure 1 with a low number of particles , to describe real processes it is necessary to model millions or even billions of particles.

Since it is impossible to model a real process considering all relevant microstructural properties of the powder, the powder is described preferentially as a continuum during powder compaction. The transition from a micromechanical model to a continuum model is called homogenization and is shown in Figure 2. In the homogenized model no single particles are considered and the material is smeared out over the whole volume of the powder part (see Figure 2 right).

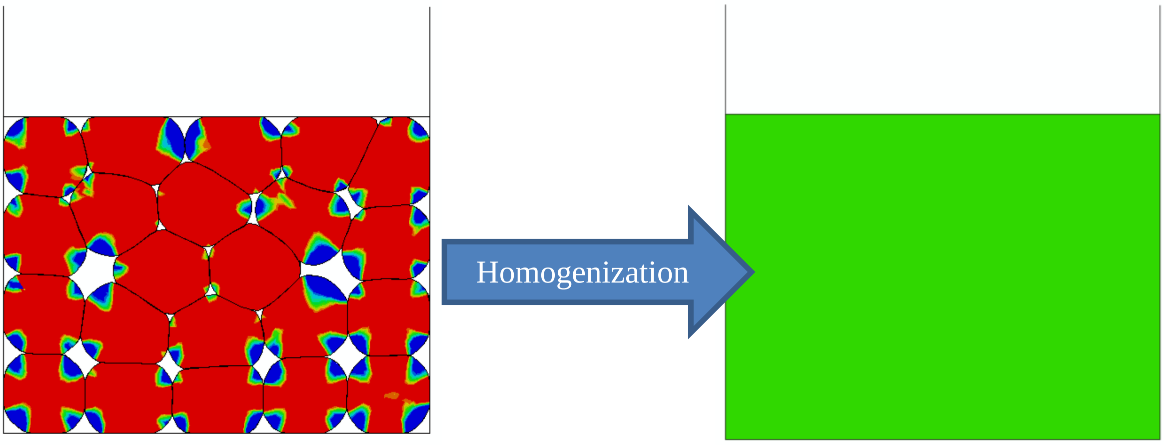

Figure 2: Transition from a micromechanical model to a continuum model

To describe the deformation and a possible failure of the compacted powder in a continuum model it is necessary to have a suitable material model including several mechanical material properties. At low stresses the powder deforms elastically (after unloading the compacted powder returns in its initial shape). The respective elasticity model requires two independent elasticity constants at minimum in case of an isotropic material and up to 21 constants for a general anisotropic material [1]. If the stress exceeds the yield stress of the powder, then the powder deforms plastically (after unloading the compacted powder does not return in its initial shape). To be able to describe yielding of powder for general load cases it is necessary to define a yield surface. Among others, the Drucker-Prager/Cap model is one of the most used models for describing the yield surface of powders [2]. All material parameters needed for a continuum model of a powder are usually found during diverse experimental tests of the compacted powder. The drawback of experiments is that they are very laborious since many samples are necessary as the material properties of the powder change dramatically during compaction. At the beginning of the compaction the powder is free flowing while it is completely solid after compaction. Furthermore, experiments give only limited insight into the physics of the process and the gain of process understanding is therefore limited. Hence, the representative volume element RVE of deformable particles is introduced in section 3. The RVE is useful to determine the mechanical properties based on a micromechanical model consisting of a low number of particles. In this way it is possible to apply the knowledge gained from a micromechanical model to a macroscopic model of a compacted powder part.

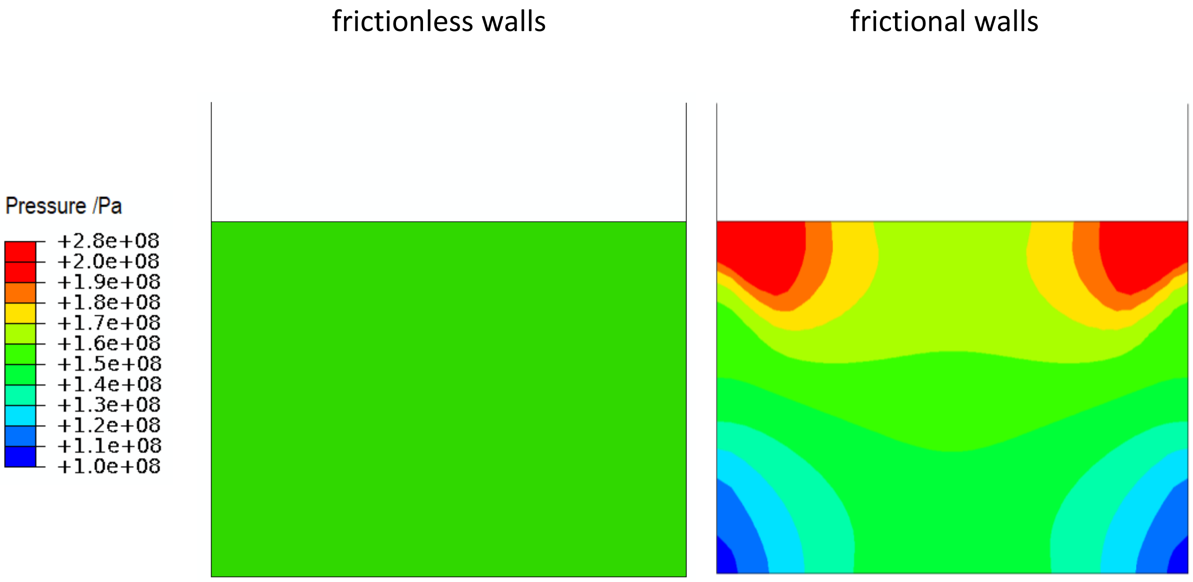

Figure 3: Pressure distribution inside a container with frictionless and frictional walls

Another important issue of powder modeling is the sensitivity of the powder properties to the compaction conditions of the powder. Unfortunately, the compaction conditions cannot be assumed to be uniform for a real powder part as can be seen for the pressure distribution in Figure 3 right. Furthermore, it is supposed to have anisotropic material properties in case of anisotropic compaction conditions. As the powder in Figure 1 is just compressed in one vertical direction it is likely to have different material properties in vertical and horizontal direction. This issue is addressed in section 4 where the powder properties are determined for different compaction conditions.

2 Mechanistic Modeling of a Capsule Filling Process[a]

Abstract: Filling a dosator nozzle moving into a powder bed was investigated using the Discrete Element Method (DEM). Various particle diameters and contact properties were modeled. The simulations qualitatively showed the influence of powder properties on the amount of dosed powder. Two factors that influence the dosed mass were observed. First, the ratio between the particle and dosator diameters affects the packing of particles inside the dosator chamber. Second, the flow behavior of the powder significantly modifies its filling and compression behavior. Cohesive powders pack less densely inside the powder bed, which could lead to a lower amount of dosed powder. In contrast, cohesive powders are compressed more during dosing and the density inside the dosator chamber increases during the dosing process. Since the simulation of fine cohesive powders is numerically impossible due to a high number of particles and small simulation time steps, we applied a simple method for particle scaling to acquire a qualitative understanding of the filling behavior of coarse and fine powders.

2.1 Introduction

Hard capsules are next to tablets one of the most commonly used and prescribed oral dosage forms and were first introduced in the 19th century. The capsule is filled with powder or with pellets made by the extrusion and spheronization. Capsules offer several advantages, including a reduction of excipients needed to achieve a designed pharmacokinetic profile. According to regulatory requirements, based on the needs and safety of patients, the content of capsules, i.e., the fill weight, needs to be constant within a certain narrow tolerance region. Moreover, content uniformity has to be ensured, i.e., segregation prior to the capsule filling step needs to be

---

[a] This section is based on the journal article “Mechanistic modeling of a capsule filling process” by Loidolt et al. in International Journal of Pharmaceutics 2017

excluded. Fill weight variability and content uniformity are therefore considered critical quality attributes (CQAs) within the Quality-by-Design (QbD) framework. [3]

In the industry, several capsule filling techniques have been used over the last decades. These include tamping and dosator systems for hard-gelatin capsules [4]. In addition, for low-dose capsules vacuum-roll techniques and vibration-based pepper-shaker systems are being used [5–7]. In this study, dosator systems are considered. In a typical filling cycle, first a cylindrical (hollow) dosator nozzle plunges into an un-compacted powder bed stored in a rotating bowl (which is periodically refilled). The nozzle vertically dips into the powder bed until it reaches a prescribed minimum distance from the bottom. During this step, the powder enters the nozzle and is compressed to a predefined degree. Subsequently, the filled nozzle is lifted and removed from the powder bed. The nozzle is then placed on top of an empty capsule body and the powder is ejected into the capsule, after which the cap is placed onto the capsule body. A detailed review of the process is provided in [8]. To prevent powder dropping from the nozzle before the powder is ejected into the capsule, a minimum stability of the powder plug inside the dosator chamber is required. Thus, the powder needs to be (lightly) compressed during the dipping step. In order to be able to control compression a moveable piston inside the dosator nozzle can enhance compression. The minimal compression stress is investigated in [9]. However, the powder plug needs to be loose enough to allow rapid disintegration upon delivery, e.g., in case of capsules made for dry powder inhalers (DPIs). [10]

The filling volume of the nozzle is defined by its inner diameter and an adjustable piston, which defines the length of dosator chamber. Since the volume of the chamber is exactly defined, this method is a volumetric dosing method. However, the critical quality attributes (CQA) of capsules are fill weight and fill weight variability. Thus, a constant fill weight is only achieved if the powder density is known and constant. Unfortunately, the density of a powder is highly variable and a strong function of many effects, including processing history, material properties, environmental conditions (such as humidity and vibrations) and the process parameters during compression. Even the surface texture of the dosator tools has to be considered as it is shown in [11]. Hence, controlling the final dosage mass is one of the biggest challenges associated with capsule filling processes, including dosator filling.

The influence of powder properties and process parameters on the capsule fill weight has been investigated experimentally by many groups (Patel and Podczeck, 1996; Podczeck and Newton, 1999; Podczeck and Newton, 2000; Pinzon, 2012; Llusa et al., 2013 and Faulhammer et al., 2014b). Evidently, the densification of powder during the dipping step increases with powder compressibility and poorer flowability (leading to higher Hausner ratios). Moreover, the plug density is increased by the precompression ratio. The precompression ratio is defined as the ratio between the powder bed height and the dosator chamber length. The influence of the dosing speed is rather complex, since an increasing dosing speed leads to a higher rotational speed of the dosator machine, causing densification of the powder bed due to machine vibrations and other forces. In addition, the dosator nozzle dipping speed increases, and it is unclear, whether the influence of dosing speed is due to the densification of the powder bed or to the increased dipping speed of the nozzle. Likely, for different powders different effects are dominating. This example shows how difficult it is to acquire a full mechanistic understanding of the process via experiments alone. Lastly, the state of the powder bed in the bowl is unknown during industrial capsule filling. Depending on the capsule filling speed a few hundred to a several hundred thousand dipping events occur per hour, affecting the consistency of the powder bed. Although there are measures taken in a capsule filling machine to homogenize the powder and to sample from non-identical locations, the powder cannot *a priori* be assumed to be homogeneous. A homogeneous state of the powder in the bowl may be achieved only for materials with very good flowability (which in turn show a tendency to segregate). Nevertheless, no standard process-analytical tools are available to analyze the state of the powder in the bowl. [5]

Numerous experimental studies focused on linking material properties and process parameters to the critical quality attributes of capsules, i.e., average fill weight and fill weight variability, as for example [3]. In contrast, modeling and simulation studies of the dosator capsule-filling process are rare. However, there are numerous groups working with simulation tools to describe other powder-based processes. For example, there are numerously simulation studies published dealing with die filling prior to compaction of tablets or the production of green bodies [16–18]. Similar to the dosator process, during die filling a fixed volume is filled with particles. Particles fall into the cavity due to gravity during die filling, and therefore, it is not directly comparable to the dosator process. Nevertheless, a constant filling mass is crucial for both processes. Another related process is the coil feeding process which can also be used for dosing. A coil feeder with cohesive powder was investigated with the discrete element method by [19].

As mentioned above, a mechanistic modeling of the dosator process itself has not been reported so far. However, a theoretical consideration of the dosator process can be found in [20]. This work deals with the retention of the powder inside the nozzle. It shows, that the interaction of the powder and the wall material is important for the capsule filling ability of powders. A phenomenological model proposed by [21] takes precompression densification and compression density into account. However, a deeper mechanistic understanding of the process is required. [22] simulated the packing behavior of various pellet shapes inside a hard capsule using a Monte Carlo method. This study was enhanced by [23]. Although the results are not directly applicable to the dosing process, as they do not involve the movement of piston inside a powder, they describe how particle size and shape influence packing inside a closed chamber. In the current study, the dosator capsule-filling process is studied using a mechanistic modeling tool. Specifically, the Discrete Element Method (DEM) is applied in this work. This method offers the opportunity to freely modify powder properties and to observe quantities that are not measurable experimentally. As such, it is a great complementary tool to experiments.

Nevertheless, many simplifications are required to set up a simulation that can be run within a reasonable time and thus, modeling of the filling process is only a first step towards the rational design of capsule filling processes.

2.2 Methods

In our study, the discrete element method DEM introduced by Cundall and Strack [24] was used to investigate the filling of a dosator nozzle. This method relies on the soft-sphere approach, with particles represented as (overlapping) spheres. The contact forces between two particles in the normal and tangential directions are computed as a function of the particle overlap. The contact law comprises the functional relationship between the particle overlap and the contact force and is the core of the DEM model. The particle position and velocity are computed at every simulation time step by solving Newton's second law. Since particle rotation in dense packed beds considered here is of minor importance the particle rotation is not considered in the simulation. This way, the position of every particle in the powder is tracked during the entire simulation. The open source DEM software LIGGGHTS® [25] was used for that purpose.

2.2.1 Geometric Setup

To simulate the dosator filling process, particles with nominal diameters of 500, 300, 200, 100 and 75 µm were allowed to settle on a fixed base in order to create a powder bed height of 8 mm. Since in DEM no ambient air is considered and particles could accelerate indefinitely, a viscous damping force is applied to get a terminal velocity of 0.1 m/s. Thus, compaction of the powder bed due to unrealistic high impact velocities can be avoided. To limit the computational effort, we only considered a section of the powder bed with a width of 12 mm both in the x- and y-directions (see Figure 4). To compensate for the limited size of the powder bed, the boundaries of the domain were set to be periodic, meaning that a particle leaving one side of the boundary was inserted at the opposite side. This geometrical setup allowed to simulate approximately 3.5 million particles with a nominal diameter of 75 µm. To avoid modeling artifacts due to monodisperse particles a mass-based particle size distribution is used (see Figure 5). A rather narrow distribution is used to avoid additional computational costs due to a high number of small particles. The diameter of the dosator nozzle was chosen to be 3.4 mm, which is a standard diameter also used in the experimental study of [3]. The dosator chamber length was set to 4 mm in all simulations. The distance from the nozzle to the powder bed floor is used to describe the position of the dosator (see Figure 6). In the results part of this work the evolution of the dosator filling is shown as function of the dosator position for different powder properties.

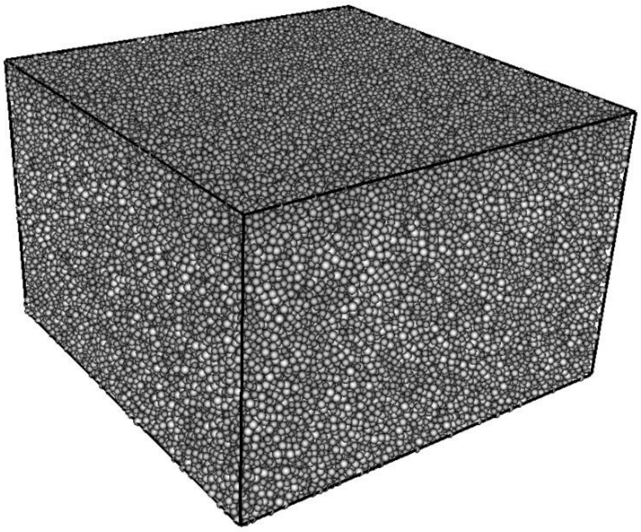

Figure 4:Initial powder bed in the dosator filling simulation. Periodic boundary conditions are used in both horizontal directions.

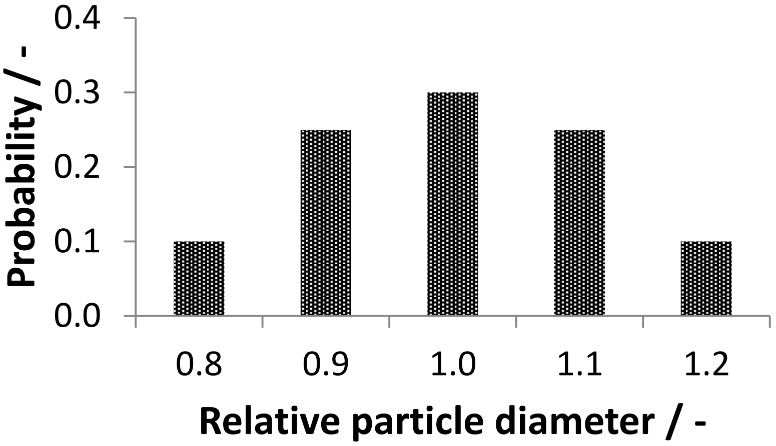

Figure 5: Particle size distribution. The diameters of the five different particle classes are given as fractions of the nominal particle diameter.

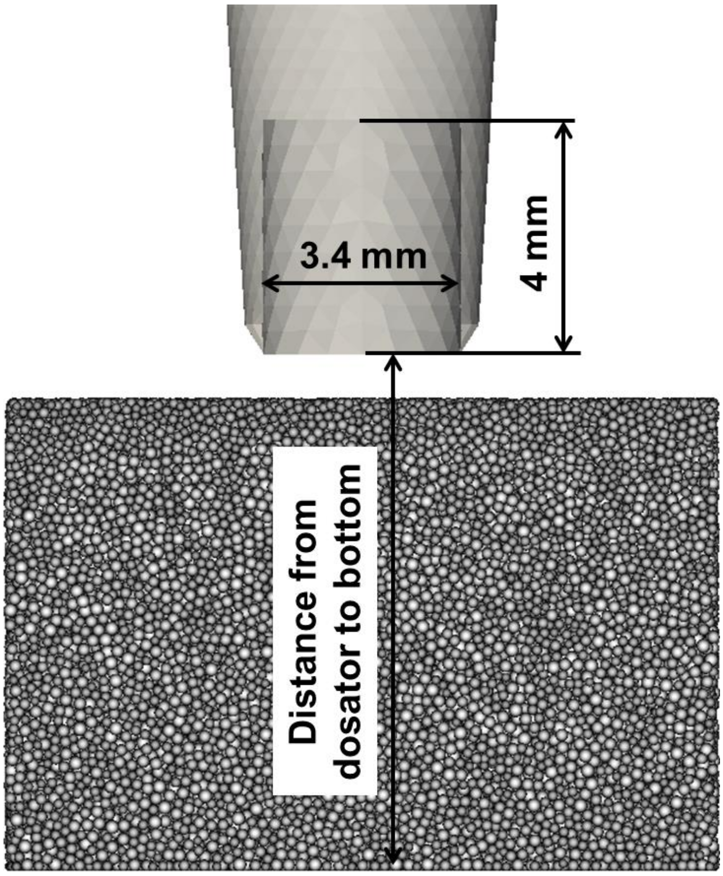

Figure 6: Cross section of the powder bed and the dosator nozzle. The position of the nozzle is given as distance to the powder bed floor.

During simulations, the dosator nozzle moved vertically into the powder bed until it touched the bottom. Since only filling of the nozzle was considered in this study, the simulation was discontinued once this position was reached. During the nozzle movement, the amount of powder and the pressure inside the nozzle were analyzed and plotted as a function of the distance to the bottom. The pressure is defined as one third of the trace of the stress tensor. In the results section the pressure inside the dosator is reported as the volume averaged pressure inside the dosator chamber.

2.2.2 Particle Contact Model

In DEM simulations, the mechanical particle properties have to be defined. In this work, lactose was chosen as a reference material since it is often used in pharmaceutical capsule-filling applications. Accordingly, the particle density was chosen to be 1538 kg/m³. A Poisson ratio of 0.3 and a Young's modulus of 25 MPa were used as elastic constants. To reduce the high contact stiffness and to increase the minimum simulation time step, a low Young's modulus was used rather than the true Young's modulus of lactose of approximately 25 GPa [26], as is typically done in DEM simulations. To determine the effect of this modification on the dosator filling, the Young's modulus was varied in our study.

Material properties are essential for the contact model. The well-known Hertz contact model (a standard model implemented in LIGGGHTS®) was used to compute the contact normal force F_n as a function of the particle normal overlap δ_n, the effective particle radius R^* and the effective Young's modulus E^* as shown in Eq. (1). The tangential contact force is a function of the tangential overlap δ_t and the effective shear modulus G^* and is shown in Eq. (2). It is limited by the Coulomb friction force, which is a function of the coefficient of friction μ_s and the contact normal force. The effective properties can be computed as function of the particle diameter and the elastic constants of the two particles being in contact as it is shown in Eq. (3) to (5). To enable energy dissipation, damping forces in the normal and tangential directions were computed based on the coefficient of restitution e (equations not shown here). More detailed information about the contact model can be found in [27].

$$F_n = \frac{4}{3} E^* \sqrt{R^*} \delta_n^{\frac{3}{2}} \tag{1}$$

$$F_t = \min \begin{cases} 8G^* \sqrt{R^* \delta_n} \delta_t \\ \mu_s F_n \end{cases} \tag{2}$$

$$\frac{1}{E^*} = \frac{1 - {\nu_1}^2}{E_1} + \frac{1 - {\nu_2}^2}{E_2} \tag{3}$$

$$\frac{1}{E^*} = \frac{1 - {\nu_1}^2}{E_1} + \frac{1 - {\nu_2}^2}{E_2} \tag{4}$$

$$\frac{1}{G^*} = \frac{2(2 - \nu_1)(1 + \nu_1)}{E_1} + \frac{2(2 - \nu_2)(1 + \nu_2)}{E_2} \tag{5}$$

To model cohesive powders also cohesion forces have to be included into the contact model. Basically, powders can be considered as cohesive if the attractive cohesion forces between particles or particles and walls are large compared to volume forces of the particles. A dimensionless group that describes the relative effect of cohesion is the Bond number Bo which is defined as the ratio of volume forces and surface forces. In this work it is defined as the ratio of particle gravity force and contact cohesion force (see Eq. (6)). To model powders of different Bond numbers a simple cohesion model was implemented into LIGGGHTS® in addition to the default cohesionless contact model. The cohesion model adds a constant attractive normal force to the contact if two particles touch each other. By adding different cohesion forces to the particle contacts the Bond number can be varied over several orders of magnitude. Consequently, powder properties ranging from free flowing (high Bond number) to very cohesive (low Bond number) can be adjusted irrespective of the particle diameter.

$$\mathrm{Bo} = \frac{\text{volume force}}{\text{surface force}} = \frac{\text{gravity force}}{\text{cohesion force}} = \frac{\frac{d^3 \pi \rho g}{6}}{F_c} \tag{6}$$

In Table 1, the model parameters used for the reference case are summarized. The particle density and the Poisson ratio of lactose are used. The particle diameter and the Young's modulus are chosen to give a compromise between simulation time and quality of the result. For the reference case no cohesion is considered and therefore the Bond number is infinity. All other contact parameters for the reference case are chosen in order to represent the average properties of the four parameter studies outlined below.

Table 1. Model parameters for the reference case

Particle diameter d	200	µm
Particle density ρ	1538	kg/m^3
Young's modulus E	25	MPa
Poisson ratio ν	0.3	-
Coefficient of restitution e	0.45	-
Coefficient of friction (all contacts) μ_s	0.1	-
Bond number Bo	∞	-

In part 1 of this study, the Young's modules is increased by one and two orders of magnitude compared to the reference case. The aim was to check if there are any effects and artefacts caused by the substantially lower stiffness used in the DEM simulation compared to real particle stiffness. In part 2 of this study, the nominal diameter of particles filled into the nozzle is varied in the range from 75 to 500 µm. The objective was twofold: First, we want to investigate the behavior of coarse and fine powders during the dosator filling process. Second, the results should indicate if it is possible to use bigger particles in the simulation than in the real process. If there is no big difference between bigger and smaller particles, then the number of particles in the simulation can be reduced compared to the real systems. Only then simulation of the dosator process would be feasible (in a realistic time scale) since the number of particles in a real system is far too high for the simulation using current computational capacity (up to 10^8 particles with the best codes).

In part 3 of this study the influence of the coefficient of friction is investigated. Based on this simulation additional insight into the process is expected. Especially in regions of high shear rates inside the powder bed or for particles sliding close to the wall of the dosator bed floor the friction behavior may be relevant. In part 4 of the study, powders with different Bond numbers (∞, 0.1, 0.01, 0.001, 0.0001) are compared. A Bond number of infinity describes powders with negligible small particle cohesion forces compared to the particle volume forces. This is the case for dosing of big particles like granules. A bond number of Bo=0.0001 represents fine powders where cohesion forces dominate. For example, during cohesion force measurements of microparticles in [28] a Bond number of 0.0001 was obtained for particle diameters of approximately 10 µm. During studying the range of high to low Bond numbers it is possible to investigate the transition from free flowing powders to very cohesive powders. In Figure 7 the solid volume fraction inside the powder bed after settling (poured density) is shown as a function of the Bond number. For high Bond numbers the solid volume fraction is 0.62 what is close to the solid volume fraction 0.64 of random closed packed monodisperse spheres. For the lowest considered Bond number, the solid volume fraction is 0.32. In the study of the Bond number the nominal particle diameter is kept constant 200 µm and only the cohesion force is adjusted to get the desired Bond number.

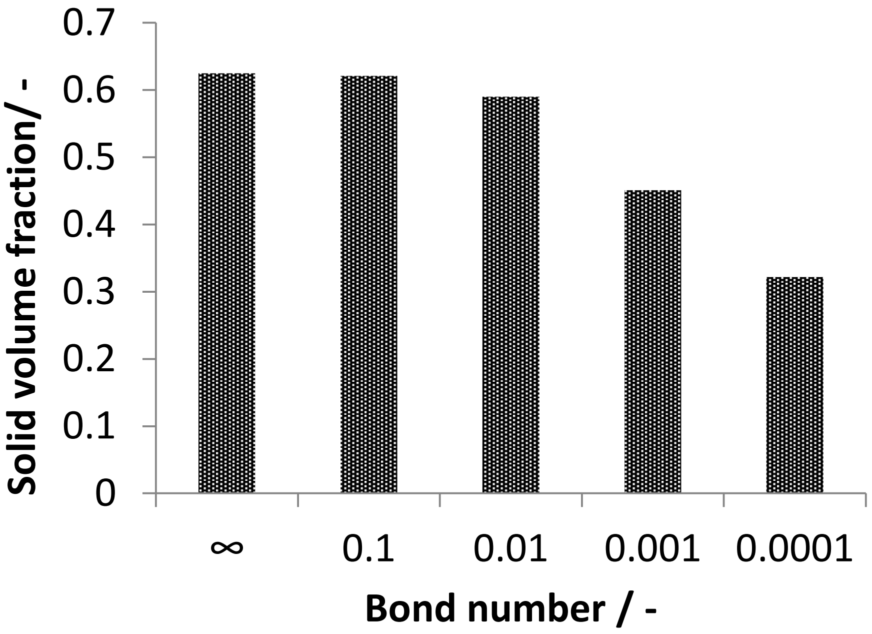

Figure 7: Solid volume fraction inside the powder bed as a function of the Bond number.

2.3 Results and Discussion

2.3.1 Dosing of Non-Cohesive Powder

In Figure 8 three snap-shots of the dosator nozzle cross section during dipping into the powder bed are shown for different cases. The first row represents the reference case of cohesionless particles and a 200 µm nominal diameter. The complete evolution of powder mass inside the nozzle and the average pressure inside the nozzle of the reference simulation (particle stiffness 25 MPa) is shown in Figure 9. In addition, two cases with higher particle stiffness are included. By plotting the dosed mass as a function of the distance from the bottom, the dosator filling process can be divided into three stages. In the figure the feeding process always starts at the right side at the maximum distance and ends at zero distance. During the first stage, the dosator chamber is filled linearly as a function of the traveling path. Filling begins as the nozzle enters the top of powder bed and ends when the piston inside the nozzle reaches the level of powder bed. Since the dosator chamber is filled in this position but there is more or less no pressure acting on the powder, the first stage may be considered as volumetric filling, i.e., mass is directly proportional to the filled volume. During the (intermediate) stage 2, the nozzle moves further through the powder bed. The amount of powder inside the nozzle is nearly constant, yet the pressure increases sharply. Finally, when the nozzle is closer than 1mm to the bottom, another sharp increase in mass occurs. The pressure inside the nozzle is up to 100 times larger than that during the second stage. Hence, the third stage is referred to as the compression step. Thus, only the very last stage of the dosing process determines the pressure inside the dosator nozzle (and hence, the level of compression). As a consequence, the minimum gap occurring at the deepest penetration of the nozzle has very strong impact on the plug stability and dispersability, and thus, is one of the most sensitive (and easily controllable) process parameters.

Interestingly, the particle stiffness used in the simulations does not have a significant impact on the evolution of the dosed mass and the pressure inside the nozzle during the first two stages. Only in the compression stage the softer particles can be easier compressed (higher overlap) compared to the stiff particles, and therefore, the amount of dosed mass is higher for soft particles when the nozzle touches the powder bed floor. The maximum pressure inside the nozzle is lower for softer particles. Thus, for a precise quantitative simulation of the compression stage III of the dosator process a particle stiffness higher than 25 MPa is needed. Alternatively, a factor can be introduced to compensate for the systematic deviation due to soft particles. Since the aim of this work is to get a mechanistic understanding of the dosator process and the qualitative behavior is well represented with softer particles a Young’s modules of 25 MPa is used for the subsequent studies.

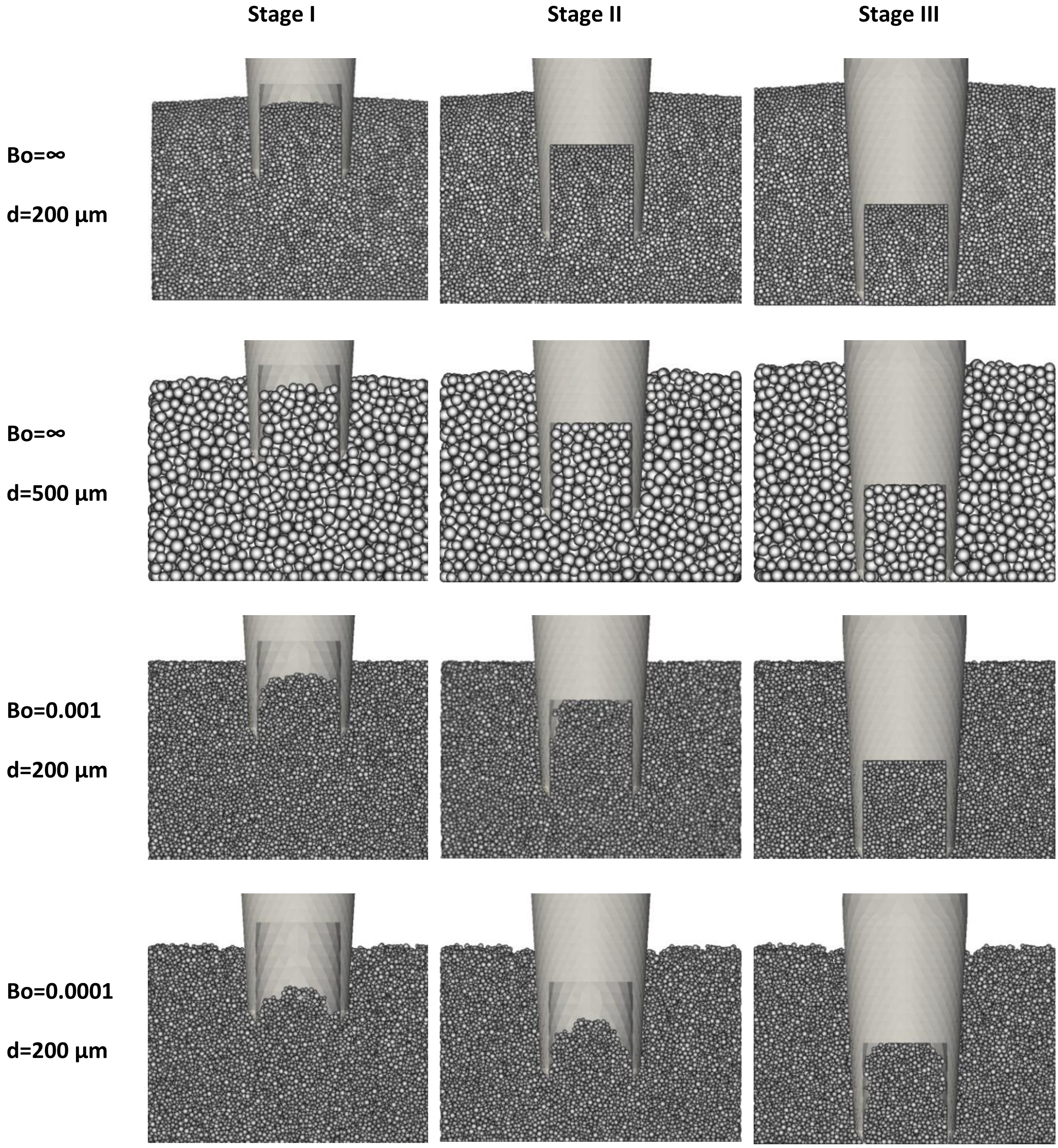

Figure 8: The three stages of dosator filling for different nominal particle diameters and Bond numbers.

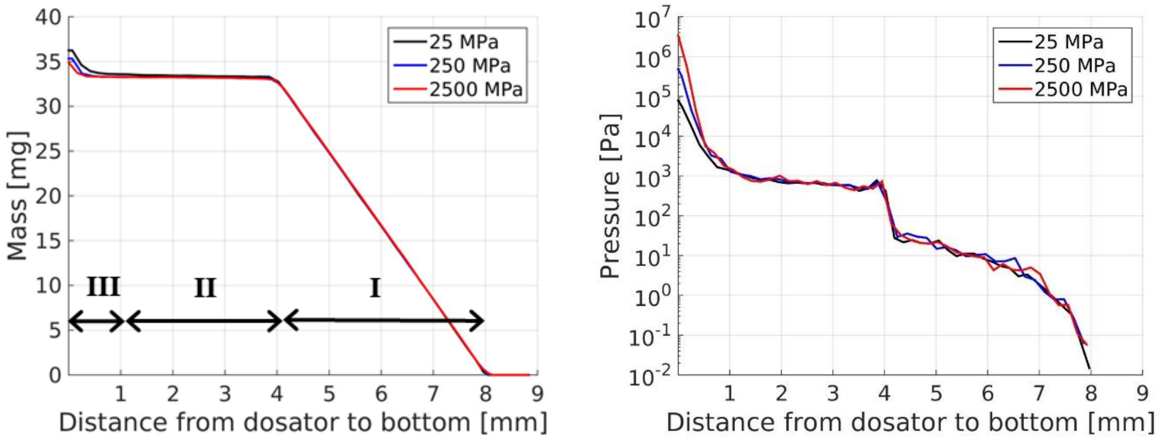

Figure 9: Mass and average pressure inside the dosator as a function of the nozzle position for different particle stiffness. The dosator filling can be divided in three different stages.

Figure 10 shows the powder mass and the average pressure inside the nozzle as a function of the distance to the bottom of the powder bed for five different nominal particle diameters. For all curves, the contact parameters from the reference case are used except for the particle diameter, which is provided in the inset. Three snap-shots of 500 µm particles are shown in Figure 8 and they look similar to the reference case with 200 µm particles.

As can be seen in Figure 10 the qualitative evolution of the powder inside the nozzle is very similar for all particle diameters, though there are significant quantitative differences. Although the initial solid volume fraction for all particle diameters is approximately 0.62 inside the powder bed, after the volumetric filling stage the mass of powder inside the nozzle is lower for bigger particles. This behavior can be referenced to a wall effect, since particle packing close to walls is different compared to far away from walls. The wall effect is more important if the ratio of particle size to the size of the geometry is big. Similarly, a study by [29] showed the increase of the porosity with increasing particle diameter for particles packed into cylindrical container.

In stage two the mass inside the dosator remains constant irrespective of the nominal particle diameter, although there is a small increase in case of 500 µm particles. In average, the pressure inside the nozzle is nearly the same for all particle diameters in the first and second stage of filling. The fluctuation of the pressure is higher for increasing particle diameter, since the number of particles inside the nozzle is smaller for bigger particles. In the compression stage III the pressure is significant higher for bigger particles and so is the amount of additional powder squeezed into the nozzle. This is the reason why the total amount of powder inside the nozzle at end of the process is nearly the same for all particle diameters although it was lower for bigger particles after the volumetric filling phase. However, if only a small gap of 0.5-1mm existed at the end of filling, powder with larger particles would lead to a reduced fill weight (up to 5-10%).

Interestingly, the fill masses in Figure 10 converge for small particle diameters, i.e., below a certain particle-to-dosator-size ratio, size effects are not noticeable. In fact, the ratio of particle and dosator nozzle size matters, as also shown by [29] and [30]. The filling behavior for particle diameter of 200 µm (used in the reference case) is close to the behavior for 75 µm particles. Thus, 200 µm seems a good choice for the reference case.

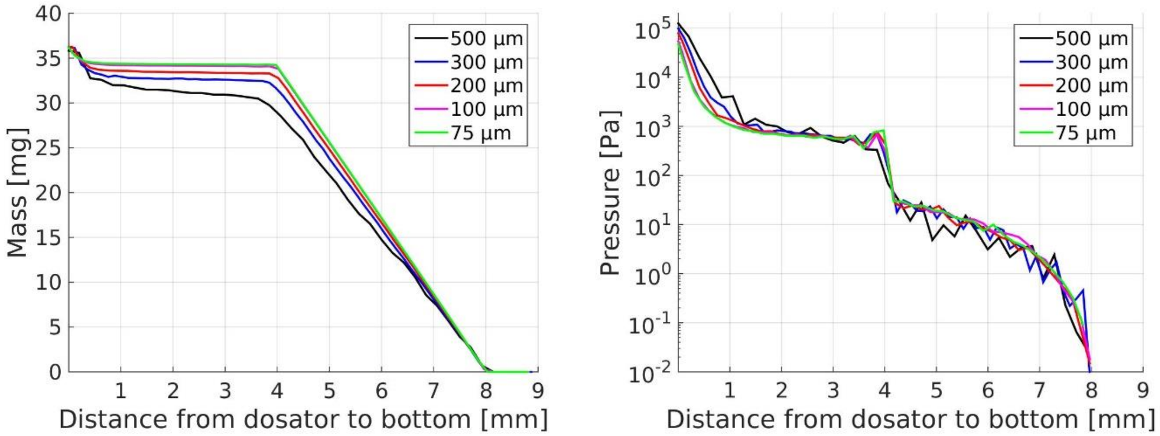

Figure 10: Powder mass and average pressure inside the dosator as a function of the distance to the bottom of powder bed for various nominal particle diameters

In order to gain a better mechanistic understanding of the compression stage a study with different coefficients of friction was performed (Figure 11). The coefficient of friction applies to particle-particle and particle-wall contacts. In addition to the reference case, a high-friction case (coefficient of friction 0.5) and the case of frictionless contacts are shown. The amount of dosed mass after volumetric filling (at a distance of 4 mm) is increased for lower friction coefficients since in this case the particles rearrange easier, leading to denser beds. This can also be seen in the initial powder bed with a solid volume fraction of 0.59 for the high friction case and 0.64 for the frictionless case. Interestingly, the extent of compression in phase III close to the bottom is different for all three cases. In the case of frictionless contacts, there is only compression very close to the bottom, since a quite dense powder bed was already created during phase I of the filling process and particles can "escape" from the region between the lowering dosator nozzle and the bottom of the container. This is shown in Figure 12 (left), which shows the velocity field of the particles during the filling process. Clearly, particles can leave the space below the nozzle for the case of frictionless particles. Compression of the frictionless particles occurs only if the clearance between the nozzle and the bottom is smaller than the particle diameter, i.e., when particles are trapped inside the nozzle (Figure 12 right). In contrast, if particles are frictional, compression starts already at a clearance of 1mm, which is even more pronounced for the case of high-friction contacts. This is due to resistance against the shear flow, which occurs when the powder is squeezed through a small gap close to the bottom for frictional particles (see Figure 12 left).

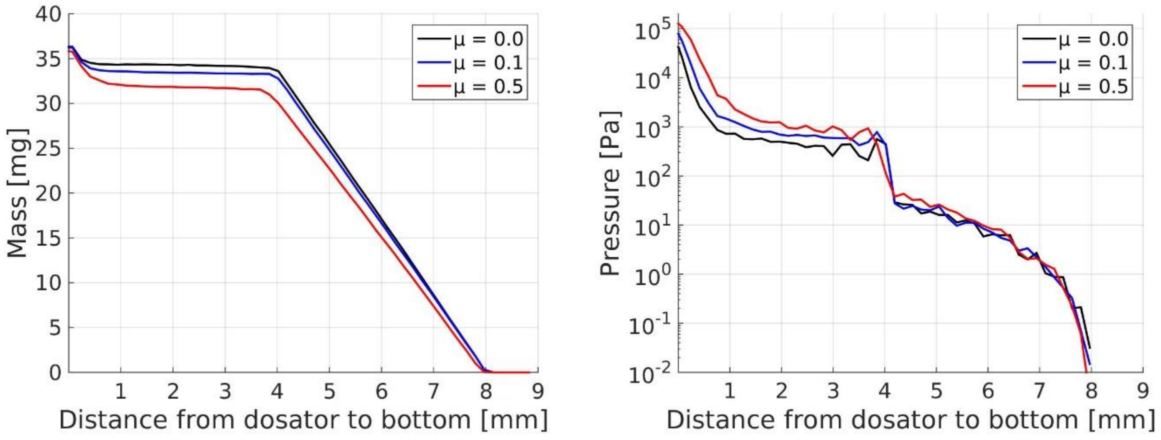

Figure 11: Dosed powder mass and average pressure as a function of distance for various friction coefficients. Frictionless particles lead to denser beds during volumetric filling and high-friction particles are compressed more during the compression stage.

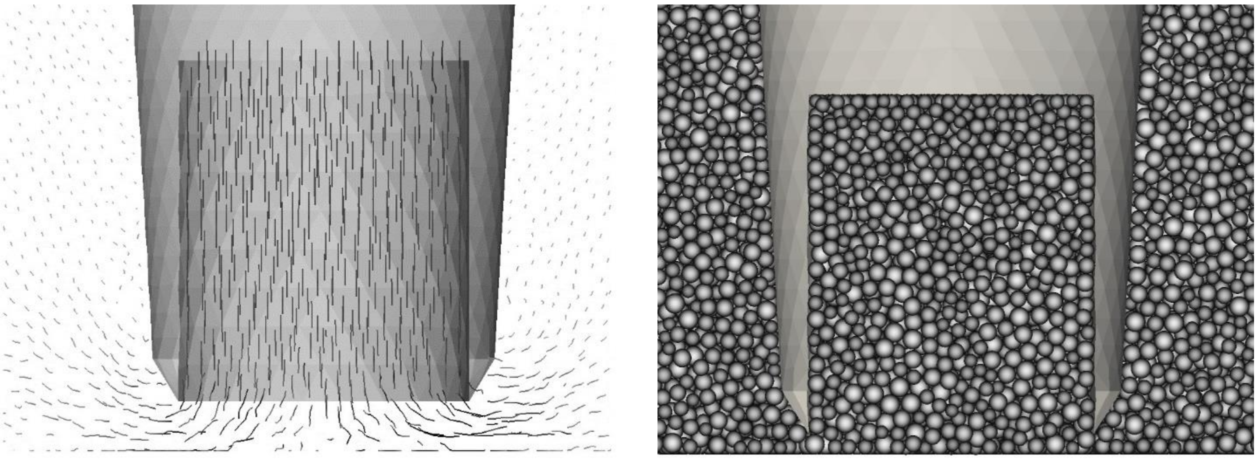

Figure 12: Streamlines of particles during the filling process for the reference case (left). The velocity is proportional to the length of the streamlines. If the gap becomes smaller than the particle size, the particles are trapped inside the dosator chamber (right)

Different stages of dosator filling were observed experimentally also by [5] via force measurement. In these experiments the same nozzle diameter as in the current study was used. In the experiments a sharp increase of the force acting on the nozzle was measured when the nozzle came within 1 to 2 mm to the powder bed floor. This indicates a high pressure acting on the powder inside the nozzle.

The comparison of the plots for various particle diameters in Figure 10 above showed that small particles pack more densely than larger ones during volumetric filling due to lose packing of particles close to the walls and corners. Although this well-known wall effect applies to all particle sizes, the effect on the average solid volume fraction of the nozzle is more important for bigger particles (also see [29]). An opposing effect can be observed during the final compression stage close to the bottom: bigger particles are more compressed, which is due to the particles trapped close to the bottom (Figure 12 right). Particles are not trapped as long as the clearance between nozzle and bottom is larger than the particle size, but the resistance against squeezing them through the gap causes a compression of the powder inside the nozzle. This is also the reason why there is more compression in the case of high friction.

2.3.2 Dosing of Cohesive Powder

The filling behavior of cohesive particles with various Bond numbers is shown in Figure 13. The contact properties are the same as in the reference case (i.e., the case with $Bo=\infty$). With increasing cohesion (decreasing Bond number) the rate of mass accumulation inside the dosator changes dramatically. For Bond numbers 0.1 and 0.01 the plots look similar to the ones for cohesionless particles, i.e., three distinct phases can be observed. However, for Bond numbers 0.001 and 0.0001 the three different stages of dosator filling completely vanish. Instead, the mass inside the dosator increases continuously during the whole movement of the nozzle through the powder bed. The amount of powder during volumetric filling decreases, due to the looser packing of cohesive powder beds. Clearly, the looser packing of the cohesive powder beds (see Figure 7) increases the compressibility of cohesive powders, leading to a different behavior during nozzle filling. In addition, another effect which can be seen in the third and fourth row of Figure 8 comes into play. In case of Bond number 0.0001 the dosator chamber is not completely filled even if the upper end of the chamber is lower than the level of the powder bed. The powder is not able to enter the dosator nozzle, but an arch is formed which prevents dosator filling. This effect is comparable with arches inside of hoppers which prevent hopper outflow. Only as the nozzle gets closer to the powder bed floor and the powder is pressed into the nozzle the dosator can be filled. As a consequence, the total mass inside the nozzle at the bottom of the powder bed is much lower for the case of very strong cohesion (Bond number 0.0001) and the pressure is also significantly lower.

The effect of arching is not that pronounced for a Bond number of 0.001. In this case the dosator is filled volumetrically with some cavities and a lower solid volume fraction compared to the cohesionless case (see Figure 8 stage II). After volumetric filling the powder is compressed continuously until the nozzle touches the powder bed floor. In this way the mass inside the nozzle at the bottom of the powder bed and the pressure inside the powder are identical for the Bond number 0.001 and for cohesionless powder (see Figure 13). The important consequences of the differences in evolution of dosed mass for cohesive and non-cohesive powders are following:

- For non-cohesive powders, the total powder bed height is of minor importance. If the powder bed height increases, the second stage expands and the dosed mass remains nearly constant.
- For cohesive powders, there is no real stage 2 and the dosed mass increases with an increase in the powder bed height. This is a mechanistic explanation why the influence of the powder bed height is more important for cohesive powders, as experimentally observed, e.g., in [10].

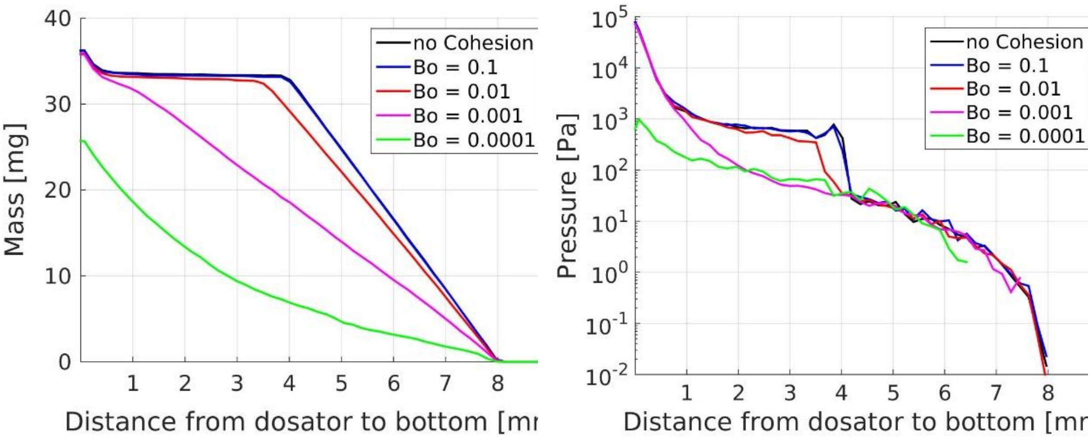

Figure 13: Dosed mass and average pressure as a function of distance from bottom for 200μm particles of various Bond numbers

2.4 Conclusions

The current work focused on a basic understanding of the capsule filling process via dosator system, using the computational method of DEM simulations. The method can simulate the dosing process and can track the amount of powder inside the nozzle as a function of the nozzle's penetration depth (or the distance to the bottom of the bowl) during dosing. The filling behavior of coarse and fine powders and cohesive and non-cohesive powders was compared.

While the influence of the particle size can be explained by the wall effects, the effect of cohesion is more complex. Non-cohesive and cohesive powders have different filling mechanisms of the dosed mass, which mechanistically explains the influence of powder bed height on the fill weight of cohesive and non-cohesive powders observed in the experimental studies.

For non-cohesive powders the amount of dosed powder is not sensitive to the total powder bed height and it is not that important to keep the powder bed height constant in the industrial process. Compared to the simulation it is not possible in the real process to move the nozzle until it touches the powder bed floor, but a certain clearance is needed to avoid damage of the machine. Since the minimum distance to the powder bed floor is very important for the maximum pressure acting on the powder inside the nozzle it is essential to keep the clearance constant. Only for a constant pressure a constant density and strength of the dosed plug can be expected.

For cohesive powders the amount of dosed powder is sensitive to the total powder bed height and the smallest clearance between nozzle and powder bed floor. Cohesive powders form a powder bed of lower solid volume fraction and are therefore easier to compress. If the nozzle moves through the powder bed the powder gets densified continuously. For very cohesive powders arching is observed and it is difficult to fill the nozzle. To avoid the problem of arching a dosator chamber with bigger diameter and smaller height may be beneficial similar as a wider hopper opening is beneficial to avoid arching during hopper outflow.

To keep the computational time reasonable, using bigger and softer particles in the simulation compared to real powders is necessary. With regard to the investigated dosator geometry (diameter 3.4 mm, length 4 mm), nominal particle diameters in the range of 75-300 µm produced qualitatively comparable results. For larger particles significant deviations were observed. This indicates that the particle diameter should be less than approximately one tenth of the smallest dimension of the geometry. For quantitative studies, correction factors should be used to compensate for the artificial wall effect due to enlarged particle diameters. Particle softening is critical if there are high contact forces or if the cohesion forces are computed based on the contact area.

To avoid confusion with respect to cohesion forces a cohesion model with a constant cohesion force was used to adjust desired Bond numbers. In this work, only selected Bond numbers were used to model the powder properties, ranging from free-flowing to highly cohesive. Simulating a real powder in future work will require calibrating the contact properties accordingly. Only in this way a direct comparison between simulations and experiments can be made. To achieve a better understanding of the process, the geometry of the dosator and the powder bed height should be varied for various powder properties.

For future studies, not only the movement of the dosator into the powder bed, but also the movement out of the bed should be considered to establish if the powder plug inside the nozzle is stable or if there is a loss of powder. Finally, the variability of the dosed mass as a function of bed inhomogeneity will be studied, since this is another critical quality indicator of filled pharmaceutical capsules. The ultimate goal should be to determine material and process parameters (i.e., a comprehensive design space) that ensure a stable process with low variations in the dosed mass.

3 Modeling Yield Properties of Compacted Powder using a Multi-Particle Finite Element Model with Cohesive Contacts[b]

Abstract: The multi-particle finite element method (MPFEM) was used to simulate the yield properties of compacted powders with cohesive contacts. A suitable representative volume element (RVE) of monodisperse, spherical, deformable particles was created to be implemented into a commercially available finite element code. New efficient periodic boundary conditions were proposed to compute representative properties of the volume at limited computational costs. A contact model was introduced, which includes repulsive forces, friction forces and cohesion forces. As a result, the proposed model is capable of considering tensile strength in a MPFEM setting, which was not attainable in related published work.

We present extensive parameter studies to demonstrate the performance of the proposed RVE and to find the optimal balance between accuracy and computational speed. The minimum mesh fineness and the minimum number of particles in the RVE were determined during convergence studies. The employed explicit integration scheme was enhanced by means of mass scaling. The optimized model was used to predict the strength of compacted powders. A simple analytical expression was fitted to the numerical predictions to describe the uniaxial tensile strength and the uniaxial compression strength as a function of the powders' relative density and the cohesion strength of the contacts. A general form of a yield surface was proposed to describe the yield properties for generic load cases, which can be applied to different relative densities and cohesion strengths. As a result, we showed that the yield surfaces grow with increasing relative density, while they change their shape with increasing cohesion strength. The obtained yield surface results in the Drucker-Prager/Cap model in case of low cohesion,

---

[b] This section is based on the journal article "Modeling yield properties of compacted powder using a multi-particle finite element model with cohesive contacts" by Loidolt et al. in Powder Technology 2018

whereas it has an elliptical shape in case of high cohesion. The proposed analytical form of the yield surface is capable of describing both cases.

3.1 Introduction

Cold compaction of powder is important for many industrial processes, e.g., for the production of green bodies before sintering of metals, ceramic parts in mechanical engineering, pellets for mineral or animal food industry or the production of tablets in the pharmaceutical industry [31–34]. The goal of powder compaction is to reduce the volume of the powder, increase the flowability or to create a part of a certain shape and size.

The final powder compact requires a minimum strength as otherwise it would disintegrate during processing, transportation or storage. The strength of a compact depends on both, material and process parameters. Important material parameters are the chemical composition of the primary particles (and their mechanical properties), as well as the particles' size and shape. Furthermore, the material properties are influenced by the environmental conditions, e.g., temperature and humidity. The process parameters include the geometry of toolings and dies, the compaction stress or strain, as well as on the compaction force-versus-time profile, which depends on the control strategy of the compaction machine. Experiments can be used to adjust the process to get the desired compact properties. Commonly, this is time-consuming, as process parameters change often, e.g., the geometry of the machine tools or the powder properties. Hence, reliable numerical models to predict the properties of compacts with simulations are crucial.

Phenomenological models for powder compression have been in use for many decades. The Heckel equation [35] and the Kawakita [36] equation are, among many other approaches, most commonly used nowadays. Recent studies dealing with these equations were reported [37–39]. Both equations correlate the applied pressure with the relative density (or porosity) of the powder compact. Another noteworthy phenomenological model is the Ryshkewitch-Duckworth

[40] equation which correlates the relative density of a powder compact with its strength, which is of higher interest in practical situations. Recent studies using this equation are reported in [41,42]. All models have in common that the introduced constants are empirically adjusted by means of compaction experiments and force measurements. The disadvantages of these phenomenological approaches are the minimal mechanistic understanding of the process and the lack of information about the strength of the final compact. Moreover, the parameters determined for one material (or one size fraction) are not valid for other materials.

There also exist some analytical models in the literature which describe the compaction process. We mention here exemplarily [43] and [44] with analytically derived flow surfaces and [45] with the authors considering the densification during compaction and sintering theoretically. Although very interesting in principle, the disadvantage of analytical models is their oversimplification. Most often, affine motion has to be assumed and the description of particle deformation is very difficult. Such assumptions limit the practical applicability of these models.

In recent years, two numerical methods became important for powder flow simulations, which are the discrete element method (DEM) and the finite element method (FEM). In DEM every single particle is modelled and numerically tracked. The interaction forces between particles are computed based on the overlap of the particles (soft-sphere model) and Newton’s equations of motion are solved for the particles’ acceleration, velocity and position. As a result, the rearrangement of particles during compaction can be efficiently modelled. Recent investigations in this area were carried out, e.g., by [46–50]. Note that particle deformation, which is dominant at higher densities of the powder compact, are commonly not taken into account. Furthermore, the fully discretized nature of DEM entails high computational costs and practically limits the number of particles to fewer than 10 million. In contrast, in classical FEM simulations powders are described as a continuum, i.e., the discrete nature of the particles is not implemented. This renders the method to be much more efficient than DEM. Recent studies include [51–53]. However, in FEM a material model is required to connect the stress and the strain of the material. The determination of such material models, including the yield surface, is a difficult and cumbersome task.

Several models for yield surfaces connected to powder compaction can be found in the literature. The Drucker-Prager/Cap model based on [2] is one of the most often used yield surfaces. It is conceived for pressure-dependent materials and widely used for geological materials, powders, polymers, concrete, foams and other substances. Another common model is the so-called modified Cam-Clay model [54], which was developed for soft soils. Its yield surface is an elliptical curve. Both models are compared in the recent work of [55]. The shape and the evolution of the yield surfaces are shown in the p-q diagrams (equivalent pressure stress p and von Mises equivalent stress q) (see Figure 14). With regard to powder compaction, both models are employed for the description of powders with small or negligible tensile strength, since in such a case the yield surfaces do not extend into the negative pressure region. In contrast, the metallic foam model proposed by [56,57] and the Gurson model [58] can be used if tensile strength has to be taken into account (see Figure 14). The metallic foam model, which has the shape of an ellipse, is used to model foams which have a comparably high void fraction. In case of volumetric hardening (as it is shown in Figure 14) the tensile strength is fixed and the compression strength increases during compaction. For the metallic foam model with isotropic hardening, the center of the ellipse is located at the origin of a p-q diagram. The Gurson model is developed for porous materials with comparably small voidage rather than for compacted powders. Its yield surface is symmetric with respect to the q-axis and grows with decreasing voidage f. As a side note, all mentioned yield surface models are implemented in Abaqus 6.14 as standard material models.

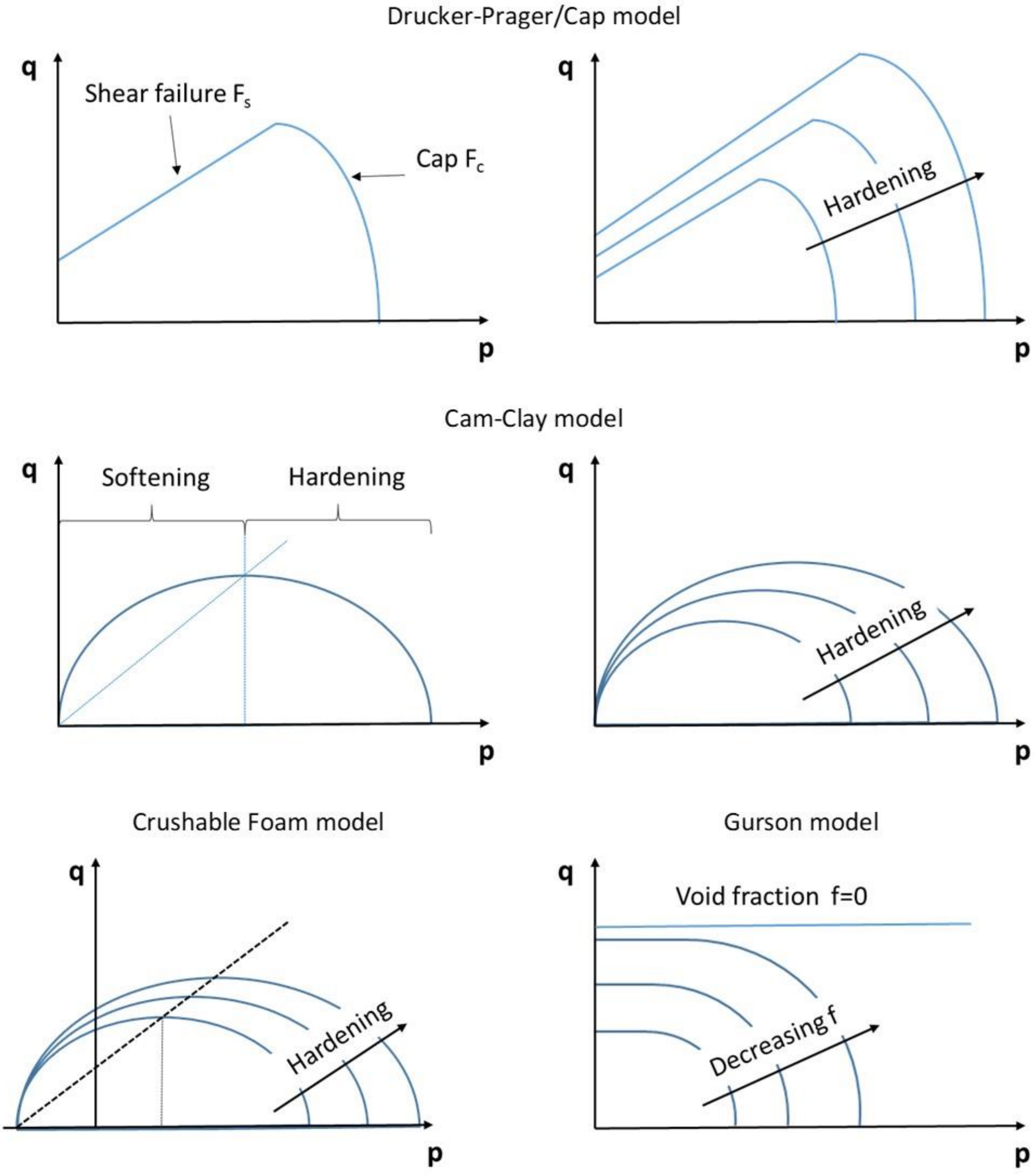

Figure 14: Schematic of the Drucker-Prager/Cap model and the modified Cam-Clay model in the p-q plane. In addition to the shape of the yield surface the evolution of the yield surface with relative density (hardening) is shown. For powders with substantial tensile strength the yield surface for crushable foam and the Gurson yield surface for porous metal can be used.

A kind of combination of DEM and FEM is the multi-particle finite element method (MPFEM), also called the discrete finite element method. This approach considers discrete particles by treating each single particle with FEM. The meshed particles may deform according to some elasto-plastic material law and interact with each other via contact mechanics. The MPFEM has the advantage of taking all granular phenomena into account: irregularly shaped particles, packing density, interfacial friction and cohesion, particle deformation and other properties. Recent approaches in the literature include [59–62]. The disadvantage of this method is the very high computational costs, which by far exceed the computational cost of DEM with the same number of particles. Hence, it is usually not possible to model complete powder compacts, but only small sections of the powder.

In order to account for these computational limitations, in our work only a small representative volume with a certain number of particles is considered. This "micromechanical" model is then used to determine macroscopic properties of the powder, which could be used in a continuum FEM model of a complete powder compact.

The state of the art in micromechanical modeling defines a *representative volume element* (RVE) in a computational homogenization procedure [63]. The objective is to compute the macroscopic properties of a heterogeneous material from the response of its underlying microstructure. The heterogeneous material may then be substituted with an equivalent homogeneous one. An RVE considers a small but representative volume of the structure, which features all relevant characteristics of the material's microstructure. The RVE needs to be sufficiently large in size to capture enough microstructural information, but small enough to show no gradients of a macroscopic state variable. The effective macroscopic properties are commonly computed by averaging over the internal fields in the RVE in a first-order strain-driven computational homogenization. The boundary conditions of the RVE are generally defined such that the energy equivalence between the two scales, the so called Hill–Mandel condition (macro-homogeneity), is preserved [64–66].

$$\overline{\boldsymbol{P}}:\dot{\overline{\boldsymbol{F}}} = \frac{1}{\Omega_0}\int_{B_0} \boldsymbol{P}:\dot{\boldsymbol{F}}\,\mathrm{d}V_0. \qquad (7)$$

The quantity $\boldsymbol{P}$ represents the first Piola-Kirchhoff stress tensor, $\boldsymbol{F}$ the deformation gradient and Ω_0 is the referential volume. Note that in case of a powder or porous material, Ω_0 takes also the voids between the particles into account. Quantities with a bar denote the macroscopic equivalents. Several boundary conditions obey this requirement: constant deformation over the entire RVE (Voigt-Taylor's bound), constant stress over the entire RVE (Reuß-Sachs's bound), linear displacement on the boundary of the RVE, constant traction on the boundary of the RVE domain, and periodic displacement and antiperiodic traction boundary conditions (PBC).

This work investigates the influence of cohesive contact between compacted particles on the yield properties of the resulting powder compact. An appropriate RVE with periodic boundary conditions (PBCs) in an MPFEM is determined. However, new PBCs needed to be developed in this work for two reasons. First, the boundary conditions need to be suitable not only to apply pressure, but also tension load to test the strength of the cohesive contacts. Second, a computationally efficient implementation for technological-relevant processes should be possible, allowing implementation into commercially available FEM software packages.

The paper is organized as follows. Section 3.2 gives details about the MPFEM. A new formulation of PBCs, the interfacial contact and the simulation procedure are described. Section 3.3 presents convergence studies in probing the yield surface using the proposed RVE setting. Section 3.4 applies the model to a powder compact with different degrees of cohesive contact. We demonstrate the large influence of cohesion and how the yield surface significantly changes its shape. Finally, a conclusion closes the paper in section 3.5.

3.2 MPFEM Model with Cohesive Contact of Particles

3.2.1 Boundary Conditions of the RVE

Homogenization procedures, which are based on Eq. (7), are well developed for continuous microstructures. Particle microstructures as encountered in powder compaction are more difficult to handle. The basic difficulty in the transition is the possible rotation of particles, which leads to an inconsistency with a homogenized standard macro-continuum. Here we apply the approach discussed in [67–69], which facilitates the quasi-static homogenization of (rigid) granular aggregates. The same approach can be used for our model of deformable particles since a reference point is assigned to each particle. The discrete counterpart to Eq. (7) is discussed in [68] and shown in Eq. (8). The discrete Hill-Mandel-type condition is postulated as

$$1/V \cdot \sum_{q=1}^{M} \left(\boldsymbol{a}_q - \bar{\boldsymbol{P}}\boldsymbol{A}_q\right) \cdot (\dot{\boldsymbol{x}}_q - \dot{\bar{\boldsymbol{F}}}\boldsymbol{X}_q) = 0. \tag{8}$$

We thereby assume a microstructure volume V that characterizes an RVE of a granular aggregate of solid particles. The centroid of a boundary particle q for q=1,…,M of this aggregate is located at $\boldsymbol{X}_q \in \partial V$ in the reference configuration and $\boldsymbol{x}_q$ in the current configuration. The continuous-to-discrete transition is conceptually performed by the operations $\int_{\partial V_q} \boldsymbol{N}\, dA \rightarrow \boldsymbol{A}_q$ and $\int_{\partial V_q} \boldsymbol{t}\, dA \rightarrow \boldsymbol{a}_q$. Hence, infinitesimal boundary area vectors (with $\boldsymbol{N}$ being the normal vector pointing outward of the boundary) are transformed to the finite area vectors $\boldsymbol{A}_q$ and infinitesimal boundary forces (with boundary traction $\boldsymbol{t}$) are transformed to finite forces $\boldsymbol{a}_q$ acting at the center point of each boundary particle. The quantity ∂V_q is the portion of the microstructural boundary domain ∂V associated with particle q. Several boundary conditions obey the discrete Hill-Mandel requirement.

For example, linear displacements on the entire boundary ∂V of an RVE are invoked by

$$\boldsymbol{x}_q = \bar{\boldsymbol{F}}\boldsymbol{X}_q \qquad \text{for } q = 1, \dots, M. \tag{9}$$

The particles' centers are translated according to the prescribed macroscopic deformation gradient (Dirichlet BC). Additionally, the boundary particle rotations are constrained to be zero. This boundary condition causes a too stiff macroscopic response, since particles are not able to rearrange as they could inside the powder bed.

Next, a constant traction boundary condition prescribed on the entire boundary ∂V of an RVE may be applied, i.e.,

$$\boldsymbol{a}_q = \overline{\boldsymbol{P}}\boldsymbol{A}_q \qquad \text{for } q = 1, \dots, M. \tag{10}$$

The discrete support forces $\boldsymbol{a}_q$ are determined according to the macroscopic first Piola-Kirchhoff stress (Neumann BC). The particles are free to rotate in this setting. Problems of non-uniqueness and rigid body motions may arise in this setting, which are overcome in continuous homogenization by additional semi-Dirichlet BC in the literature [63,70]. This boundary condition results in a too soft macroscopic response since particles can rearrange easier than inside a powder bed.

The third option is to use periodic boundary conditions that relax the Dirichlet constraint to some extent. The boundary is split into periodic (opposing) counterparts. Each particle $\boldsymbol{X}_q^+$ in ∂V^+ has an associated particle $\boldsymbol{X}_q^-$ in ∂V^- (with $\partial V = \partial V^+ \cup \partial V^-$). Therefore, periodicity of the deformation of a granular medium can be enforced by a periodic displacement of the particle center and anti-periodicity of the particle support forces:

$$\boldsymbol{x}_q^+ - \boldsymbol{x}_q^- = \overline{\boldsymbol{F}}[\boldsymbol{X}_q^+ - \boldsymbol{X}_q^-], \qquad \boldsymbol{a}_q^+ + \boldsymbol{a}_q^- = \boldsymbol{0} \quad \text{for } q = 1, \dots, M/2. \tag{11}$$

In addition, the boundary particle rotations $\boldsymbol{q}_q$ need to be periodic as well: $\boldsymbol{q}_q^+ - \boldsymbol{q}_q^- = \boldsymbol{0}$. A proper application of periodic boundary conditions requires a periodic topology of the particles in this setting. Even more, application of periodic boundary conditions requires a periodic mesh in the FEM discretization where every node on the boundary was constraint to its opposite counterpart.

In our implementation, we avoid constraining every node on the boundary. Accordingly, we employ a new flavor of periodic boundary conditions suitable for MPFEM, which is designed to be compatible with conventional finite element code architectures. For demonstration purposes we consider a simple face-centered unit cell as shown in Figure 15 and use the commercial multi-purpose finite element package Abaqus 6.14. If a particle at the boundary of the periodic box is found, an associated particle is placed at the opposite side of the periodic box to obtain a periodic arrangement. A reference point is assigned to the center of each boundary particle. The reference points are used to enforce the periodic boundary condition according to Eq. (11) and the displacements and the forces on the reference points are used for the homogenization based on Eq. (8). Then we define a simulation box, which is the size of the periodic box enlarged by an add-on layer. Every finite element located outside the simulation box is removed. The nodes and elements in the add-on layer of every single boundary particle are used to distribute the reaction force of its reference point via distributing coupling. The distributing coupling enforces a distribution of loads, which means that the sum of the forces and the moments at the coupling nodes is equivalent to the forces and moments at the reference node. The coupling forces are weighted based on the surface area of the coupled elements (for detailed information see also [71]). The thickness of the add-on layer is half of the largest particle radius to have enough nodes for the distributing coupling and to avoid stress concentrations. A thicker add-on layer would cause additional computational costs and thus has no further benefit.

Finally, the pairs of reference points for opposite particles in the RVE are constrained to enforce the periodic boundary conditions. The constraints are applied via linear constraint equation for all degrees of freedom (3 translational and 3 rotational). To deform the RVE during simulation ($\boldsymbol{x}_q^+ - \boldsymbol{x}_q^- \neq \boldsymbol{0}$) it is necessary to introduce three auxiliary nodes to the model. Each auxiliary node is assigned to a pair of opposing faces of the RVE and controls the movement of the faces to each other. The linear constraint equation for two opposite boundary particles on faces with a normal vector in x-direction, as shown in Figure 15, can be written as:

$$\boldsymbol{x}_q^+ - \boldsymbol{x}_q^- + \boldsymbol{x}_{ref,x} = \boldsymbol{0}, \;\; \boldsymbol{q}_q^+ - \boldsymbol{q}_q^- = \boldsymbol{0} \tag{12}$$

As a result, we obtain 6*N* constraint equations for *N* pairs of opposite boundary particles. The approach of three auxiliary nodes was also used in the MPFEM model of [72]. The advantage of our approach is the relatively low number of constraint equations that are needed to apply periodic boundary conditions. Consequently, this approach increases the simulation speed dramatically.

The application of the periodic boundary condition during the whole simulation procedure is summarized as follows: During compaction of the RVE the displacement of the auxiliary nodes is prescribed. The auxiliary nodes are kinematically constrained to the reference points of the boundary particles, which are themselves connected to their coupling nodes via distributing coupling. This way a macroscopic deformation gradient can be incrementally applied. Then the system of equations is solved and the nodal positions of the inner particles are updated. This mode is referred to as “deformation-controlled”. During probing of the yield strength, the load of the auxiliary nodes is prescribed to achieve a certain macroscopic stress of the RVE. This mode is referred to as “force-controlled”. We restrict ourselves to three auxiliary nodes in this powder compaction study, which limits the change in the RVE’s shape to a cuboid. The generalization of the proposed procedure to more auxiliary nodes is straightforward.

Note that the proposed RVE is similar to the procedure in [72]. These authors use linear constraint equations to prescribe the displacement of pairs of nodes on the opposite sides of the RVE. The constraint equations are also governed by the displacements of three auxiliary nodes. Each auxiliary node is connected to one of the three parallel faces of the cubic RVE. The parallel faces need to have a periodic mesh topology, which is solved by the authors with ‘ghost particles’. For every particle on the boundary there exists a particle composed of the surface nodes on the opposite boundary. These surface nodes are constrained with each other. However, a high number of constraint equations have to be solved, which reduces significantly the efficiency of the FE solver and slows down the simulation.

Another similar methodology is presented by [59] and [62]. These authors study the compaction of ductile metal powders through a numerical assembly of elastic–plastic and rate-independent spherical particles, which are in frictional contact. The simulation results revealed yield surfaces with both isotropic and kinematic hardening mechanisms. Their work uses rigid planes for the walls of the RVE to bound the particles into a cubic volume, which has certainly a large influence on the homogenized macroscopic quantities.

An implementation of PBCs was also accomplished in [73] via surface-to-surface constraints, i.e., by constraining each node on a slave surface to have the same motion as the closest point on a master surface. The authors in [74] present different approaches for possible boundary conditions resulting in periodic and non-periodic RVE topologies. Among others, these authors advocate approximate periodic boundary conditions via surface-to-surface constraints available in most commercial FE software packages. Kinematic coupling is enforced in a master-slave approach. The degrees of freedom at the coupling nodes are eliminated, which will move henceforth with a reference point (see Figure 15).

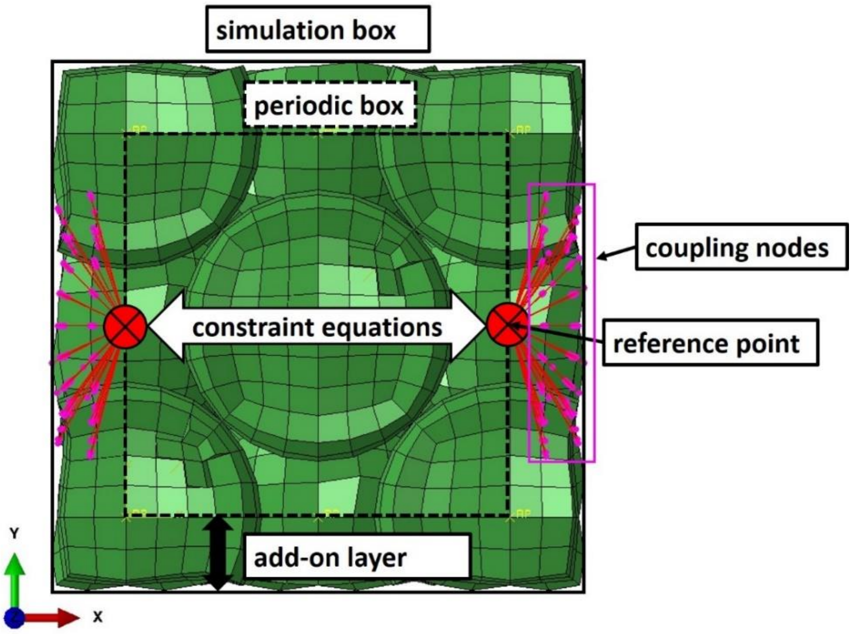

Figure 15: Periodic boundary conditions of two opposite particles in a RVE with particles arranged as a face-centered unit cell.

In addition, note that the proposed periodic boundary conditions can be applied to systems with non-periodically meshed particles, i.e., the associated (opposite) particles in the add-on layer in

Figure 15 do not need to have the same mesh. It is obvious that the choice of the reference points and the distributed coupling with nodes in the vicinity via distributing coupling is independent of the discretization. In [74], a similar definition of boundary conditions is reported, which does not require periodicity of the underlying discretization. These authors conclude that enforcing periodicity is not necessary in order to identify material parameters for technologically relevant processes. We refrain from showing non-periodic meshes in this article as we focus on the dependence of yield surfaces on cohesion. Furthermore, we only study spherical particles and creating a periodic mesh is simple in this case.

3.2.2 Interfacial Contact of Particles

Failure of powder often occurs at contacts between particles, especially if the cohesion interaction of the contacts is weak. As a result, contact properties are of great importance in powder modeling and a suitable implementation of friction and cohesion forces is necessary. We propose in this work to compute the contact forces with the balanced master-slave method. This method is robust and allows for an efficient implementation into existing (commercial) finite element software packages.

In the balanced master-slave method the contact forces are computed as a linear combination of the pure master-slave forces of the two surfaces in contact. In our case the forces of the interchanged master-slave pairs will be weighted equally. The contact force of each node on the slave surface is computed as a function of contact stress multiplied by the associated surface area. To compute the contact stress, we implement a simple user-defined contact model (including cohesion stress) using the VUINTERACTION user subroutine in Abaqus 6.14. The contact normal stress is computed as a function of the normal distance δ_N of the slave node to the master surface as shown in Figure 16 and Figure 17. The distance has positive values for penetration and negative values for separation (Figure 17). Similar the contact tangential stress is computed as a function of the relative tangential displacement δ_T. Additionally, a numeric damping coefficient d can be included, which damps the system as a function of the normal relative velocity $\dot{\delta}_N$ and the tangential relative velocity $\dot{\delta}_T$.

Three different situations are considered (see Table 2 and Figure 16 (right)). First, if the separation is greater than δ_0, no interaction between the surfaces occurs and all stresses are zero. The quantity δ_0 is the interaction length of the cohesion model. Second, the cohesion stress increases linearly as a function of the distance starting from δ_0 until the slave node touches the discretized master surface. The repulsive normal stress σ_{rep} and the tangential friction stress σ_{fric} remain zero until the discretized surfaces virtually penetrate each other. Third, if the surfaces penetrate each other, the repulsive normal stress increases linearly as a function of the penetration δ_N. The contact stiffness k is chosen such that the penetration remains small compared to the dimension of the particles (penetration/diameter < 0.001), yet avoiding stability issues due to a too stiff contact. The cohesion stress remains constant, if the surfaces are in contact. The friction stress increases linearly with the relative tangential displacement δ_T and is limited by the maximum friction force, which is the product of the repulsive stress and the coefficient of friction.

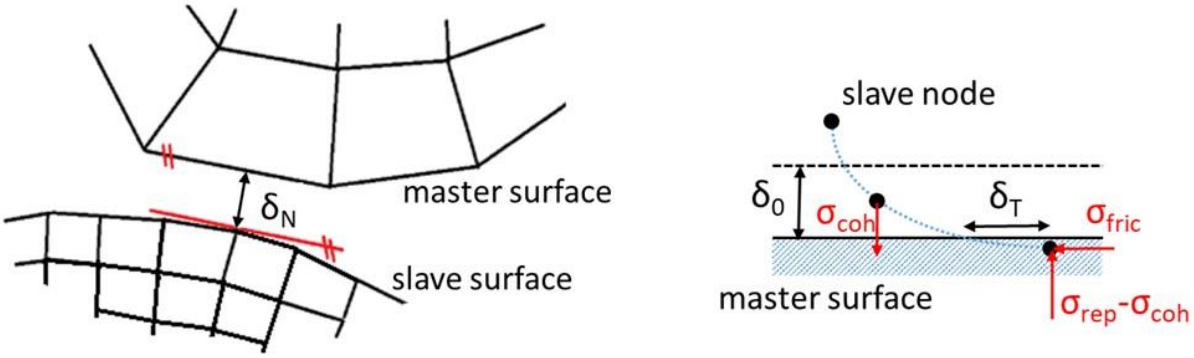

Figure 16: Determination of the normal distance in the master-slave contact algorithm (left). Schematic representation of the load on a slave node approaching a master surface (right).

Table 2: Overview contact model with cohesion stress

	Normal direction	**Tangential direction**
$\boldsymbol{\delta_N < \delta_0}$	$\sigma_N = 0$	$\sigma_T = 0$
$\boldsymbol{\delta_0 < \delta_N < 0}$	$\sigma_{rep} = 0$ $\sigma_{coh} = c_{max}\left(1 - \frac{\delta_N}{\delta_0}\right)$	$\sigma_{fric} = 0$
$\boldsymbol{0 < \delta_N}$	$\sigma_{rep} = k \cdot \delta_N$ $\sigma_{coh} = c_{max}$	$\lvert k \cdot \delta_T \rvert < \sigma_{rep} \cdot \mu$: $\sigma_{fric} = -k \cdot \delta_T$ $\lvert k \cdot \delta_T \rvert > \sigma_{rep} \cdot \mu$: $\sigma_{fric} = -\sigma_{rep} \cdot \mu \cdot \frac{\delta_T}{\lvert \delta_T \rvert}$
total	$\sigma_N = \sigma_{rep} - \sigma_{coh} + d \cdot \dot{\delta}_N$	$\sigma_T = \sigma_{fric} - 0.01 \cdot d \cdot \dot{\delta}_T$

The total normal stress σ_N, which is enforced at the slave node, is a function of the repulsive stress, the cohesion stress and additional damping. The evolution of the contact normal stress as a function of the dimensionless overlap (overlap/particle diameter) without damping is shown in Figure 17. The signs follow the convention that compressive stress is taken to be positive. The damping is a linear function of the relative speed and the damping coefficient d. The value of the damping coefficient is chosen such that contact oscillations are dampened, yet substantial additional macroscopic stresses are avoided. Without damping the elastic contact would lead to an oscillating movement of the particles. Similar to the normal stress, the total tangential stress σ_T is a function of the friction stress and a tangential damping.

The implemented contact model considers contact cohesion in a simplified way. Dependent on the physical origin of the cohesion interaction a different cohesion model may be implemented. We use this simple model to obtain a clear picture of how contact cohesion influences the yield properties of compacted powder.

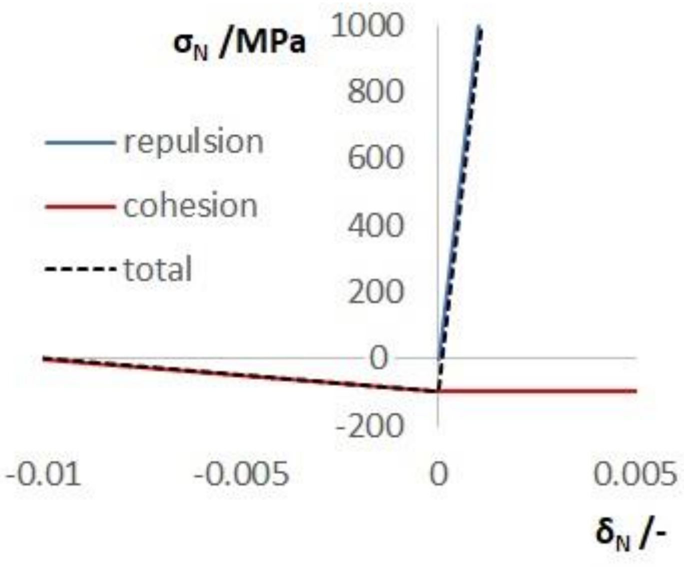

Figure 17: Contact normal stress as function of the relative overlap (overlap/diameter)

3.2.3 *Simulation Procedure*

We chose a cubic RVE filled with monodisperse random close-packed spheres. The initial packing (relative density 0.64) is obtained from a DEM simulation in LIGGGHTS® [25]. During the DEM simulation a cubic box with periodic boundary conditions is filled with randomly placed spheres. Starting from a loose initial packing the diameter of the particles is ramped up until a relative density of 0.64 is reached. The periodic boundary condition of the DEM code automatically creates a periodic counterpart for each particle at the boundary of the box. The DEM simulation offers therefore a suitable initial packing for our model. In the MPFEM model PBC and the interfacial contact as described in section 3.2.1 and 3.2.2 are used. Furthermore, each particle is modeled as an elasto-plastic body, which does not break during deformation. This assumption is in good agreement with the experimental behavior of metallic particles, but may not be as applicable to ceramics or certain brittle compaction aids used in the pharmaceutical industry.

A MPFEM simulation is divided into three steps, i.e., compaction, unloading and reloading, as shown in Figure 18. The compaction and unloading steps correspond to the production of a real powder part. The reloading corresponds to the testing of the powder-part strength and is used in the simulation to determine the yield points in the stress space. In the compaction step, the randomly-filled close-packed particles are compacted by a deformation-controlled isotropic compression to reach a certain relative density of the entire RVE. In order to keep the accelerations small, the deformation speed is linearly ramped up in the first half of the compaction step and linearly ramped down in the second half. After compaction a short dwell step with fixed boundaries of the RVE is included to allow for dissipation of possible oscillations. Then the load control of the RVE is shifted to force control, and the load is linearly ramped down during unloading to relieve the RVE to a state of 0.1 MPa isostatic compression stress. The small residual compression stress is used to avoid disintegration of the compact in case of cohesion-less contacts. After releasing the applied load, we end up with a compacted RVE without unnatural gaps between the particles. This state of the RVE will be taken as the RVE's reference state as it corresponds to the state of a powder part after production.

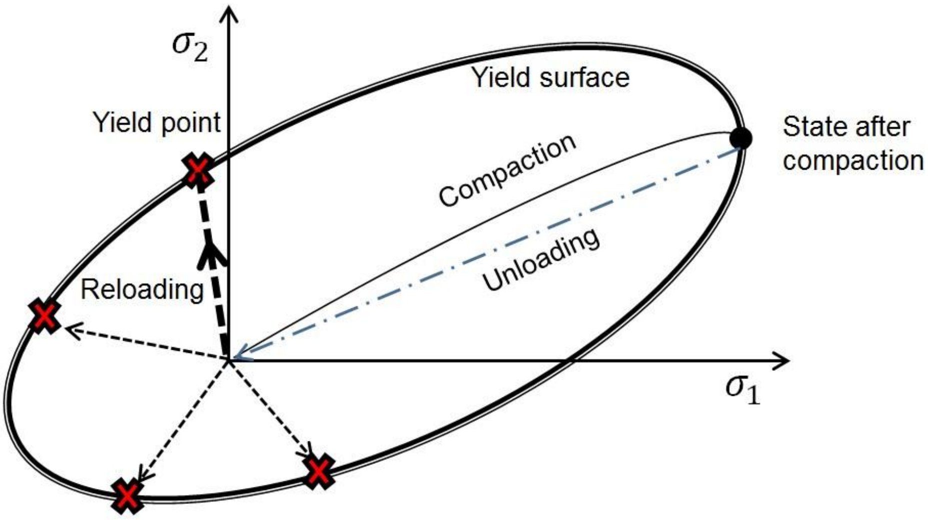

Figure 18: Schematic evolution of the stress during the three steps of the compaction and subsequent yielding simulation. The real simulation is in 3D.

The size of the reference RVE is used to compute the stresses and strains needed for the calculation of the yield points. The edge lengths of the RVE are denoted as X, Y and Z and the area of the faces are A_x, A_y and A_z. In the reloading step the RVE is reloaded in different directions to probe different yield points on the yield surface. The probing of each direction is independent of each other and always starts from the reference RVE. The probing of one direction is an elaborate procedure as it is necessary to ramp up the stress slowly towards the unknown yield point to avoid inertial effects. As a remedy, we probe each direction at least three times to approach the yield point with sufficient accuracy, i.e., we use two trial steps to estimate the yield point and use the third one to hit the yield surface sufficiently slowly to minimize inertial effects.

The three-step procedure (compaction, unloading, reloading) is similar to the work [59] and [72], although the former authors use rigid walls as BC and both do not consider cohesion. Furthermore, in the referenced studies only the compaction step was performed with the explicit solver of Abaqus and the implicit solver was used for unloading and reloading. This has the potential benefit of a reduction in computational costs since bigger time steps can be used with the implicit solver. In the present work convergence issues arose with the implicit solver of Abaqus 6.14 due to the used contact model, and therefore, only the explicit solver was used.

The determination of the yield point requires a criterion for plastic deformation of the powder compact. Small (or infinitesimal) strain theory is used in the following, since only small strains are considered during yielding of the RVE. This is tantamount to assuming the size of the (undeformed) reference RVE and the (deformed) actual RVE in the reloading step to be identical. The Cauchy stress tensor, which coincides with the first Piola-Kirchhoff stress tensor for small strain theory, is defined as

$$\boldsymbol{\sigma} = \begin{bmatrix} \frac{F_{xx}}{A_x} & \frac{F_{xy}}{A_x} & \frac{F_{xz}}{A_x} \\ \frac{F_{yx}}{A_y} & \frac{F_{yy}}{A_y} & \frac{F_{yz}}{A_y} \\ \frac{F_{zx}}{A_z} & \frac{F_{zy}}{A_z} & \frac{F_{zz}}{A_z} \end{bmatrix} \tag{13}$$

and based on the constraint forces, which are imposed by the constraint equation. The sum of the constraint forces for two parallel faces can be obtained as the reaction force of the auxiliary node, which was used for the corresponding constraint equations. Hence, the three force vectors $\boldsymbol{F}_x, \boldsymbol{F}_y$ and $\boldsymbol{F}_z$ are taken from the three auxiliary nodes and their components are used to compute the stress tensor. Similarly, the strain tensor

$$\boldsymbol{\varepsilon} = \begin{bmatrix} \frac{\Delta u_{xx}}{X} & \frac{1}{2}\left(\frac{\Delta u_{xy}}{X} + \frac{\Delta u_{yx}}{Y}\right) & \frac{1}{2}\left(\frac{\Delta u_{zx}}{Z} + \frac{\Delta u_{xz}}{X}\right) \\ \frac{1}{2}\left(\frac{\Delta u_{xy}}{X} + \frac{\Delta u_{yx}}{Y}\right) & \frac{\Delta u_{yy}}{Y} & \frac{1}{2}\left(\frac{\Delta u_{yz}}{Y} + \frac{\Delta u_{zy}}{Z}\right) \\ \frac{1}{2}\left(\frac{\Delta u_{zx}}{Z} + \frac{\Delta u_{xz}}{X}\right) & \frac{1}{2}\left(\frac{\Delta u_{yz}}{Y} + \frac{\Delta u_{zy}}{Z}\right) & \frac{\Delta u_{zz}}{Z} \end{bmatrix} \tag{14}$$

can be computed based on components of the displacement vectors of the auxiliary nodes $\Delta\boldsymbol{u}_x$, $\Delta\boldsymbol{u}_y$ and $\Delta\boldsymbol{u}_z$. We propose a scalar strain measure for general load cases, which can be used to describe the yielding of a powder. For that we adopt the structure of the von Mises equivalent strain formulation. The von Mises equivalent strain is based on the strain deviator tensor and is often used for metals. The deviatoric strain component is related to distortion, but not to volume change. Since powders can also yield during isostatic compression, we use the full strain tensor instead of the strain deviator tensor to determine the yield point and define the critical plastic equivalent strain for yielding $\varepsilon_{pl,crit}$ as

$$\varepsilon_{pl,crit} = \sqrt{\frac{2}{3}\boldsymbol{\varepsilon}_{yp} : \boldsymbol{\varepsilon}_{yp}} - \sqrt{\frac{2}{3}\boldsymbol{\varepsilon}_{el} : \boldsymbol{\varepsilon}_{el}}. \tag{15}$$

Therefore, the yield point is found by evaluating the plastic equivalent strain of Eq. (15) during probing the RVE in a certain direction. The simulation is stopped as soon as the critical plastic strain for yielding is achieved. The strain tensor at the yield point $\boldsymbol{\varepsilon}_{yp}$ is computed with Eq. (14), i.e., the positions of the RVE's auxiliary nodes at the yield point and in the reference state determine the displacements. The elastic strain tensor $\boldsymbol{\varepsilon}_{el}$ is estimated as the unloading strain after compaction. Hence, the positions of the RVE's auxiliary nodes after compaction and the positions in the reference state determine the displacements for the elastic unloading. The unloading strain after compaction is taken as elastic strain for all yield points since there exists no accurate constitutive equation for the elastic deformation of powders and cyclic probing of the powder tremendously increases the computational costs. However, the contribution of the elastic strain is not crucial anyway and there is no need to determine the elastic strain for each loading direction.

The plastic equivalent strain needs to be negligible (smaller than a user-defined threshold) during elastic loading. If the user-defined threshold of plastic equivalent strain is reached, then the deformation is assumed to be plastic. In the present work the threshold for the plastic equivalent strain was chosen to be 0.002 in analogy to the offset yield point in uniaxial tensile testing, where a plastic strain of 0.2% is used to define the yield strength. The corresponding yield stress tensor of this loading direction is evaluated according to Eq. (13) in a post-processing step.

In the results section of this work (section 3.4) the yield points are plotted in the p-q-plane. The pressure p and the equivalent stress q are computed as functions of the main principal stresses of the stress tensor at the yield point (Eq. (13)):

$$p = \frac{1}{3}(\sigma_{11} + \sigma_{22} + \sigma_{33}) \tag{16}$$

$$q = \sqrt{\frac{1}{2}[(\sigma_{11} - \sigma_{22})^2 + (\sigma_{22} - \sigma_{33})^2 + (\sigma_{33} - \sigma_{11})^2]} \tag{17}$$

Previous studies, such as [59], used the amount of dissipated energy during probing of the yield surface as a yield criterion. This approach has a disadvantage concerning cohesion, which can be explained by a simple example. If we consider a compact with lubricated contacts and low cohesion, then the compact has to be strained severely to obtain a certain amount of energy dissipation. In contrast, if we take a non-lubricated system with high cohesion levels, then only little plastic strain is needed for the same energy dissipation. Hence, we advocate an alternative approach in this work, which takes the plastic strain into account.

In addition, note that the von Mises equivalent strain is based on the strain deviator tensor and is often used for metals. The deviatoric strain component is related to distortion, but not to volume change. Since powders can also yield during isostatic compression, we use the full strain tensor instead of the strain deviator tensor to determine the yield point.

Although a quasi-static problem is considered by the MPFEM, we employ ABAQUS/Explicit as a solver. Hence, dynamic equilibrium equations are solved by a forward Euler algorithm. The explicit algorithm allows for an efficient and robust solution of the contact algorithm problem compared to an implicit algorithm. The drawback of the explicit solver is the limited time increment, since this method is only stable for sufficiently small time steps. Fortunately, it is possible to increase the stable time step by mass scaling. During mass scaling the density of the material is artificially increased without any influence on the results in case of a quasi-static model. The dynamic effect of mass scaling for explicit FEM was investigated in [75] and more recently used in [76] and [77]. As long as there are no inertial effects in the model, it is possible to apply mass scaling. Since finite accelerations are needed to deform and to yield the RVE the maximum mass scaling is limited.

3.3 Convergence Study for the Proposed RVE

The choice of a proper RVE is a subtle task as powder compacts have a complex microstructure. Needless to say, accuracy should be maximized with the least computational effort. The RVE must be large enough to be statistically representative of the powder, such that it effectively includes a sampling of all microstructural heterogeneities. To address these issues, the performance of the proposed RVE is demonstrated by convergence studies. First, a mesh convergence study was conducted to find the minimum mesh fineness. This is followed by a study of the number of particles and their arrangement in the RVE. Finally, the time step size and the influence of mass scaling were investigated.

We chose again a periodic cubic box filled with randomly close-packed, monodisperse spheres (relative density 0.64) obtained from a DEM simulation, as initial packing. Each particle was modeled as an elasto-plastic body, which does not break during deformation. In this work the particles have the material properties of copper, which are summarized in Table 3. The yield stress of the von Mises yield criteria increases as a function of the plastic strain and is defined piecewise linear based on the experimental data given by [78] and [79]. The particles' contact parameters are listed in Table 4. The maximum cohesion interaction length is given as a fraction of the particle diameter $d_{particle}$. For simplicity the diameter of the particles is chosen to be one meter, since it does not influence the properties of the RVE in case of a quasi-static simulation. The value of the damping coefficient was determined by preliminary studies and yielded an optimum in our simulations for a sufficient damping and a negligible influence on the macroscopic yield stress. The particles in the MPFEM model are discretized with standard linear hexahedrons in Abaqus 6.14.

Table 3: Material properties of copper used as particle material

Property	**Value**
Young's modulus	115 GPa
Poisson ratio	0.34
density	8920 kg/m³
σ/ MPa	**$\varepsilon_{plastic}$**
150	0.00
250	0.06
300	0.30
350	1.00
400	2.50
450	5.00

Table 4: Contact properties for convergence studies

Property	**Value**
Contact stiffness k	$1.0 \cdot 10^{12}$ N/m
Coefficient of friction μ	0.2
Maximum cohesion strength c_{max}	100 MPa
Cohesion interaction length δ_0	$0.01 \cdot d_{Particle}$
Damping coefficient d	500 MPa·s/m

The four parameter studies were performed iteratively, since the mesh size, the number of particles, time step size and mass scaling interact with each other. As an example, the maximum time step size for a robust simulation is a function of the finite element size and the density. The maximum mass scaling decreases with an increasing number of particles in the RVE. However, the four parameter studies should verify the suitability of the proposed RVE for powder compaction within acceptable tolerances.

3.3.1 *Mesh Fineness*

The first study addressed the degree of mesh fineness of the particles, which is needed to obtain convergence in the homogenized quantities. We considered an initial packing of 50 particles and compacted the RVE to a relative density of 0.9. The particles were discretized with different mesh fineness. The mesh fineness is defined as the ratio of particle diameter to element size and ranges from 4 to 16 in this study.

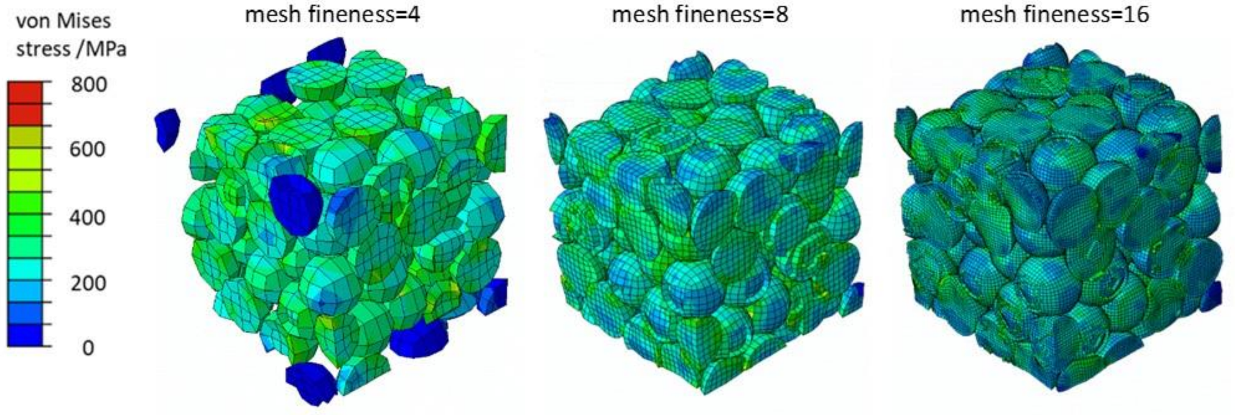

Figure 19: Stress distribution after compaction of 50 particles in the RVE for different finite element discretization.

Figure 19 shows the stress distribution after compaction for three representative meshes based on an identical initial particle packing. In the case of a very coarse mesh the linear elements cannot discretize the shape of the spheres very well. In addition, some of the particles on the boundary are not deformed at all (blue color), since there is no constraint active as the number of coupling nodes is not high enough for at least one of two corresponding particles. The stress distributions for the medium and the fine mesh are comparable by visual inspection. To determine a sufficient mesh fineness, the compact strengths for three different loading cases (uniaxial tension, uniaxial compression and isostatic compression) are plotted as functions of the mesh discretization in Figure 20. It can be clearly seen that the strengths converge for mesh fineness higher than 8 or 10. Since there is only a small deviation in the compact strength (maximum 3.2%) for the mesh fineness of 8 compared to 16, a mesh fineness of 8 was used for the subsequent studies (section 3.4) to keep the computational cost moderate.

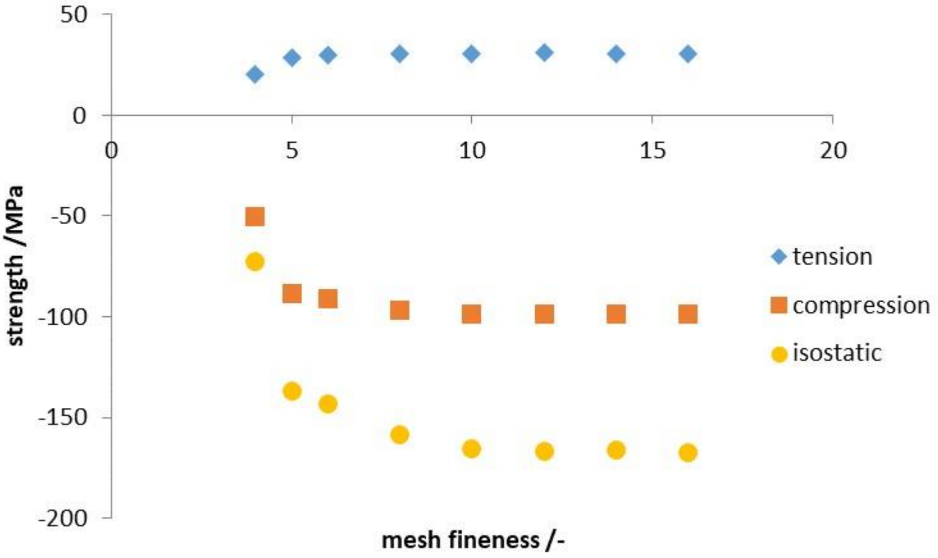

Figure 20: Compact strength of an RVE with 50 particles compacted to a relative density of 0.9.

3.3.2 Particle Number and Particle Distribution

The minimum number of particles to obtain converged quantities for the proposed RVE was investigated next. The RVE must be large enough to be statistically representative of the powder such that all microstructural heterogeneities are sufficiently sampled. Particle numbers ranging from 10 to 2000 particles were considered. As only a small number of particles can be practically considered in the MPFEM, the packing distribution itself will have a large influence on the results. Hence, we chose ten different packing realizations for each particle number and computed the average. The RVE was compacted again to a relative density of 0.9. In Figure 21 three particle packings with different particle numbers are shown for illustration purposes.

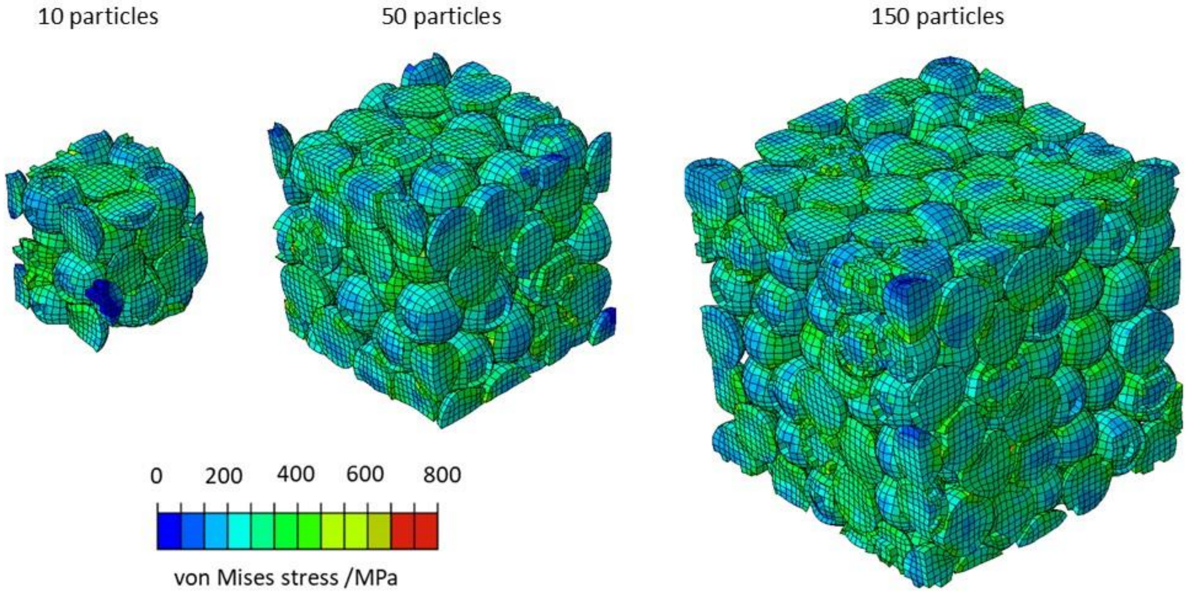

Figure 21: Stress distribution after compaction of different numbers of particles inside the RVE.

The computed compact strengths of the three loading cases are shown for all packings in Figure 22 as black crosses. In addition to that, the average compact strength as a function of the number of particles and the three loading cases is plotted by a filled symbol. We clearly observe that with an increasing number of particles the average strengths converge towards a nearly constant value. There is a slight increase of the yield strength above 100 particles what may be due to inertial effects. The mass scaling factor used in this study was determined for a system of 50 particles (see section 3.3.4) and is rather too high for packings with several hundred particles. Interestingly, the results for the particle packing with 10 particles are closer to the converged results than for 20 particles. The random arrangement of 20 particles in this simulation is apparently not sufficient for modelling an infinite particle packing. Besides, a low particle number (smaller than 50) gives a very wide scattering of the results. Figure 23 presents the relative standard deviation (RSD) shown for different particle numbers and loading cases. The RSD decreases with an increasing particle number. We observe that beyond 100 particles the RSD is limited to a range from 0 to 0.05. It is noteworthy that the RSD is higher for uniaxial compression compared to isostatic compression and uniaxial tension. According to this convergence study and due to computational reasons we used a packing of 50 particles for further simulations.

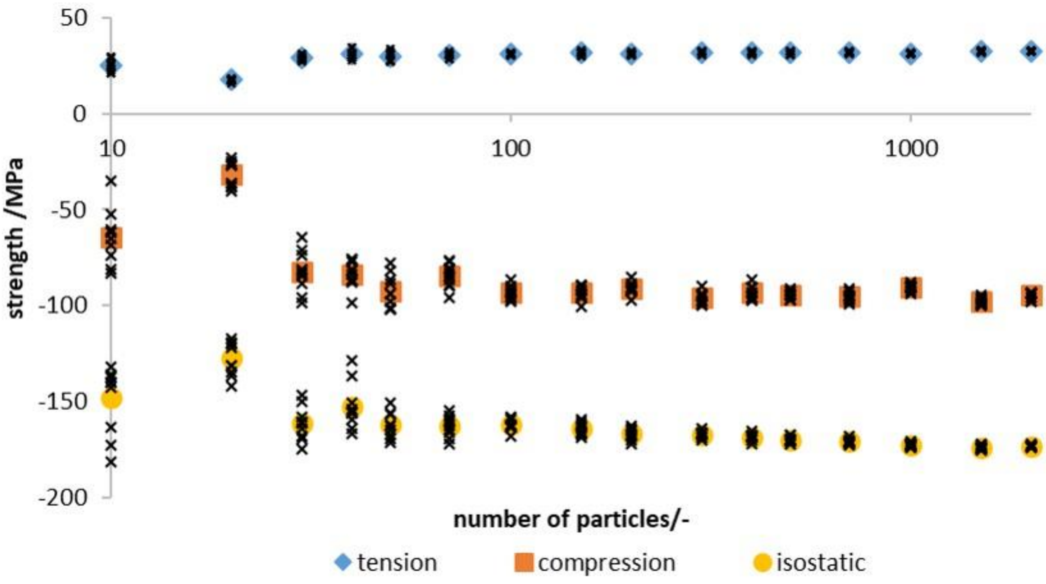

Figure 22: Strength for different particle packings compacted to a relative density of 0.9. Every single compact strength is plotted as a cross, whereas the average strength for the same particle number is plotted with filled symbols.

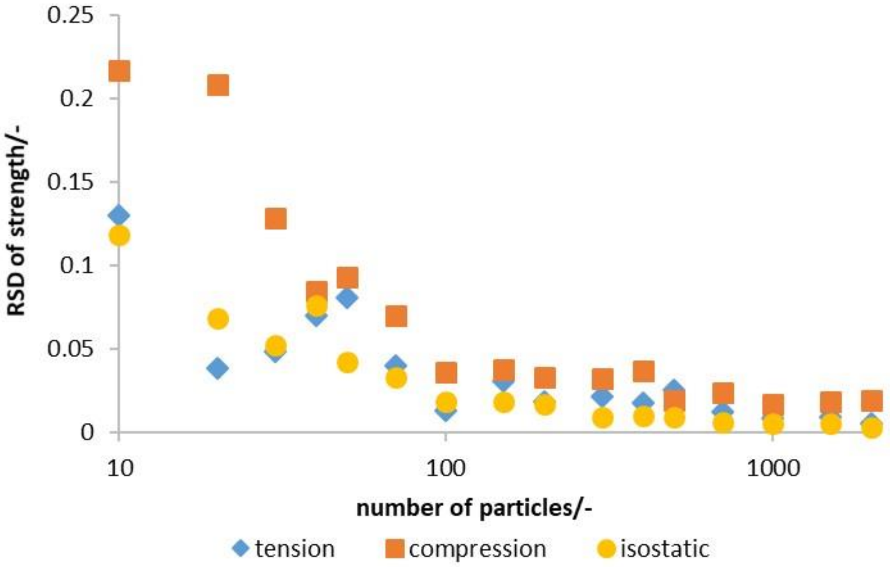

Figure 23: Relative standard deviation of the compact strengths for different loading cases as a function of the particle number.

3.3.3 *Time Step Size*

The presented MPFEM is designed for the implementation in commercially available FEM software packages. The complex contact problem involved in the MPFEM advocates the use of an explicit integration scheme in these packages. As we opt for ABAQUS/Explicit, the homogenized compact strength will be dependent on the simulation time step size. To determine its influence, we considered an RVE populated with 50 particles and a mesh fineness of 8 and investigated three different loading cases. The simulation time step was varied from 0.01 to 1ms, while the mass scaling factor was kept constant at 10000. Time step sizes larger than 1ms resulted in an unstable simulation. As can be seen in Figure 24, the results are rather insensitive to the size of the time step, although a deviation of 8.5% for the largest time step compared to the smallest time step for uniaxial compression is obtained. We chose a size of 0.1ms for the convergence study of the mesh and the mass scaling to obtain stable simulations for a big range of the mesh fineness and the mass scaling factor. A higher step size of 0.5ms is used during convergence study of the number of particles and the subsequent simulation studies of the yield properties.

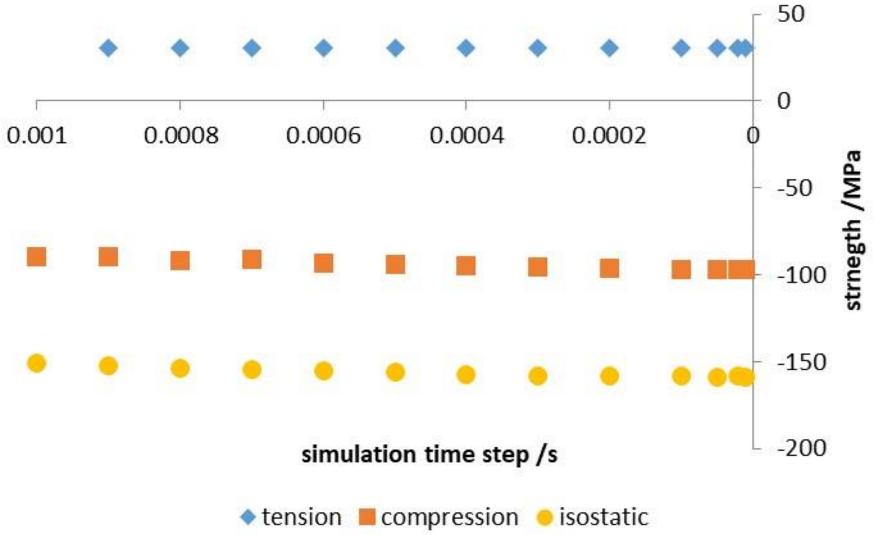

Figure 24: Strength of a 50-particle RVE compacted to a relative density of 0.9 for different loading cases as a function of the simulation time step.

3.3.4 *Mass Scaling*

A parameter study for the maximum factor of mass scaling was performed. Mass scaling multiplies the original density by a factor to give a new artificial density, which optimizes the solution of the quasi-static problem. We considered an RVE with 50 particles, initial packing density of 0.64 and a mesh fineness of 8 and investigated a compaction to a relative density of 0.9, considering three different loading cases (uniaxial tension, uniaxial compression and isostatic compression). First we used a time step size of 1µs and no mass scaling. The used time step of 1µs was found during a convergence study in which the time step was stepwise reduced until the result was constant. The resulting compact strengths are given in Figure 25 as horizontal lines. We increase the time step to 0.1ms to speed up the simulation. However, this requires a mass scaling as the simulation is not stable while using the original density. The mass scaling factor was varied between 200 and 70,000. Smaller factors than 200 resulted in unstable simulations for the chosen time step size. We note that too low scaling factor result in stability problems or imprecise results, while too high scaling factors cause artificial inertia effects.

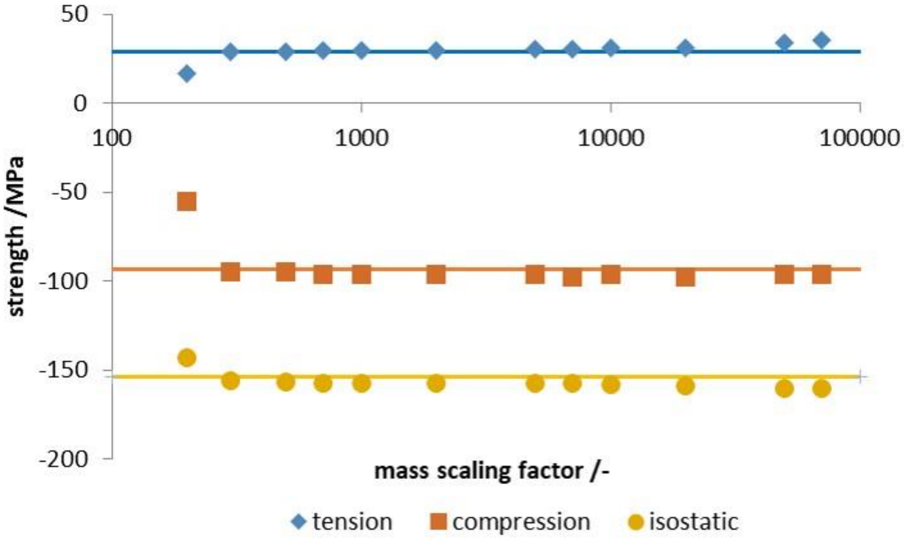

Figure 25: Strength of a 50-particle RVE compacted to a relative density of 0.9 for different loading cases as a function of the mass scaling factor. The horizontal lines indicate the strength without mass scaling.

Figure 25 shows in addition the compact strength as a function of the mass scaling factor for a time step size of 0.1ms. Mass scaling factors between 300 and 10,000 result in compact strengths that are nearly constant and match the target strength obtained without mass scaling, although the strength is slightly overestimated during mass scaling. Possibly, minor inertial effects cause a delay of yielding, and therefore, increase the apparent yield strength. If the mass scaling factor exceeds 10,000, the deviations increase noticeable. This effect is more dominant for tension than for compression. This is to be expected, as the cohesive bonds break under tensile load and the particles have to be accelerated. To limit this inertial effect a mass scaling factor of 10,000 is used for all subsequent simulation studies with a time step size of 0.1ms.

3.4 MPFEM for Obtaining the Yield Properties of Compacted Powders

3.4.1 Uniaxial Strength of Powder after Isostatic Compaction

The dependence of the uniaxial strength on different relative densities after compaction was studied. We used RVEs with 50 particles, an initial relative packing density of 0.64, a mesh fineness of 8, a mass scaling factor of 10,000 and a simulation time step of 0.5ms. Three different initial packing arrangements were considered for each case and averages were computed. The system was isostatically compacted to packing densities ranging from 0.65 to 0.95. Figure 26 shows the stress distribution inside one RVE after compaction to different relative densities.

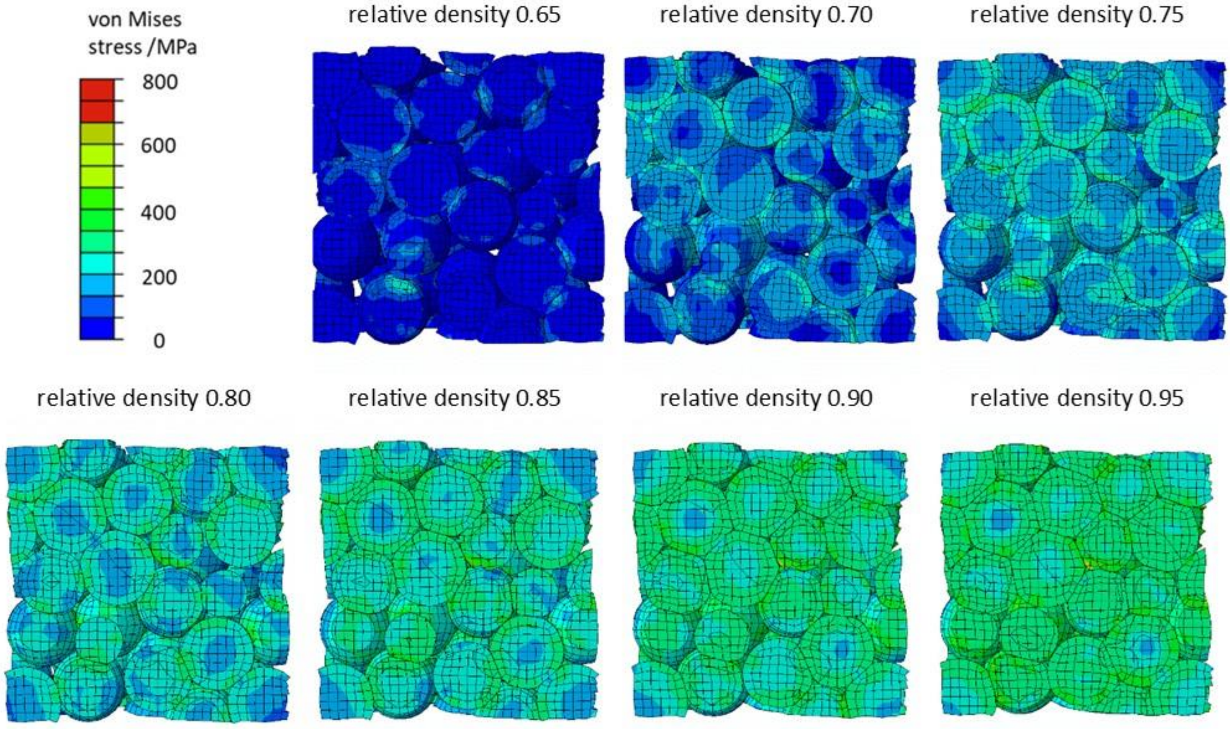

Figure 26: Stress distribution inside an RVE's cross section after compacting to different relative densities.

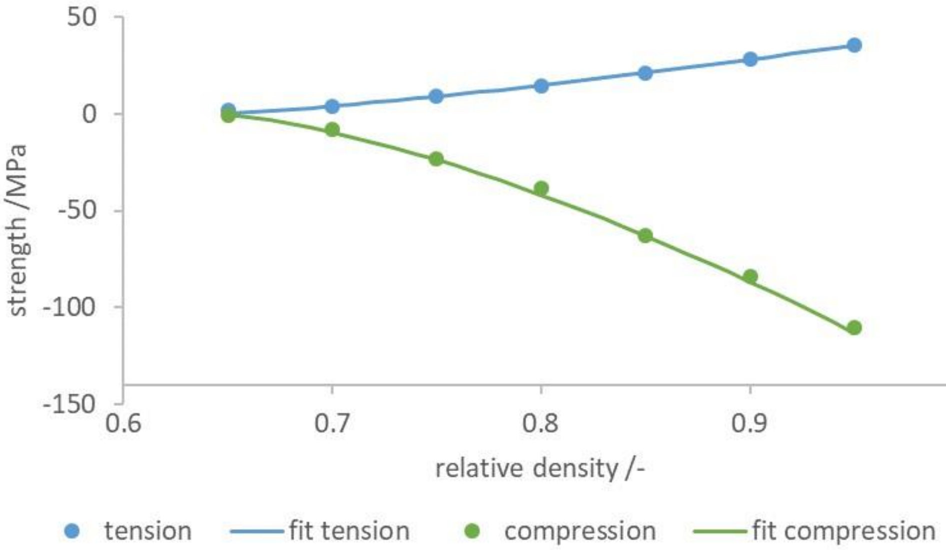

Figure 27: Uniaxial strength as a function of the relative density with a constant cohesion interaction strength of 100 MPa.

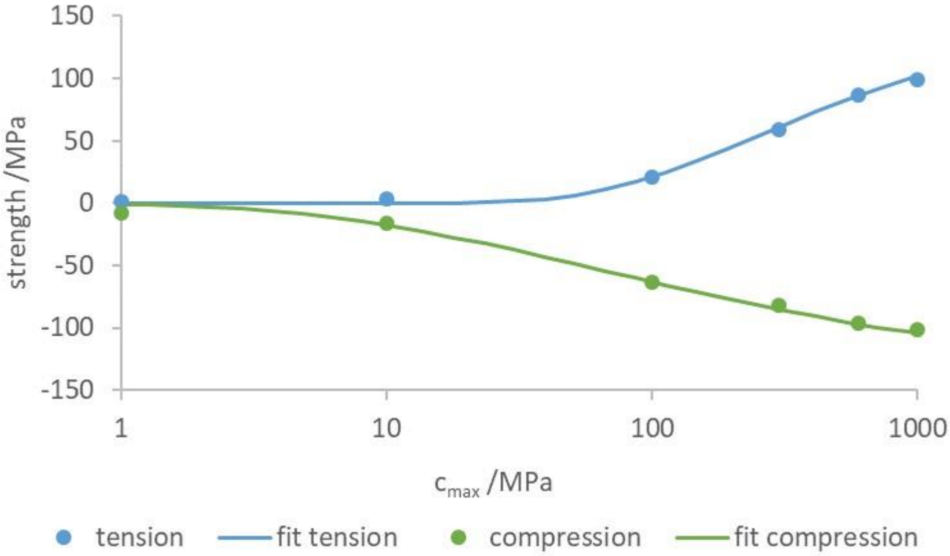

Figure 28: Uniaxial strength as a function of the cohesion interaction strength with a constant relative density of 0.85.

Figure 27 shows the uniaxial strength as a function of the relative density after compaction. Tensile strength is stated as positive and compression strength is negative. The simulation results are plotted as filled points. Every point describes the average uniaxial strength of three different RVEs compacted to the same relative density. In addition, a parameter study with different cohesion strengths was performed with a constant relative density of 0.85. The results are shown in Figure 28. It is possible to fit the numerically obtained uniaxial yield strength shown in Figure 14 and 15 by means of an analytical equation:

$$\sigma_{uniaxial} = a \cdot \left(\rho_{rel} - \rho_{rel,0}\right)^{b} \cdot \exp\left(-\left(\frac{c}{c_{max}}\right)^{d}\right). \tag{18}$$

The equation consists of a scaling factor a, another prefactor, which describes the influence of the current relative density ρ_{rel} compared to the initial relative density $\rho_{rel,0}$, and an exponential term, which includes the influence of the maximum cohesion strength c_{max}. The exponential term saturates at high cohesion strength and hence, it is possible to model contact failure at low cohesion strength and failure of the particle material at high cohesion strength. Theoretically, the saturation cohesion strength c should be in the order of the yield strength of the base material. It is supposed to have negligible yield strength for packing densities below random closed packing of spheres ($\rho_{rel,0} = 0.64$) since contact surfaces between spheres are only formed above this threshold. Furthermore, two additional parameters b and d are introduced to improve the flexibility of the fitting.

Least square regression analyses resulted in the factors a, b, c and d. The analytical expression for the tensile strength (in MPa) equals

$$\sigma_{tension} = 1180 \cdot (\rho_{rel} - 0.64)^{1.33} \cdot \exp\left(-\left(\frac{255.5}{c_{max}}\right)^{0.71}\right), \tag{19}$$

while the analytical expression for the compression strength (in MPa) is

$$\sigma_{compression} = -1530 \cdot (\rho_{rel} - 0.64)^{1.50} \cdot \exp\left(-\left(\frac{65.3}{c_{max}}\right)^{0.40}\right). \tag{20}$$

The regression curves fit the numerically obtained strengths very well as it can be seen in Figure 27 and Figure 28. Interestingly, the saturation cohesion strength c for uniaxial tension is 255.5 MPa while it is only 65.3 MPa for uniaxial compression. The yield strength of the base material of 150 MPa lies in between the saturation cohesion strength for tension and compression. This is reasonable, since contact failure is influenced by the loading direction while yielding of the base material is the same for tension and compression. The contact surfaces are compressed towards each other during compressive load, which strengthens cohesive interactions and plastic deformation of the base material occurs rather than contact sliding. In contrast, during tensile load contact surfaces are pulled apart from each other, acting against the cohesion interaction. In this case a higher cohesion strength is needed to obtain plastic flow of the base material.

The analytical description allows for a quick estimation of the strength based on numerical results of the MPFEM. This simplifies the incorporation of the proposed strategy into technologically relevant processes. Of course the presented results are only valid for the considered system of monodisperse copper-like particles. The coefficients may differ for other systems and additional simulations are needed to describe the yield strength for other materials.

3.4.2 Yield Surfaces

For the description of powder compacts via continuum models a properly defined yield surface is needed. As we investigate the influence of cohesion on the yield surfaces in this article, we take a general form of the yield surface in the p-q-plane (hydrostatic pressure p, equivalent stress q) as a basis. We use the following form:

$$q = \left(\frac{(a^2 - (p - p_m)^2)^{0.5}}{r}\right) \cdot (j \cdot (p - t)^2 + k \cdot (p - t) + 1). \tag{21}$$

Eq. (21) can be divided into two parts. The first part describes an ellipse with a midpoint at the pressure p_m, the horizontal semi axis a and r, which is defined as the ratio of the two semi axes a/b. The second part is a quadratic polynomial with factors j, k and t, which change the shape and the position of the ellipse in stress space. A schematic example of the yield surface in stress space is shown in Figure 29.

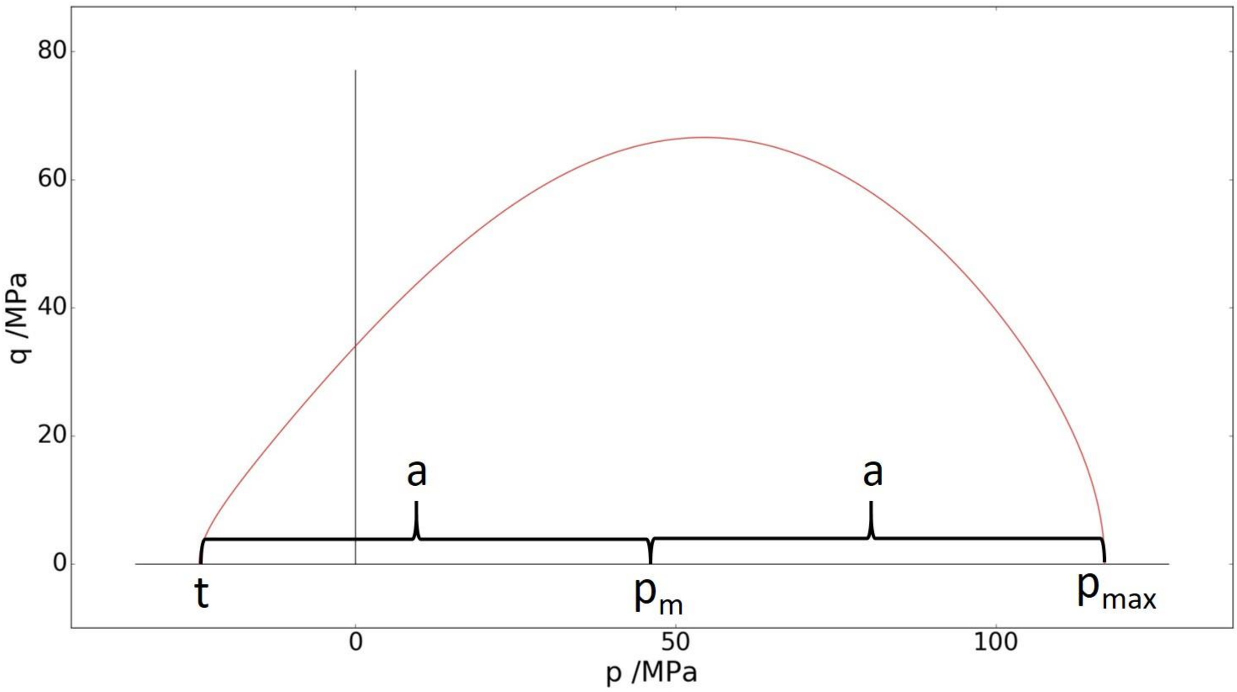

Figure 29: Schematic representation of the proposed form of the yield surface

We employ the same RVEs as in the previous section and consider again averages of three different initial packing arrangements. The yield surfaces are numerically probed and the parameters in Eq. (21) are obtained by curve fitting to obtain an analytical description of the yield surface.

Figure 30 presents the numerically obtained yield surfaces for different relative densities with a constant cohesion strength (filled points). As expected, the size of the yield surfaces increases with increasing relative density, while the shape remains approximately constant. The solid lines are least-square error fits of Eq. (21) to the discrete data points. Table 5 summarizes the regression data. As can be seen in the figure, a very good fit is achieved. During regression an isotropic yield behavior of the powder and a circular shape of the yield surface in the deviatoric cross section was assumed. In this case a certain yield point, which is a function of the pressure, has to be independent of the loading direction. The same pressure can be achieved for different loading directions as can be seen in Eq. (16). The yield points in Figure 30 are only slightly scattered, although the strength was tested in different loading directions. Consequently, the assumption of isotropic yield behavior is valid in case of isostatic compaction.

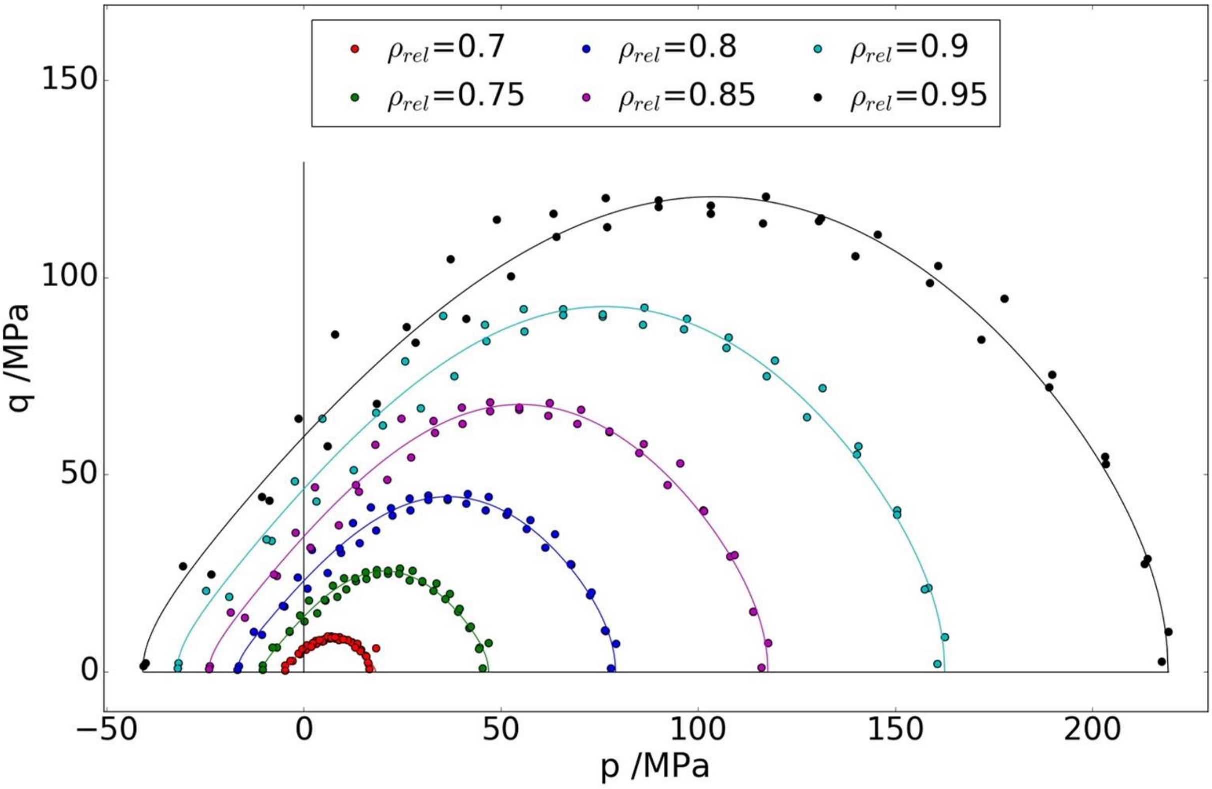

Figure 30: Evolution of the yield surfaces as a function of the relative density with a constant cohesion strength of 100 MPa

Table 5: Parameters of the yield surface as a function of the relative density for a constant cohesion strength of 100 MPa.

ρ_{rel} /-	p_{max} /MPa	t /MPa	a /MPa	p_m /MPa	r /-	k /MPa^{-1}	j /MPa^{-2}
0.7	18.2	4.8	11.5	6.7	1.344	0.021	-4.38E-03
0.75	46.9	10.5	28.7	18.2	1.227	0.016	-6.23E-04
0.8	79.1	16.9	48.0	31.1	1.216	0.011	-1.97E-04
0.85	117.7	24.1	70.9	46.8	1.190	0.008	-9.20E-05
0.9	162.6	32.1	97.3	65.2	1.206	0.006	-4.73E-05
0.95	219.2	40.8	130.0	89.2	1.249	0.004	-2.51E-05

Figure 31 depicts the numerically modeled yield surfaces as a function of the cohesion strength with a constant relative density of 0.85. An interesting behavior can be observed here: Low cohesion strengths cause yield surfaces that match the shape of the Drucker-Prager/Cap model.

In contrast, high cohesion strengths result in an elliptical shape. The ellipse is remarkably similar to the isotropic constitutive model for the plastic behavior of metallic foams developed by [56]. The center of the ellipse is close to a pressure of zero, which requires the isostatic compressive strength to be equal to the isostatic tensile strength. Such a behavior can be physically motivated, if particles are compressed into each other in a hydrostatic manner and they are practically bonded due to very high cohesion. Then little or no contact sliding and particle rearrangement is expected. In this case the plastic yielding of the particles is mainly responsible for the deformation of the powder, which renders the powder's behavior similar to a foam or porous material. The solid lines are again least-square error fits of Eq. (21) to the discrete data points, the regression data are shown in Table 6. Once more, a very good match is obtained.

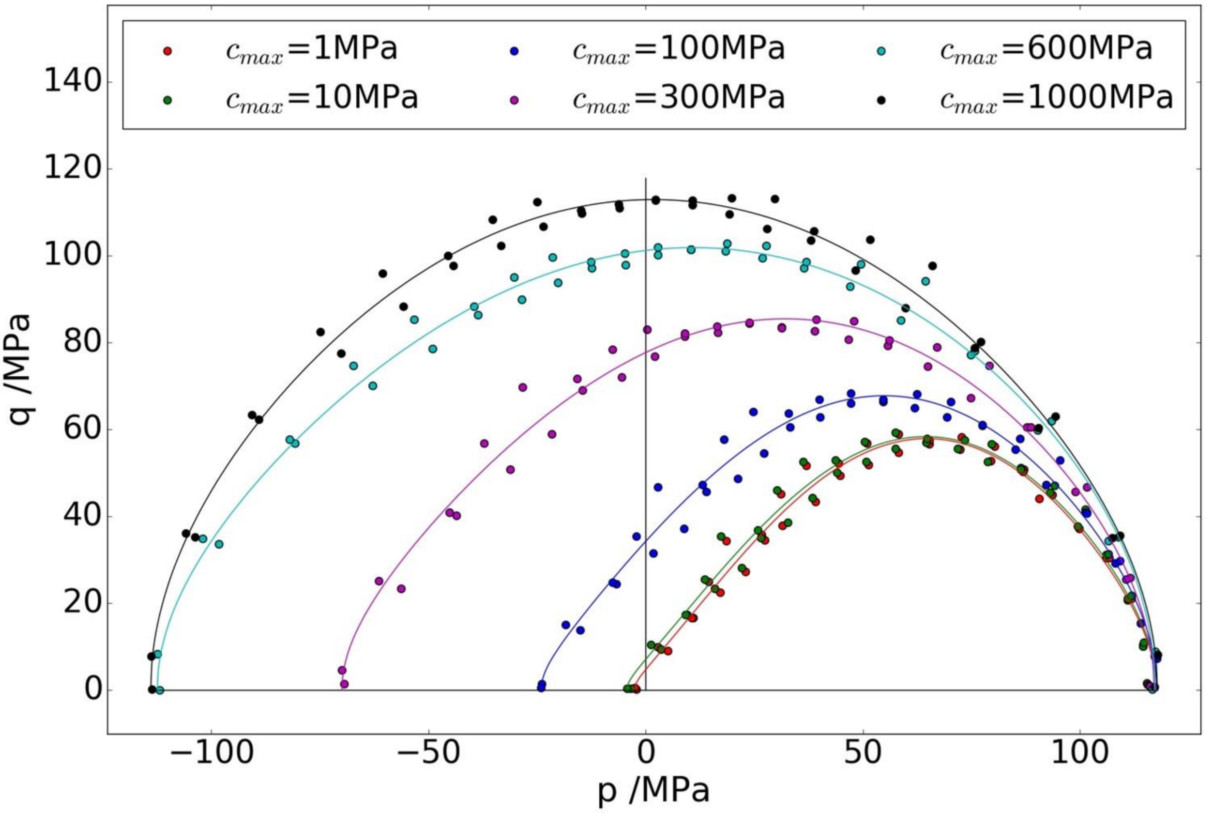

Figure 31: Yield surfaces as function of the cohesion strength with a constant relative density of 0.85

Table 6: Parameters of the yield surface as a function of the cohesion strength for a constant relative density of 0.85.

c_{max} /MPa	p_{max} /MPa	t /MPa	a /MPa	p_m /MPa	r /-	k /MPa^{-1}	j /MPa^{-2}
1	117.6	2.6	60.1	57.5	3.137	0.060	-4.31E-04
10	117.7	4.3	61.0	56.7	2.573	0.044	-3.23E-04
100	117.7	24.1	70.9	46.8	1.190	0.008	-9.20E-05
300	117.1	69.9	93.5	23.6	1.099	-0.001	-3.22E-05
600	117.3	112.5	114.9	2.4	1.237	-0.003	-1.67E-05
1000	117.8	114.0	115.9	1.9	1.257	-0.004	-1.76E-05

To get a deeper understanding of the failure mode in the compact, the effect of the coefficients of friction was studied. The relative density was kept constant and three different cohesion strengths ranging from very low to very high were investigated (see Figure 32 to Figure 34 and Table 7 to Table 9). As can be seen, the coefficient of friction has no influence on the isostatic strength (neither for compressive nor for tensile load). However, if the RVE is probed in a non-isostatic way, the coefficient of friction becomes important as can be seen in Figure 32 and Figure 33. In this case sliding between particles is responsible for powder yielding. Interestingly, in case of very high cohesion strengths (see Figure 34) the yield surfaces approach each other for coefficients of friction of at least 0.2. Here, plastic yielding of the particles is again responsible for the powder yielding, since particle sliding is inhibited due to high cohesion and friction.

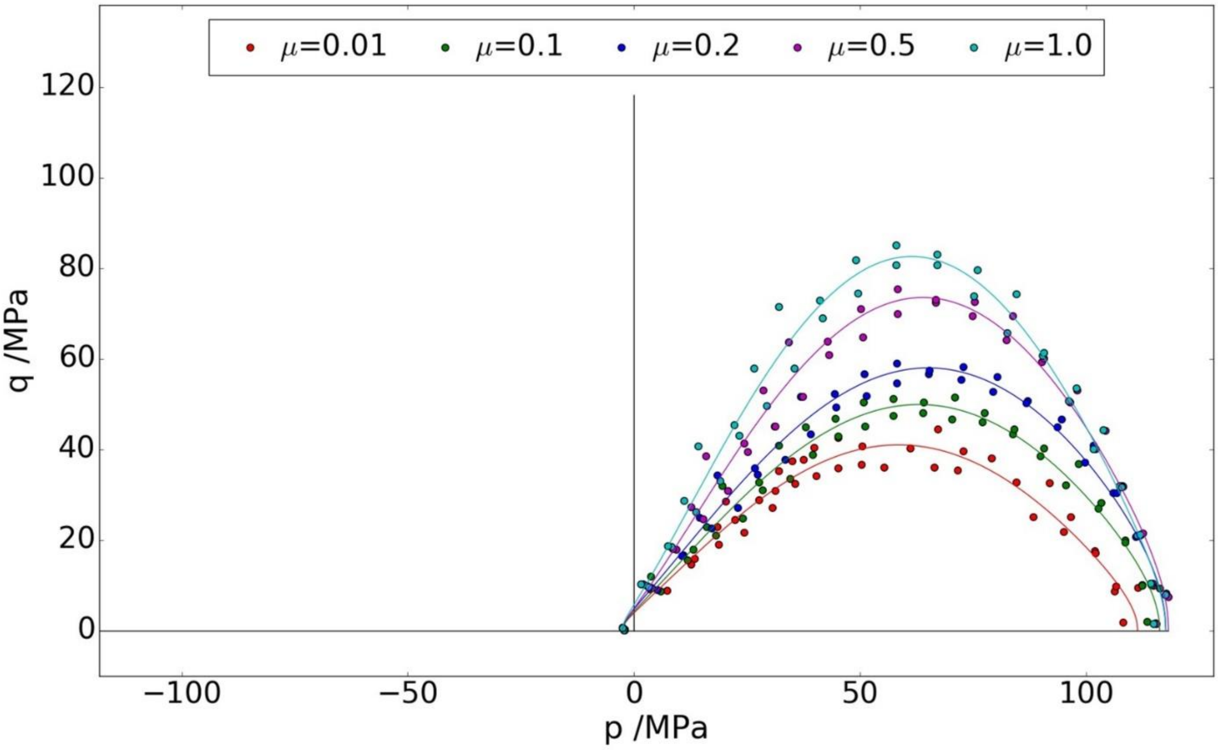

Figure 32: Yield surfaces as a function of coefficient of friction with a constant relative density of 0.85 and a cohesion strength of 1 MPa

Table 7: Parameters of the yield surface as a function of the coefficient of friction for a constant relative density of 0.85 and a cohesion strength of 1 MPa.

coef. of friction /-	p_{max} /MPa	t /MPa	a /MPa	p_m /MPa	r /-	k /MPa^{-1}	j /MPa^{-2}
0.01	111.4	2.6	57.0	54.4	3.735	0.057	-4.81E-04
0.1	116.2	2.5	59.4	56.9	3.492	0.059	-4.46E-04
0.2	117.6	2.6	60.1	57.5	3.156	0.060	-4.26E-04
0.5	118.2	2.6	60.4	57.8	2.897	0.077	-5.81E-04
1	117.6	2.6	60.1	57.5	2.456	0.077	-6.26E-04

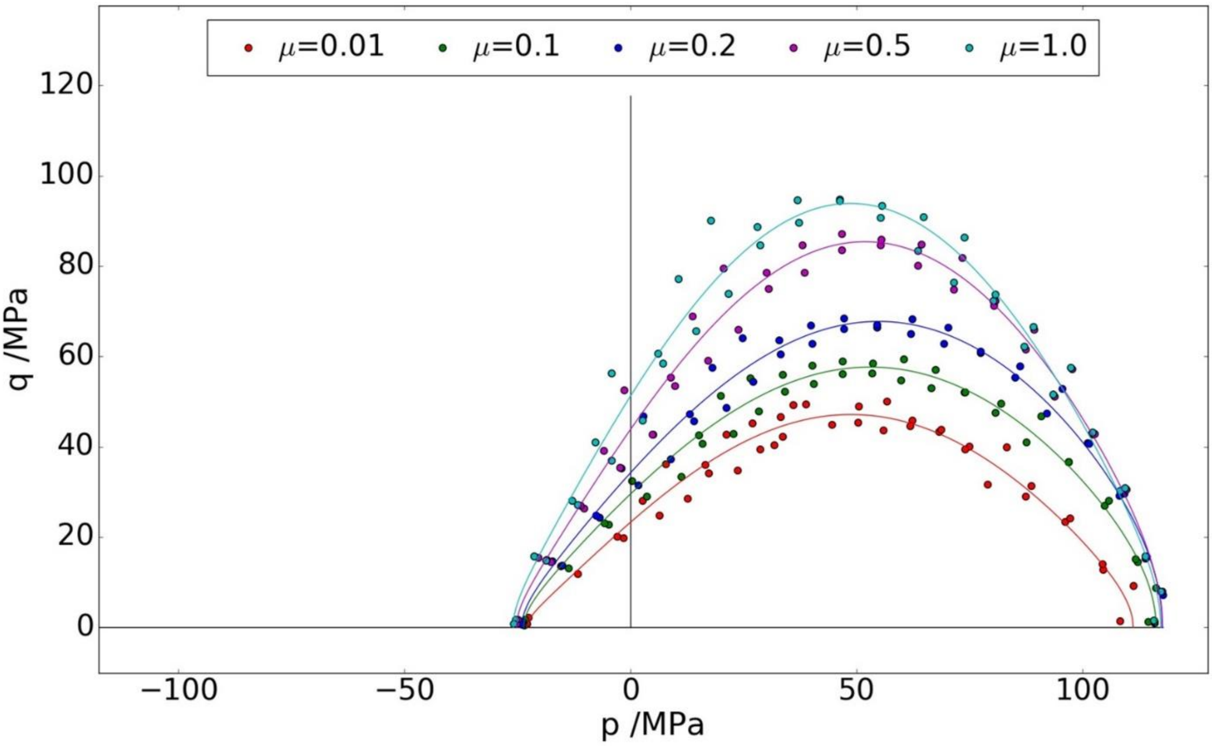

Figure 33: Yield surfaces as a function of the coefficient of friction with a constant relative density of 0.85 and a cohesion strength of 100 MPa

Table 8: Parameters of the yield surface as a function of the coefficient of friction for a constant relative density of 0.85 and a cohesion strength of 100 MPa.

coef. of friction /-	p_{max} /MPa	t /MPa	a /MPa	p_m /MPa	r /-	k /MPa^{-1}	j /MPa^{-2}
0.01	111.2	22.9	67.0	44.2	1.594	0.008	-1.39E-04
0.1	116.3	23.6	70.0	46.3	1.367	0.007	-9.86E-05
0.2	117.7	24.1	70.9	46.8	1.190	0.008	-9.20E-05
0.5	117.6	25.2	71.4	46.2	0.928	0.007	-1.12E-04
1	117.3	25.9	71.6	45.7	0.821	0.006	-1.20E-04

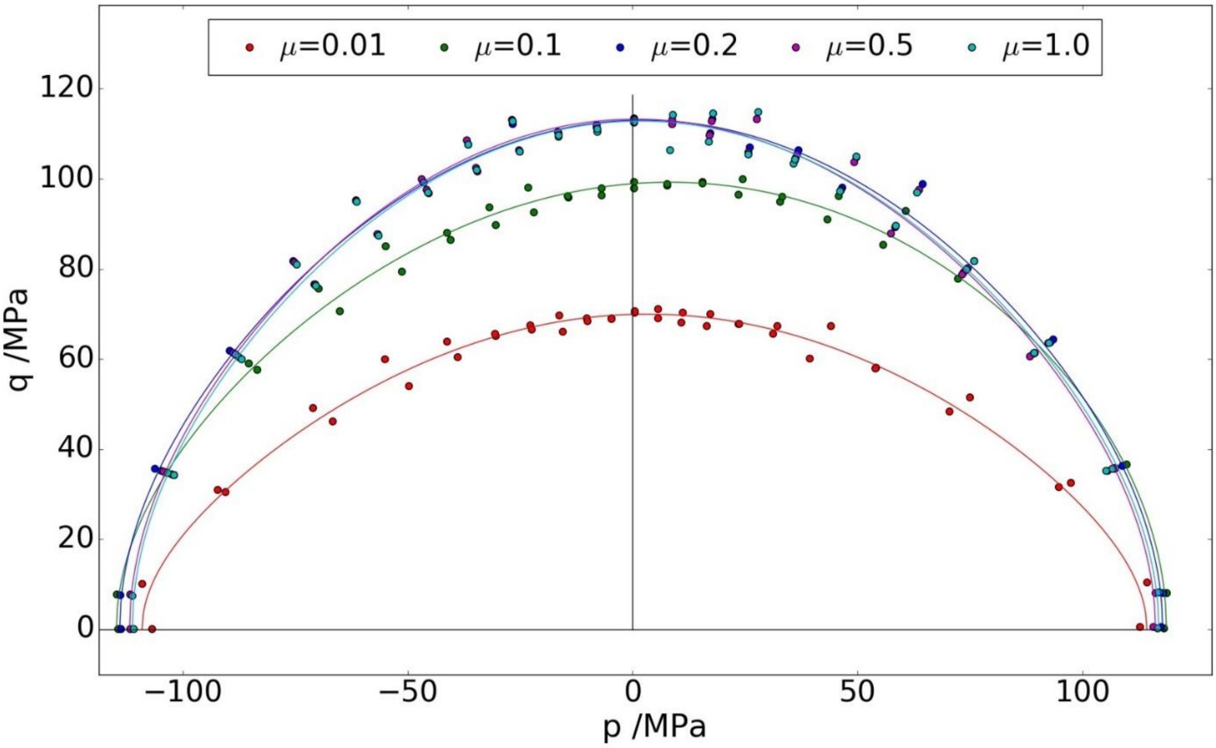

Figure 34: Yield surfaces as a function of the coefficient of friction with a constant relative density of 0.85 and a cohesion strength of 1000 MPa

Table 9: Parameters of the yield surface as a function of the coefficient of friction for a constant relative density of 0.85 and a cohesion strength of 1000 MPa.

coef. of friction /-	**p_{max} /MPa**	**t /MPa**	**a /MPa**	**p_m /MPa**	**r /-**	**k /MPa^{-1}**	**j /MPa^{-2}**
0.01	114.3	109.0	111.6	2.6	2.119	-0.006	-2.99E-05
0.1	118.7	114.7	116.7	2.0	1.258	-0.002	-1.10E-05
0.2	117.8	114.0	115.9	1.9	1.260	-0.004	-1.86E-05
0.5	116.2	111.8	114.0	2.2	1.276	-0.005	-2.03E-05
1	116.9	111.2	114.1	2.9	1.266	-0.004	-1.99E-05

The investigation of the yield surfaces for different contact parameters can be summarized as follows:

During compaction the yield surface grows, but the shape remains constant for constant contact parameters.

For low cohesion strength the Drucker-Prager/Cap model is appropriate. For very high cohesion strength the yield surface can be described with an ellipse, which is symmetric with respect to the q-axis (the metallic foam model with isotropic hardening is appropriate). An analytical equation is given capturing both shapes.

The frictional constants are not relevant for isostatic compression or in case of very high cohesion strengths combined with coefficients of friction exceeding 0.2. In both cases there is no contact failure since contacts simply stick to each other.

If the state of stress is not isostatic and the cohesion strength is small compared to the particles' material strength, then contact sliding is the failure mode.

3.5 Conclusion and Outlook

This work introduces an efficient RVE for the compaction of a monodisperse powder with the MPFEM. In contrast to earlier studies, such as [59] and [72], cohesion is considered in the particles' contact, which allows to describe tensile strength after compaction. The present article shows the influence of different cohesion strengths on the yield surface of compacted powder.

A new way of incorporating periodic boundary conditions is presented. Each boundary particle is assigned with a reference point and the nodes of the finite element mesh of this boundary particle within an add-on layer are coupled with the reference point via distributing coupling. This manner of modeling allows for the incorporation of cohesive contact to the boundary particles, which is essential for this study. As a result, a robust MPFEM ready for the implementation into existing FEM codes is obtained.

We present several convergence studies to justify the performance of the proposed RVE. This is an important step since an RVE of compacted powder is only useful if convergence of the macroscopic yield properties can be obtained. To the best knowledge of the authors no comparable convergence study was reported in the literature which showed convergence of a MPFEM RVE. The mesh fineness, the ratio of the diameter of the spherical particles and the size of the finite elements, has to be chosen to equal 8 or higher to avoid mesh effects. Different particle arrangements have a significant influence on the homogenized results. The scatter decreases with an increasing particle number, but is still observable for RVEs with 300 particles. Therefore, it is necessary to simulate a couple of different particle arrangements with the same particles' properties to determine average RVE properties. The required number of particles and the minimum mesh fineness of the FEM model determine to a large extent the computational costs for a single time step. The number of time steps is a function of the total process time and the simulation time step. The maximum simulation time step may be increased by mass scaling for quasi-static problems. If the process time for the compaction step is 6s, then a mass scaling factor of 10,000 can be used without the introduction of unwanted inertial effects. In this situation a robust simulation time step equals 0.5ms.

The proposed MPFEM is designed to be efficiently implemented into an existing finite element software. One compaction step of our reference model (50 particles and mesh fineness of 8) can be solved in parallel on three CPU cores in approximately 50 minutes.

The model allows to run multiple parameter studies. Hence it is possible to determine the uniaxial yield strength and complete yield surfaces as a function of the compact density and the cohesion strength. The numerically obtained uniaxial tensile strength and the uniaxial compression strength are described by analytical equations, which include the relative density and the cohesion strength. We are even capable of describing yield surfaces based on different contact properties and relative densities by using the numerical model. Again, an analytical form is given to match the numerical results. Hence, the same material model could be used to describe weak cohesion during cold compaction of a powder and strong cohesion (or bonding) of the powder after subsequent sintering.

The existing work demonstrates the possibilities of MPFEM for compaction simulations. Nevertheless, many further steps are necessary to fully exploit the possibilities of this method in the future. First of all, the simulation results have to be compared to experimental results, such as in [80]. Non-ideal conditions in the experiments (non-spherical particles, slightly polydisperse, etc.) have to be taken into account to describe real powders. Next, different compaction modes could be considered in future work, which might lead to the observation of anisotropic material properties of the compacted powder what was already observed experimentally in [81]. Especially closed-die compaction should be considered, since it is representative for many industrial compaction processes. Different base materials could be investigated to elucidate the influence of their yield properties on the yield properties of the compacted powder. Contact modeling and the identification of sufficient contact model parameters for a certain material is another story and must be solved in a future work. In addition to the yield surface considered in this work the MPFEM can also be used to investigate the flow rule to see how the material flows upon yielding. Moreover, the Young's modulus, which is needed to describe the elastic behavior of the compacted powder, should be considered. As a result, all macroscopic properties of the compacted powder could be determined by the MPFEM, which are then used in a continuum model to simulate macroscopic parts under stress and deformation.

4 Prediction of the Anisotropic Mechanical Properties of Compacted Powders[c]

Abstract: The multi-particle finite element method (MPFEM) was used to test the anisotropic elastic and plastic properties of compacted powders with cohesive contacts. A representative volume element (RVE) of monodisperse, spherical, deformable particles was used to investigate the powder properties after compaction. Efficient periodic boundary conditions and an RVE of only 50 particles allowed extensive parameter studies. During parameter studies the relative density after compaction, the contact cohesion strength and the strain path during compaction were varied. The strain paths were characterized by the ratios of the applied principal strains during compaction that results in different Dirichlet boundary conditions on the RVE. Seven different strain paths were considered including the practically important isostatic and closed die compaction.

The outcome of the parameter study were the elastic constants of an orthotropic material model, the uniaxial yield strength for tension and compression, and the yield surfaces for general load cases. No anisotropy was observed for isostatic compaction but increasing anisotropy was observed with increasing ratio of the principal strains during compaction. Regression curves were generated to describe the mechanical properties as a function of the model parameters. In this way, continuous functions were obtained which were capable to describe the distribution of the mechanical material properties in a FEM model of a heterogeneous compacted powder part.

---

[c] This section is based on the journal article “Prediction of the anisotropic mechanical properties of compacted powders” by Loidolt et al. in Powder Technology 2018

4.1 Introduction

Compaction of powders is a very common industrial process. It is used for producing green bodies before sintering a metallic or ceramic part, to produce pellets of minerals or animal food or to manufacture tablets in the pharmaceutical industry [31–34]. The requirements depend on the application: for example, the total mass and its uniformity is crucial in the pharmaceutical industry, whereas shape of the parts is essential for structural parts in mechanical engineering. The properties of the compacted powder depend on the particle properties, such as particle size and shape, the mechanical features of the particles and the particle-surface properties. In addition to that the process conditions during compaction play a major role. The geometry and the surface of the tools, as well as the load control during compaction, are three of the most important influencing factors of the process.

Simulations are an important tool, next to experiments, to understand the details of a process and to optimize powder compaction. The advantage of process optimization via simulation is the possibility to perform extensive parameter studies without any investment costs for prototypes. The drawback of simulation is the simplification of the real system that requires the identification of assumedly negligible effects on the system to set up a suitable model. Suitable models are not well established for powder materials. There are some very basic phenomenological models available which correlate the applied pressure with the relative density or porosity of a powder (compressibility), e.g. the Heckel [35] and Kawakita [36] equations. Other models correlate the relative density of a powder compact with its strength (compactability) [40]. The constants of these models differ from powder to powder and have to be estimated during compaction experiments by force measurement. The benefit of these models is limited, since there is no spatial resolution which may be crucial for a complex stress distribution inside the part. Furthermore, the gain of mechanical understanding is marginal.

In opposite to the simple phenomenological models, the compaction processes can as well be described by means of simple mechanical models as proposed in [44] and [43]. In these studies, yield surfaces for powders are derived analytically. Compaction and sintering is analyzed theoretically in the work of [45]. The drawback of analytical models is the need of many simplifications as it is not possible to consider rearrangement and deformation of particles within these models.

Due to the availability of high-performance computers the application of numerical methods became more common in recent years. In the field of powder simulations, the discrete element method (DEM) and the finite element method (FEM) are used. In a DEM model the position of every particle is tracked. If two particles (theoretically) overlap, a contact force is computed as a function of the overlap. The particles are accelerated by the sum of all contact forces and the position of the particles is calculated based on the Newton’s equations of motion. In this way rearrangement of particles is considered. With efficient codes, this method can be used to model up to many millions of particles [82,83]. Still, in most cases the number of particles inside the process is too high to be captured by a DEM model. Furthermore, the deformation of particles cannot be considered effectively in DEM. In contrast to DEM, the number of particles is no issue in a FEM simulation since the powder is considered as a continuum. Therefore, individual particles are not considered, but the powder is assumed to have field properties which are distributed continuously, e.g., density, stress and strain. During a FEM simulation the stress inside the part is computed as a function of the strain. In Eq. (22) the stress-strain relation is written in the Voigt matrix notation (symmetric tensors are denoted as vectors) where C_{ij} is the 6x6 elasticity tensor. The inverse relation is shown in Eq. (23) where S_{ij} is the compliance tensor.

$$\boldsymbol{\sigma_i = C_{ij}\varepsilon_j} \tag{22}$$

$$\boldsymbol{\varepsilon_i = S_{ij}\sigma_j} \tag{23}$$

Since the elasticity tensor is symmetric there are only 21 independent elastic constants for a general elastic material (see for example [1]). The number of elastic constants reduces in case of material symmetry. In Eq. (24) the compliance tensor is shown for a material with three perpendicular planes of symmetry (orthotropic material).

$$\begin{bmatrix} \varepsilon_{11} \\ \varepsilon_{22} \\ \varepsilon_{33} \\ 2\varepsilon_{23} \\ 2\varepsilon_{31} \\ 2\varepsilon_{12} \end{bmatrix} = \begin{bmatrix} \frac{1}{E_1} & -\frac{\nu_{12}}{E_1} & -\frac{\nu_{31}}{E_3} & 0 & 0 & 0 \\ & \frac{1}{E_2} & -\frac{\nu_{23}}{E_2} & 0 & 0 & 0 \\ & & \frac{1}{E_3} & 0 & 0 & 0 \\ & & & \frac{1}{G_{23}} & 0 & 0 \\ & sym. & & & \frac{1}{G_{31}} & 0 \\ & & & & & \frac{1}{G_{12}} \end{bmatrix} \cdot \begin{bmatrix} \sigma_{11} \\ \sigma_{22} \\ \sigma_{33} \\ \sigma_{23} \\ \sigma_{31} \\ \sigma_{12} \end{bmatrix} \tag{24}$$

Here E_1, E_2 and E_3 describe the Young's moduli, G_{12}, G_{23} and G_{31} are the shear moduli and ν_{12}, ν_{23} and ν_{31} are the Poisson's ratios. Examples for orthotropic materials are wood, fabrics, fiber composite materials and rolled sheet metals. If there exist an axis of rotational symmetry, then the material is called transverse isotropic. In this case two of the Young's moduli, shear moduli and Poisson's ratios are equal. In case of an isotropic material there exists only one Young's modulus, one shear modulus and one Poisson's ratio.

If the stress exceeds a certain threshold, then the powder deforms plastically. To model yielding of powder in FEM the yield surface has to be provided in addition to the elastic properties. As soon as the stress state reaches the yield surface the powder deforms plastically. A general form of the yield surface is given in Eq. (25). A good discussion about standard requirements to yield surfaces is found in [84]. The Drucker-Prager/Cap model is a widely used form of the yield surface for powders and is shown in Figure 35 (see [51]). In the Drucker-Prager/Cap model the yield surface in stress space is divided into a shear failure surface F_s and into a cap surface F_c. In both cases the von Mises equivalent stress q is computed as a function of the hydrostatic pressure p.

$$F(\boldsymbol{\sigma}) = 0 \tag{25}$$

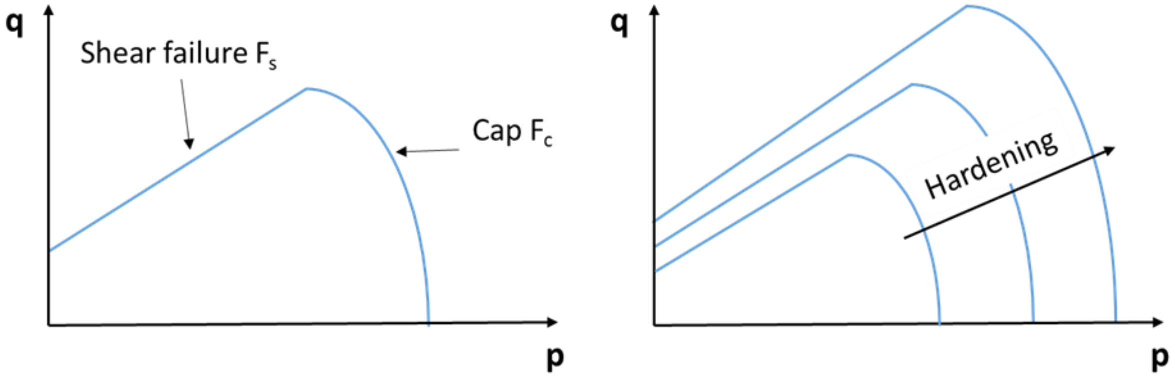

Figure 35: left: Drucker-Prager/Cap model in the hydrostatic stress-equivalent stress plane; right: Representation of material hardening during compaction of the Drucker-Prager/Cap yield surface.

A suitable yield model will need two important ingredients for our study. Firstly, as the strength of the powder changes in a compaction process, the yield surface has to grow during compaction (Figure 35 right). Such a surface growth is commonly modeled by an isotropic hardening law [84]. Hence, a huge amount of compression tests are necessary to determine the evolution of the yield surface. Secondly, the boundary conditions of compaction may render the powder compact's material properties to be anisotropic. An arbitrary initial arrangement of particles, which are made of an isotropic material, will show different material properties in the three principal directions after closed die compaction. Once again, the strength of the compact has to be tested in different loading directions to construct an anisotropic yield surface that is not known a priori.

Several yield surfaces to describe anisotropic plastic deformations were developed by Hill [85]. These yield criteria are based on the isotropic von Mises yield criterion, are widely used for metals and composites, and can be considered to be standard for FEM applications. We mention exemplarily some modifications of this approach [86–88]. An alternative criterion for plastic anisotropy was presented by Barlat [89], who introduced a criterion based on the weighted deviatoric stress tensor. Variations of this work were describes by [90–93]. A recent book [94] reviews the theory of pressure-sensitive plasticity which is important for structured materials including voids. Recent studies of powder compaction reported experimental investigations of the strength anisotropy after closed die compaction in [81] and determination of the compact’s strength by simulation in [59].

The objective of the current work is the investigation of the expected anisotropic material properties after non-isostatic compaction. The goal is to obtain reliable material properties (elastic and plastic) after compaction with different strain paths (i.e., different Dirichlet boundary conditions on a representative volume element, RVE, in compaction) and different compact densities. Therefore, we employ a multi-particle FEM (MPFEM) model already introduced by us in [95] to study the elastic and plastic properties of a representative volume element RVE consisting of deformable particles. First the model is described. Then results on the elastic properties are given, followed by results for the yield surfaces. Finally, a conclusion and outlook are provided.

4.2 Model

4.2.1 Representative Volume Element (RVE) of deformable Particles

The present work is based on a model introduced by us [95] where detailed information about the implementation is given. The model is used to obtain homogenized quantities of a particulate system. Specifically, the homogenized stress and strain inside a powder bed are determined. The stress and the strain are needed to derive the elastic and plastic properties for a continuum model of the powder. The model arranges a certain number of particles in a periodic RVE using the commercial multi-purpose finite element package Abaqus 6.14. Due to the periodic boundary conditions an RVE of 50 monodisperse spherical particles as shown in Figure 36 is sufficient to obtain representative averaged properties. To eliminate the variation between different arrangements of particles, three arrangements are simulated and averaged properties are determined. Besides, the particles in the multi-particle finite element (MPFEM) model are discretized with standard three-dimensional solid elements in Abaqus. The explicit solver is used during simulation and an appropriate mass scaling is employed to increase the time step size.

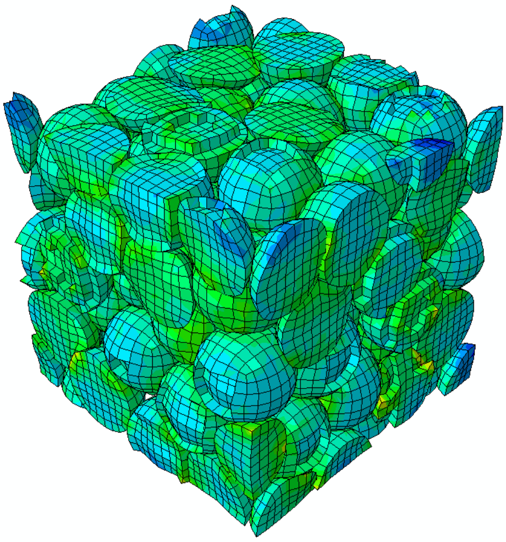

Figure 36: RVE of 50 deformable particles with periodic boundary conditions

The periodic boundary conditions are a key factor in this model. The arrangement of the particles on the boundary is periodic, i.e., for each particle on one face of the RVE there exists a particle on the opposite face. The displacements of each pair of corresponding particles is constraint via linear constraint equation. The constraint equations include the displacement of an auxiliary node. Three auxiliary nodes are used to govern the relative displacements of the particles at two opposing faces of the RVE. In addition to that, the constraint forces of all included constraints are summarized as reaction force at the auxiliary nodes. The displacements of auxiliary nodes are used to compute the strain of the RVE, and the reaction force yields the stress of the RVE. During testing of the mechanical properties of the powder the infinitesimal strain theory is used, since only small strains are considered during elastic deformation and yielding of the RVE. This means the size of the RVE is assumed to stay constant during testing. The Cauchy stress tensor is defined as

$$\boldsymbol{\sigma} = \begin{bmatrix} \frac{F_{xx}}{A_x} & \frac{F_{xy}}{A_x} & \frac{F_{xz}}{A_x} \\ \frac{F_{yx}}{A_y} & \frac{F_{yy}}{A_y} & \frac{F_{yz}}{A_y} \\ \frac{F_{zx}}{A_z} & \frac{F_{zy}}{A_z} & \frac{F_{zz}}{A_z} \end{bmatrix} \tag{26}$$

The three force vectors $\boldsymbol{F}_x, \boldsymbol{F}_y$ and $\boldsymbol{F}_z$ are taken from the three auxiliary nodes and their components are used to compute the stress tensor. The cross sections of the RVE faces are denoted as A_x, A_y and A_z. Similarly, the strain tensor

$$\boldsymbol{\varepsilon} = \begin{bmatrix} \frac{\Delta u_{xx}}{l_x} & \frac{1}{2}\left(\frac{\Delta u_{xy}}{l_x} + \frac{\Delta u_{yx}}{l_y}\right) & \frac{1}{2}\left(\frac{\Delta u_{zx}}{l_z} + \frac{\Delta u_{xz}}{l_x}\right) \\ \frac{1}{2}\left(\frac{\Delta u_{xy}}{l_x} + \frac{\Delta u_{yx}}{l_y}\right) & \frac{\Delta u_{yy}}{l_y} & \frac{1}{2}\left(\frac{\Delta u_{yz}}{l_y} + \frac{\Delta u_{zy}}{l_z}\right) \\ \frac{1}{2}\left(\frac{\Delta u_{zx}}{l_z} + \frac{\Delta u_{xz}}{l_x}\right) & \frac{1}{2}\left(\frac{\Delta u_{yz}}{l_y} + \frac{\Delta u_{zy}}{l_z}\right) & \frac{\Delta u_{zz}}{l_z} \end{bmatrix} \tag{27}$$

can be computed based on components of the displacement vectors of the auxiliary nodes $\Delta\boldsymbol{u}_x$, $\Delta\boldsymbol{u}_y$ and $\Delta\boldsymbol{u}_z$. The dimensions of the RVE are denoted as l_x, l_y and l_z.

Each particle in the RVE is modeled as an elasto-plastic body which does not break during deformation. In reality this is the case for most metallic materials. In this work the material properties of copper are used. The yield stress is defined as a piecewise linear function of the plastic strain based on the experimental data in [78] and [79]. All material properties are summarized in Table 10. If brittle materials would be considered, such as ceramics or some excipients in pharmaceutical industry, it would be necessary to use an appropriate fracture criterion to model cracking of the particles. In this case, the MPFEM model is more complex as new surfaces are created during compaction and additional material properties need to be considered.

Table 10: Material properties of copper

Property	Value
Young's modulus	115 GPa
Poisson ratio	0.34
density	8920 kg/m^3
σ/ MPa	**$\varepsilon_{plastic}$**
150	0.00
250	0.06
300	0.30
350	1.00
400	2.50
450	5.00

The contact properties between particles are of importance, since failure of powders often occurs at contacts between particles. To compute the contact stress a simple contact model including cohesion stresses was implemented as VUINTERACTION subroutine in Abaqus. The contact normal stress is computed as a function of the normal distance δ_N and the normal relative velocity $\dot{\delta_N}$ of the slave node to the master surface (see Table 11). The distance has positive values for penetrations and negative values for gaps. Similarly, the contact tangential stress is computed as a function of the relative tangential displacement δ_T and the tangential relative velocity $\dot{\delta_T}$. Three different cases are distinguished (see Table 11).

The total normal stress is a function of the repulsive stress σ_{rep}, the contact cohesion stress σ_{coh} and an additional damping stress. The signs follow from the convention where pressure stress is counted as positive. The damping stress is a linear function of the relative normal speed and a damping coefficient d. The damping coefficient is chosen to damp contact oscillations and to simultaneously avoid substantial additional macroscopic stresses. Similar to the normal stress the total tangential stress is a function of the friction force and a low tangential damping stress.

Table 11: Contact model

	Normal direction	Tangential direction
$\boldsymbol{\delta_N < \delta_0}$	$\sigma_N = 0$	$\sigma_T = 0$
$\boldsymbol{\delta_0 < \delta_N < 0}$	$\sigma_{rep} = 0$ $\sigma_{coh} = c_{max}\left(1 - \frac{\delta_N}{\delta_0}\right)$	$\sigma_{fric} = 0$
$\boldsymbol{0 < \delta_N}$	$\sigma_{rep} = k \cdot \delta_N$ $\sigma_{coh} = c_{max}$	$\lvert k \cdot \delta_T \rvert < \sigma_{rep} \cdot \mu$: $\sigma_{fric} = -k \cdot \delta_T$ $\lvert k \cdot \delta_T \rvert > \sigma_{rep} \cdot \mu$: $\sigma_{fric} = -\sigma_{rep} \cdot \mu \cdot \frac{\delta_T}{\lvert \delta_T \rvert}$
total	$\sigma_N = \sigma_{rep} - \sigma_{coh} + d \cdot \dot{\delta_N}$	$\sigma_T = \sigma_{fric} - 0.01 \cdot d \cdot \dot{\delta_T}$

The contact parameters used in the simulations are summarized in Table 12. Two different values of the contact stiffness are used for testing the yield properties and the elastic properties. A comparably high contact stiffness is used during testing the elastic properties to avoid artificial softening due to too soft contacts. A lower contact stiffness is used during testing the yield properties, since it has no essential influence on the yield strength, but a larger simulation time step can be used to speed up the simulations. The maximum cohesion strength c_{max} is varied in the range from 1 to 1000 MPa. The lower values describe the weak bonding of particles after cold compaction while the high values exceed the yield strength of the particle material and are therefore useful to describe strong bonding of particles after sintering. The cohesion interaction length is given as a fraction of the particle diameter. The latter is chosen for simplicity to be 1 m.

Table 12: Contact properties

Property	Value
Contact stiffness k (yield tests)	$1.0\cdot10^{12}$ N/m
Contact stiffness k (elasticity tests)	$1.0\cdot10^{14}$ N/m
Coefficient of friction μ	0.2
Maximum cohesion strength c_{max}	[1, 10, 100, 300, 600, 1000] MPa
Cohesion interaction length δ_0	$0.01\cdot d_{Particle}$
Damping coefficient d	500 MPa·s/m

4.2.2 Compaction Simulation

The MPFEM simulation procedure is divided in three steps. In Figure 37 the evolution of the stress inside the powder is shown for simplicity in the 2D stress space although the real simulation is in 3D. In the first step the initial packing is compacted with strain- (deformation-) controlled tri-axial compression. After compaction a short dwell step is used to allow for dissipation of possible particle oscillations. Then, the load control of the RVE is shifted to stress (force) control and the load is ramped down thoroughly to obtain a stress-free RVE. Starting from this configuration the RVE is reloaded in different directions during the testing step to determine the mechanical properties of the compacted powder.

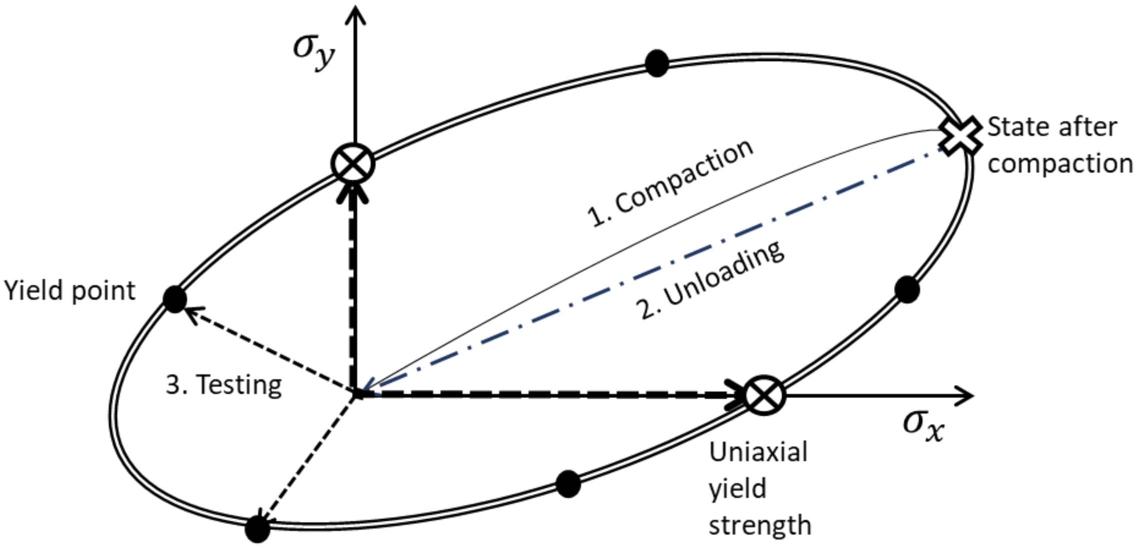

Figure 37: Schematic evolution of the stress during three steps of the compaction simulation and subsequent testing. The real simulation is in 3D.

We introduce seven different strain paths for the compaction step (see Figure 38). The initially cubic RVE is strained along the x-, y- and z-direction, i.e., the three different strains in direction of the coordinate system are equal to the principal strains during compaction as no shear strains develop. The strain is computed based on the engineering strain measure as shown in Eq. (28). The vector of the principal strains during compaction can therefore be written as shown in Eq. (29). Furthermore, the mean strain $\bar{e}$ is computed in a standard fashion from the dilatation (relative variation of the volume) as given in Eq. (30). The values of the principal strains for the seven different strain paths are given as a fraction of the mean strain. In this way the ratios of the three principal strains are fixed for a certain strain path irrespective of how dense the powder is compacted. In strain path case A (see Figure 38) all three strains are equal, and therefore, this case describes isostatic compaction. Isostatic compaction is relevant in powder metallurgy during hot isostatic pressing of high quality products. In case B the powder is only compressed in x-direction and no strain is allowed perpendicular to the x-direction. This case refers to closed die compaction and is the most often used strain path during compaction of powders. It is widely used during tableting in the pharmaceutical industry and during production of green bodies before sintering. In real compaction processes ideal homogenous deformation of the powder does not occur due to the friction between tools and powder, which affect the distribution of the strain inside the powder (e.g., see [96]). Therefore, the strain path is also not constant across the powder compact. We consider strain path case C to case G to account for a possible inhomogeneous deformation during compaction. Case C works similar to case B but in this case the powder is stretched perpendicular to the x-direction. In cases D and E, the powder is compacted in y- and z-direction. While in case D no straining takes place in x-direction, in case E a stretch is applied. Finally, three different strains are applied in cases F and G. The absolute values for the strains are determined based on the initial packing density and the final packing density after compaction. The final packing density was varied in the range from 0.65 to 0.95. For all cases the powder was unloaded after compaction to obtain the stress free reference state which is tested in the last step. The dimension of the unloaded RVE is used to calculate the stresses and strains needed during the testing step.

$$e_i = -\frac{\Delta l_i}{L_0} \tag{28}$$

$$\boldsymbol{e} = \begin{bmatrix} e_1 \\ e_2 \\ e_3 \end{bmatrix} \tag{29}$$

$$\bar{e} = \frac{e_1 + e_2 + e_3}{3} \tag{30}$$

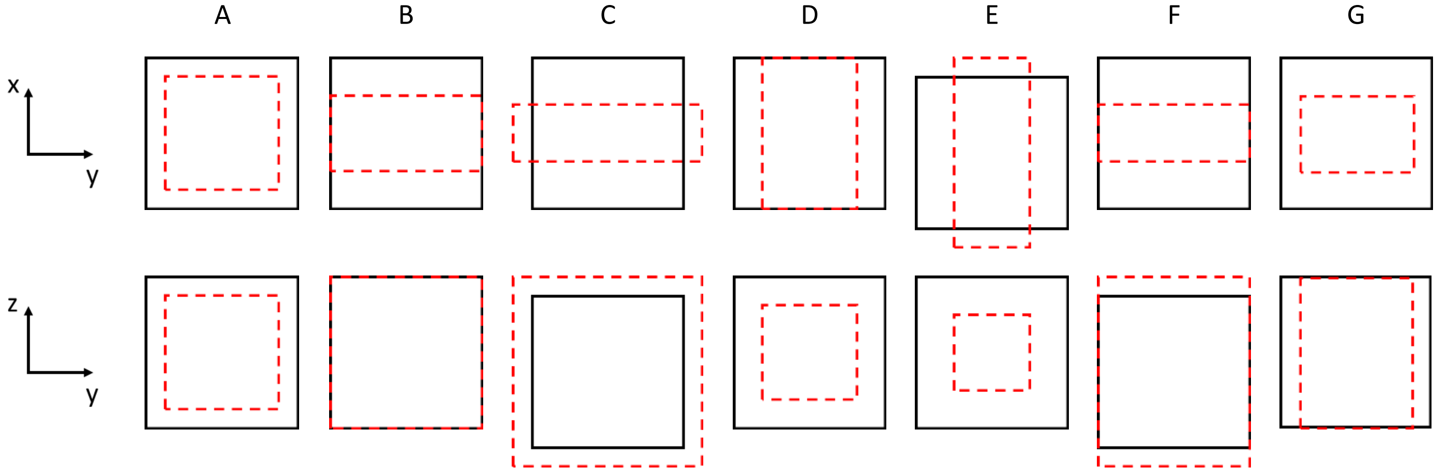

A: $e_1 = \bar{e}$, $e_2 = \bar{e}$, $e_3 = \bar{e}$

B: $e_1 = 3\bar{e}$, $e_2 = 0$, $e_3 = 0$

C: $e_1 = 5\bar{e}$, $e_2 = -\bar{e}$, $e_3 = -\bar{e}$

D: $e_1 = 0$, $e_2 = 3/2\bar{e}$, $e_3 = 3/2\bar{e}$

E: $e_1 = -6/8\bar{e}$, $e_2 = 15/8\bar{e}$, $e_3 = 15/8\bar{e}$

F: $e_1 = 6\bar{e}$, $e_2 = 0$, $e_3 = -3\bar{e}$

G: $e_1 = 2\bar{e}$, $e_2 = \bar{e}$, $e_3 = 0$

Figure 38: The seven different strain paths during compaction. The continuous line indicates the state before compaction and the dashed line the state after compaction.

4.2.3 *Testing of the Elastic Properties*

The elastic properties of the compacted powder are tested with our model. For that the reference state of the RVE is externally loaded for each of the six stress components in Eq. (24). The normal stresses are investigated for positive and negative signs to take the difference of tension and compression into account. The stress inside the RVE is calculated based on Eq. (26), while Eq. (27) is used to determine the corresponding strain. We plot exemplarily the stress as a function of the strain for uniaxial compression and tension in the direction of the first principal axis in Figure 39. Since all stress components, except of the loading direction, are zero it is possible to make use of Eq. (24) to obtain the elastic constant relevant for this type of loading. In this way, all components of the orthotropic elasticity model given in Eq. (24) can be obtained. Table 13 presents the evaluation of the nine independent elastic constants based on the six different loading cases. As shown, each Poisson’s ratio can be computed based on two different loading cases. Both cases are used in our subsequent analysis and the average value of the Poisson’s ratio is reported. The stress-strain curves of the compacted powders are generally no straight lines. Especially in case of low contact cohesion they are non-linear, as can be seen in Figure 39. This means the elastic constants are strictly speaking no constants, but are a function of the stress. In this work we aim for a description of the powder as a linear elastic material. Hence, the elastic constants are found by linearization of the stress-strain curve for strains smaller than a defined threshold strain which is chosen here to be 0.002.

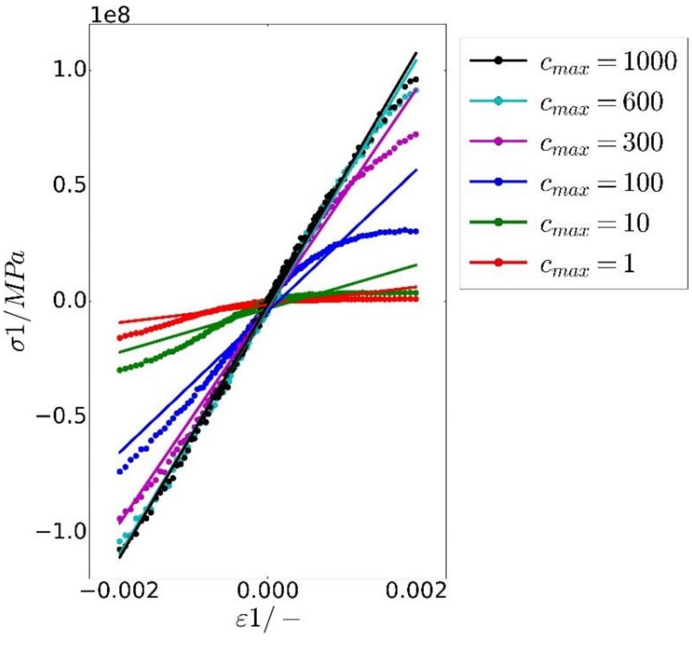

Figure 39: Determination of the Young's modulus E1 based on linear regression of the stress-strain curve for small strains. Different cohesion strengths of the particle contacts are considered as shown in the legend. Straight lines are a fit of the strain-stress relationship.

Table 13: Evaluation of the elastic constants for different loading directions

Loading	**Elastic Modulus**	**Poisson's ratio**
$\pm\boldsymbol{\sigma}_{11}$	$E_1 = \frac{\sigma_{11}}{\varepsilon_{11}}$	$\nu_{12} = -\frac{\varepsilon_{22}}{\varepsilon_{11}};\ \nu_{31} = -\frac{\varepsilon_{33}}{\varepsilon_{11}}\frac{E_3}{E_1}$
$\pm\boldsymbol{\sigma}_{22}$	$E_2 = \frac{\sigma_{22}}{\varepsilon_{22}}$	$\nu_{23} = -\frac{\varepsilon_{33}}{\varepsilon_{22}};\ \nu_{12} = -\frac{\varepsilon_{11}}{\varepsilon_{22}}\frac{E_1}{E_2}$
$\pm\boldsymbol{\sigma}_{33}$	$E_3 = \frac{\sigma_{33}}{\varepsilon_{33}}$	$\nu_{31} = -\frac{\varepsilon_{11}}{\varepsilon_{33}};\ \nu_{23} = -\frac{\varepsilon_{22}}{\varepsilon_{33}}\frac{E_2}{E_3}$
$\boldsymbol{\sigma}_{23}$	$G_{23} = \frac{\sigma_{23}}{2\varepsilon_{23}}$	
$\boldsymbol{\sigma}_{31}$	$G_{31} = \frac{\sigma_{31}}{2\varepsilon_{31}}$	
$\boldsymbol{\sigma}_{12}$	$G_{12} = \frac{\sigma_{12}}{2\varepsilon_{12}}$	

4.2.4 Testing of the Yield Properties

The uniaxial yield strength of an RVE of the compacted powder is tested by applying uniaxial loading starting from the reference state. During loading the stress and the strain inside the powder are evaluated based on Eq. (26) and (27), respectively. Yielding is defined based on a scalar plastic strain measure already proposed in [95] to describe the onset of yielding for general loading cases (see Eq. (31)).

$$\varepsilon_{pl} = \sqrt{\frac{2}{3}\boldsymbol{\varepsilon} : \boldsymbol{\varepsilon}} - \sqrt{\frac{2}{3}\boldsymbol{\varepsilon}_{el} : \boldsymbol{\varepsilon}_{el}}. \tag{31}$$

Therefore, the yield point is found by evaluating the equivalent plastic strain ε_{pl} of Eq. (31) after probing the RVE in a certain direction. The strain tensor $\boldsymbol{\varepsilon}$ is computed with Eq. (27) based on the displacements of the auxiliary nodes during testing. The elastic strain $\boldsymbol{\varepsilon}_{el}$ at the yield point is found during unloading. To avoid cyclic loading and unloading for every single yield point, we define the unloading strain after compaction as the elastic strain for all loading directions. The yield point for a certain load case is reached if the plastic equivalent strain exceeds a defined threshold. Below this threshold of the plastic equivalent strain, the deformation is assumed to be elastic. The threshold for the plastic equivalent strain is chosen to be 0.002 in analogy to the offset yield point in uniaxial tensile testing, where a plastic strain of 0.2% is used to define the yield strength. The corresponding yield stress tensor of this loading direction is evaluated according to Eq. (26) in a post-processing step.

During determination of the yield surface of the compacted powder a total of 82 yield points are tested. We aim for an even distribution of these points on the yield surface in stress space. To find a proper distribution of the yield points the rough dimensions of the yield surface is estimated during 4 trial tests. In the 4 trial tests the yield point for the loading direction during compaction, the yield point for isostatic compression and their inverted loading directions are tested. The remaining 78 yield points are evenly distributed based on the 4 obtained yield points. During testing the 78 yield points, the powder is first loaded to obtain a stress state in the center of the yield surface. Starting from this stress state an additional load is applied into different directions to hit the yield surface.

4.3 Results - Elastic Properties

The elastic properties of the powder compacted in different strain paths are summarized in Figure 40. The plots show the Young's modulus E, the shear modulus G and the Poisson's ratio ν as a function of the maximum contact cohesion c_{max} and the relative density ρ_{rel} of the powder after compaction. The simulation series of contact cohesion was conducted for a constant relative density of 0.85 while the contact cohesion was set to 100 MPa during the series of the relative densities. The points in the plots describe the average elastic properties of three different packings of 50 particles. The lines indicate the regression curves, also given in Eq. (32) to (34), which describe the simulated properties as a function of the relative density, the maximum contact cohesion and the main principal strains during compaction.

Case A

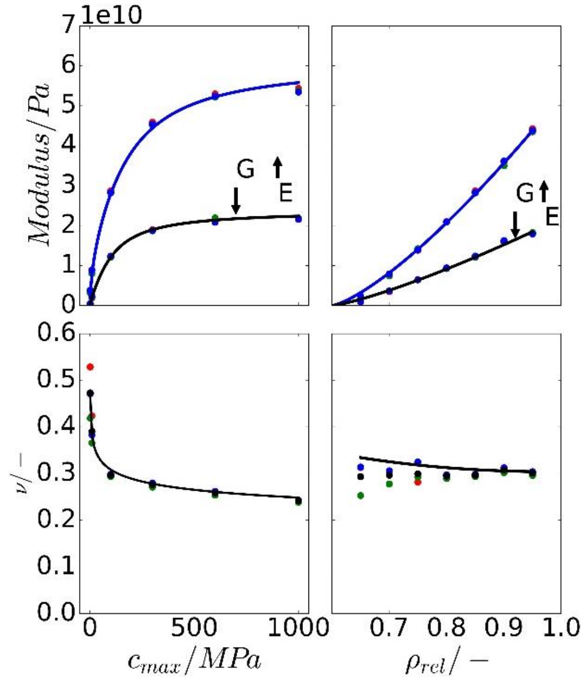

Case B

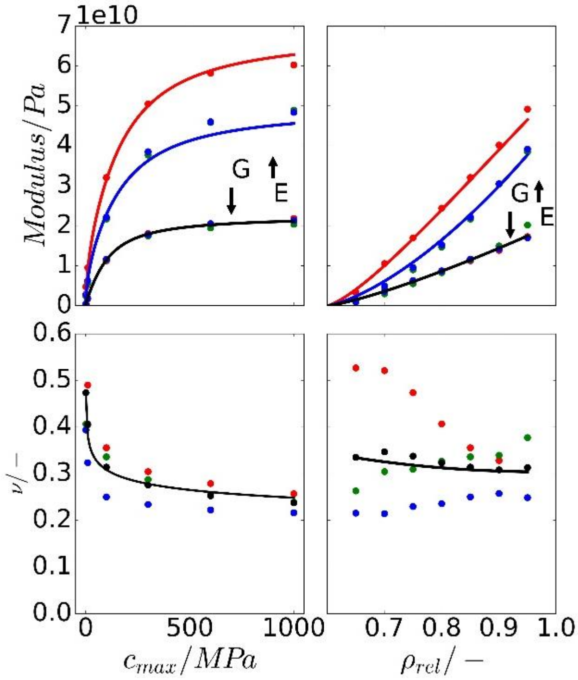

Case C

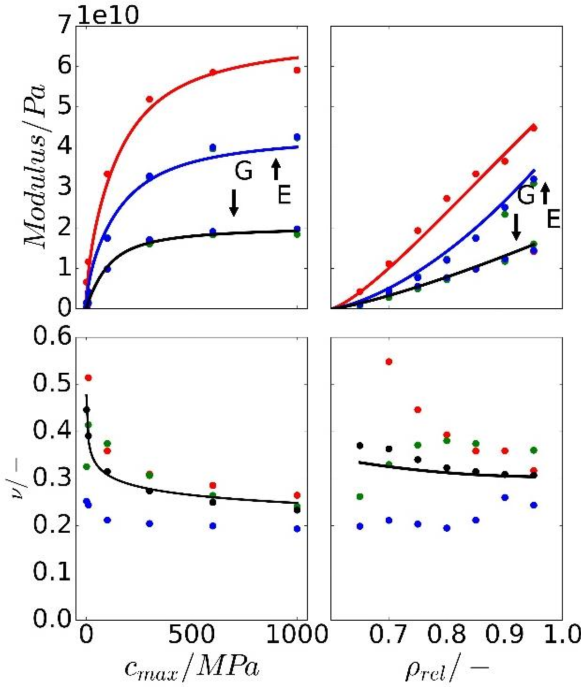

Case D

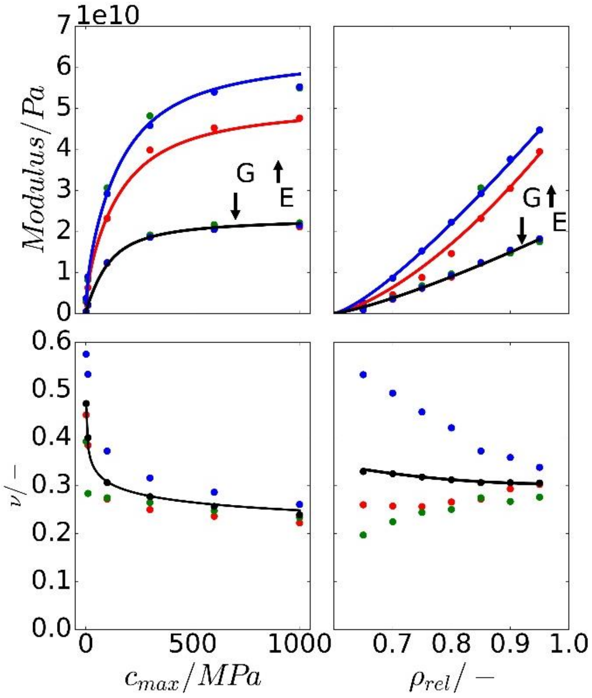

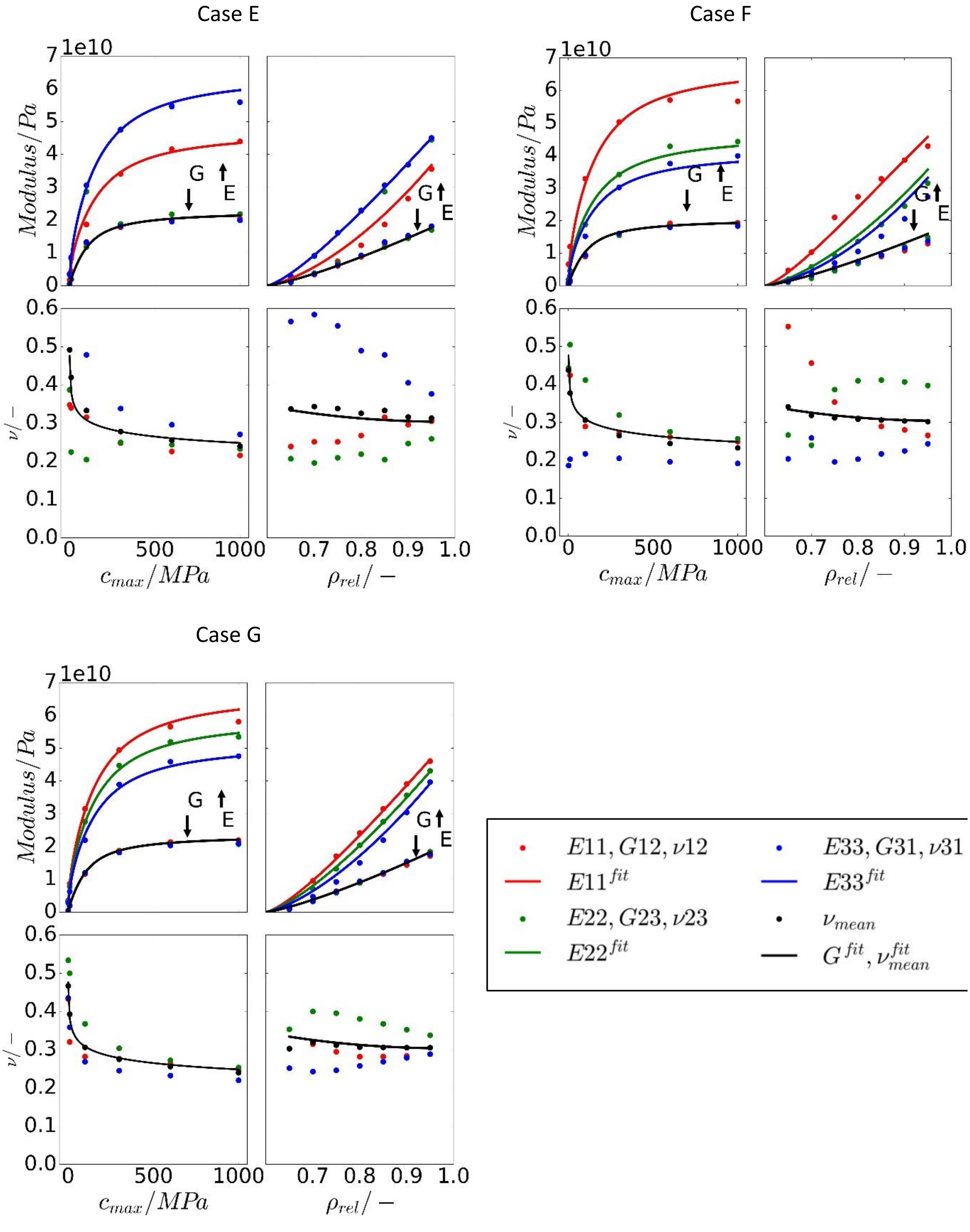

Figure 40: Elastic properties for 7 different compaction cases. The points are the simulation results and the curves are a regression fit of the simulated points. The results for contact cohesion (left panels) were obtained for a constant relative density of 0.85. Results for density (right panels) were obtained for a contact cohesion of 100 MPa.

The regression equation of the Young's modulus E_i for a certain loading direction as shown in Eq. (32) can be divided into two parts. The first part describes the increase of the Young's modulus as a function of the relative density and the contact cohesion. The influence of the contact cohesion is described by means of the arc tangent since the observed saturation behavior can be modelled in this manner. The second part of the equation includes the influence of the strain path during compaction and is only important for non-isostatic compaction. The Young's modulus averaged over the three principal axes is a maximum for isostatic compaction and decreases as a function of the standard deviation of the three principal strains in case of non-isostatic compaction. The Young's modulus is furthermore higher for directions of high compaction strains and lower for directions of low or even negative strains as described by the arc tangent. In case of the important application of closed-die compaction (case B), the Young's modulus is higher in the direction of the punch axis than perpendicular to the punch axis. This may be crucial during unloading of the powder compact inside the die after compaction, since usually first the upper punch is removed before the powder compact is ejected. This step-wise elastic unloading leads to stress states which may cause failures like the well-known capping of tablets after compaction.

The shear modulus is described in Eq. (33) as a function of the relative density, the contact cohesion and the principal strains during compaction. The shear modulus increases with increasing relative density and contact cohesion and decreases with increasing standard deviation of the strain components during compaction. In contrast to the Young's modulus there is no big influence of the loading direction irrespective of the strain path during compaction. The shear modulus can therefore be considered to be isotropic in the studied strain paths which are chosen to be practically important for compaction processes.

The regression of the Poisson's ratios for different loading directions proved to be difficult. It was not possible to obtain a unified equation which described all strain paths during compaction. Hence, we reduce ourselves to describe the averaged Poisson's ratio based on Eq. (34). The averaged Poisson's ratio is approximately 0.3 for a large range of the relative density and the contact cohesion. Only in case of very weak contact cohesion the Poisson's ratio increases up to 0.5. In this case the powder has only low strength and therefore the deformation during testing is plastic rather than elastic. According to basic plasticity theory of metals a Poisson's ratio of 0.5 is expected during plastic yielding, if plastic incompressibility is assumed [97]. The difference of the Poisson's ratios for different directions is especially distinct for low relative density and low contact cohesion. There seem to be preferred directions for transverse strain which are correlated to the principal strains during compaction as similar evolutions are observed for similar strain paths, e.g., similar evolutions of the different Poisson's ratios are found for strain path case B and case C since in both cases the powder is only compacted in x-direction. However, there is no unified rule how to describe the Poisson's ratio based on the principal strains for all different strain paths during compaction.

$$\begin{aligned} E_i = {} & 3.04 \cdot 10^{11} \cdot (\rho_{rel} - 0.6)^{1.34} \cdot \operatorname{atan}\left(\frac{c_{max}}{246}\right)^{0.559} \cdot \\ & \cdot \left[1 - 0.04 \cdot std\left(\frac{\boldsymbol{e}}{\bar{e}}\right)^{0.899} + 0.571 \cdot (1.14 - \rho_{rel}) \cdot \operatorname{atan}\left(\frac{e_i}{\bar{e}} - 1\right)\right] \end{aligned} \tag{32}$$

$$G_{ij} = 9.34 \cdot 10^{10} \cdot (\rho_{rel} - 0.6)^{1.26} \cdot atan\left(\frac{c_{max}}{118}\right)^{0.846} \cdot \left(1 - 0.0343 \cdot std\left(\frac{\boldsymbol{e}}{\bar{e}}\right)^{1.35}\right) \tag{33}$$

$$\nu_{mean} = 0.305 \cdot (1 - \rho_{rel})^{2.19} + atan\left(\frac{0.00038}{c_{max}}\right)^{0.1} \tag{34}$$

4.4 Results - Yield Properties

4.4.1 Uniaxial Strength

The evolution of the uniaxial yield strength as a function of the relative density and the cohesion strength is shown in Figure 41 for different strain paths during compaction. The tensile strength is plotted in positive direction of the ordinate while the compression strength is negative. For each strain path two simulation series are performed. The left diagrams show the uniaxial strengths as a function of the cohesion strength for a constant relative density of 0.85 after compaction while the right diagrams show the uniaxial strengths as a function of the relative density for a cohesion strength of 100 MPa. The full lines indicate the regression curves shown in Eq. (35) and (36).

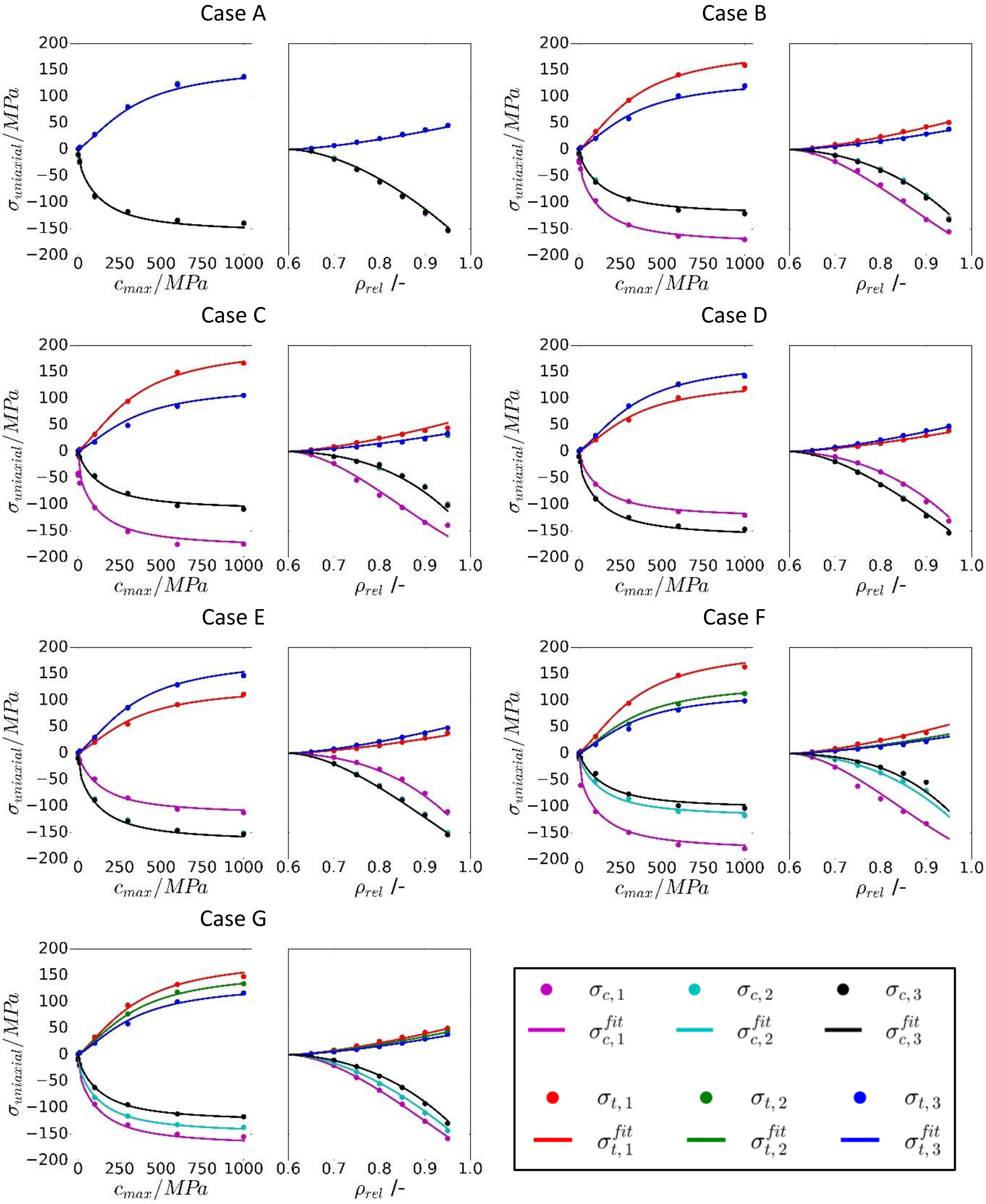

Figure 41: Uniaxial strength as a function of relative density and cohesion strength. Left panels show dependence on cohesion strength for constant relative density of 0.85. Right panels show dependence on relative density for cohesion strength of 100 MPa.

Eq. (35) shows the regression of the tensile strength for a direction of principal strain during compaction as a function of the relative density, the cohesion strength and the compaction strain in the direction under consideration. The tensile strength increases as a function of the relative density and the contact cohesion. As it was seen for the Young's modulus also the tensile strength is highest for the direction of the highest compaction strain. Hence, if isotropic mechanical properties are important then it is necessary to use isostatic compaction.

The regression of the compression strength in Eq. (36) is complex. The first part of the equation describes the averaged compression strength which increases as a function of the relative density and the contact cohesion and decreases as a function of the standard deviation of the principal strains during compaction. The second part describes the anisotropic behavior. In general, the compression strength is higher for the directions of high compaction strains. The difference between different directions increases for low relative density and decreases for high relative densities. This can be explained by contact surfaces between particles which are first formed normal to the main compaction direction. In case of high relative densities of the compacted powder the contact surfaces are also formed parallel to the compaction direction and the anisotropy of the compression strength diminishes. The evolution for both uniaxial strengths as a function of the contact cohesion increase strongly for low cohesion strengths and saturate for high cohesion strengths. The denominator of the arc tangent indicates the onset of saturation and is therefore referred to as the saturation cohesion strength. The saturation cohesion strength describes the transition between contact failure of the particle contacts in case of low cohesion strength and plastic flow of the particle material in case of high cohesion strengths. The saturation cohesion strength is remarkably higher for tensile load compared to compression load. This behavior can be attributed to the different failure mechanisms for the particle material and the contacts between particles. The particle material follows a von Mises yield criterion which is independent from the loading direction while the contact failure is different for tension and compression. During tension loading the contacts are pulled apart facilitating contact failure while contacts are pressed together during compression load impeding contact failure. This leads to a transition from contact failure to particle material flow which takes place at a lower contact cohesion strength in case of compression than in case of tension.

$$\sigma_{ti} = 772 \cdot (\rho_{rel} - 0.6)^{1.44} \cdot atan\left(\frac{c_{max}}{332}\right)^{1.13} \cdot \left(1 + 0.195 \cdot atan\left(\frac{e_i}{\bar{e}} - 1\right)\right) \tag{35}$$

$$\begin{aligned} \sigma_{ci} &= -1403 \cdot (\rho_{rel} - 0.6)^{1.73} \cdot atan\left(\frac{c_{max}}{223}\right)^{0.502} \cdot \left(1 - 0.0647 \cdot std\left(\frac{\boldsymbol{e}}{\bar{e}}\right)^{0.33}\right) \\ &-2157 \cdot (\rho_{rel} - 0.6)^{1.73} \cdot (1.03 - \rho_{rel}) \cdot atan\left(\frac{e_i}{\bar{e}} - 1\right) \cdot atan\left(\frac{c_{max}}{223}\right)^{0.216} \end{aligned} \tag{36}$$

4.4.2 Yield Surface

The simulation results for the yield points in the 3D stress space are shown in Figure 42 and Figure 43. Figure 42 shows the yield points after compaction to different relative densities and a constant cohesion strength of 100 MPa for different strain paths. In Figure 43 the relative density is kept constant at 0.85 while different cohesion strengths are used. The plots show 2D projections parallel to the Cartesian coordinate axes. The coordinate axes show pressure stresses as positive, as common for yield surfaces of powders (e.g., see Figure 35). For each projection only the yield points included in the convex hull are shown for clarity. The solid lines indicate the regression curves for the yield points, and therefore, define the yield surface.

Case A, $\boldsymbol{e} = [1, 1, 1]\bar{e}$

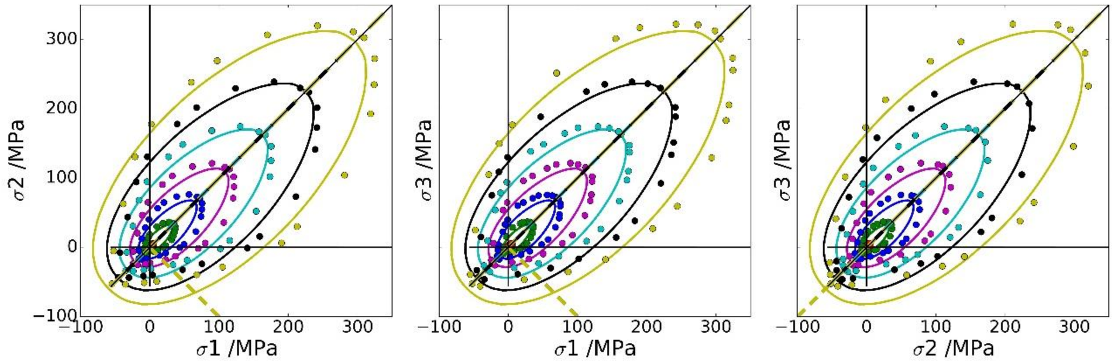

Case B, $\boldsymbol{e} = [3, 0, 0]\bar{e}$

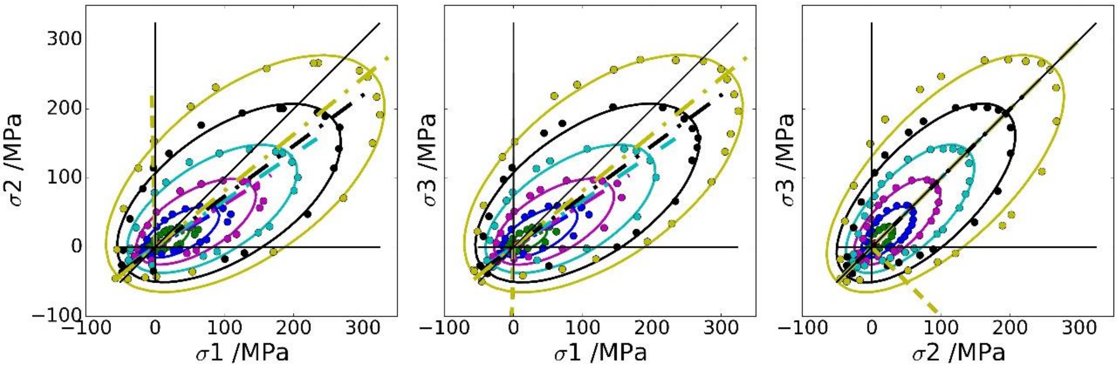

Case C, $\boldsymbol{e} = [5, -1, -1]\bar{e}$

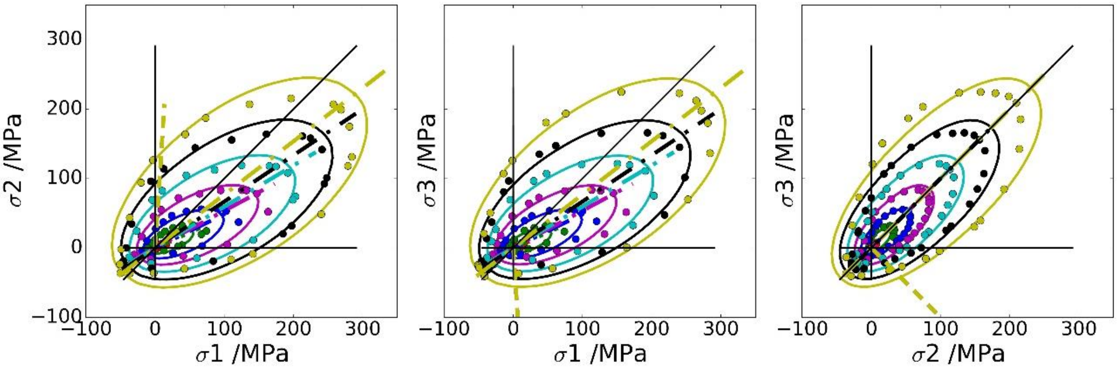

Case D, $\boldsymbol{e} = [0, 1.5, 1.5]\bar{e}$

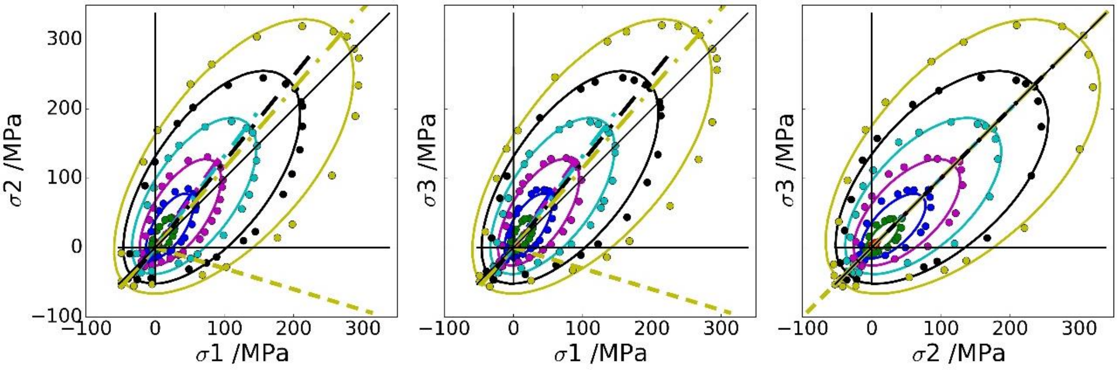

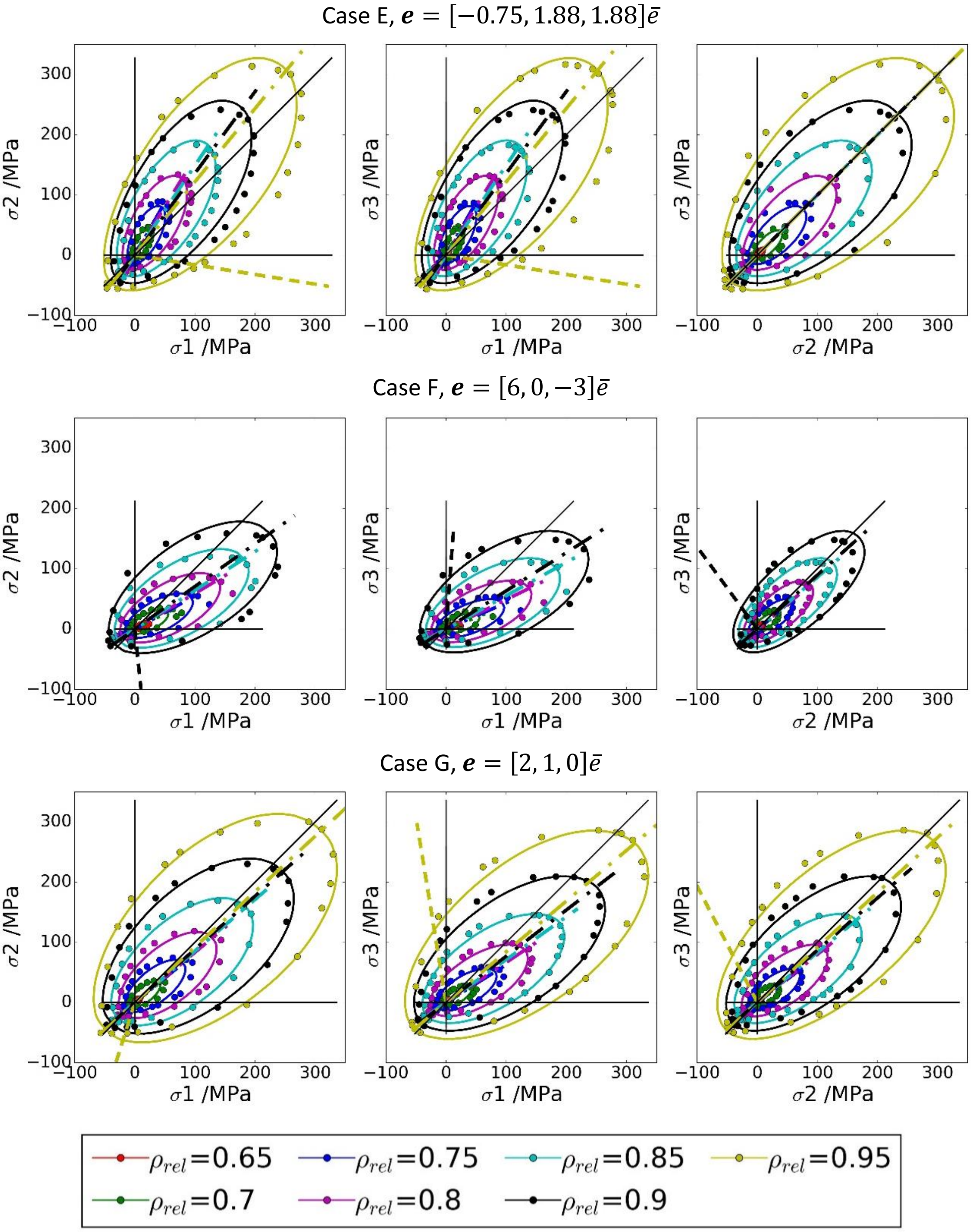

Figure 42: 2D representation of the yield points in the stress space as a function of the relative density after compaction for a constant cohesion strength of 100 MPa. The dot-dashed line indicates the rotation axis of the yield surface, while the dashed line points towards the flattest side of the yield surface ($\boldsymbol{\varphi} = \mathbf{0}$).

Case A, $\boldsymbol{e} = [1, 1, 1]\bar{e}$

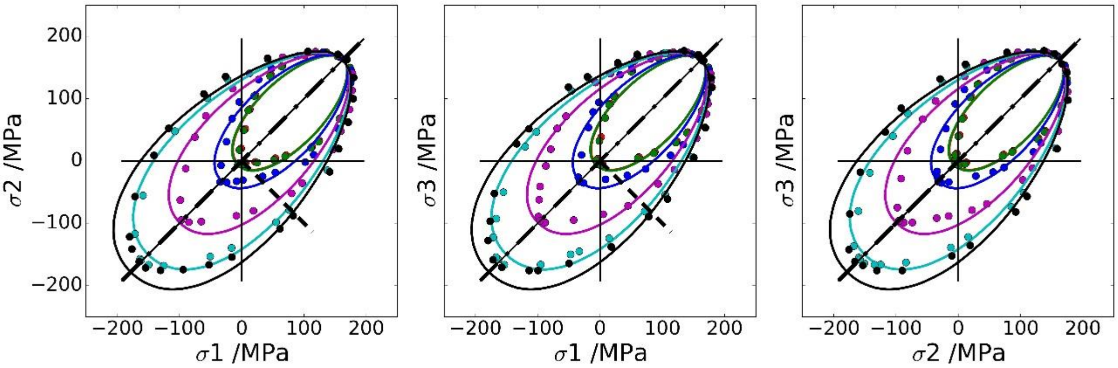

Case B, $\boldsymbol{e} = [3, 0, 0]\bar{e}$

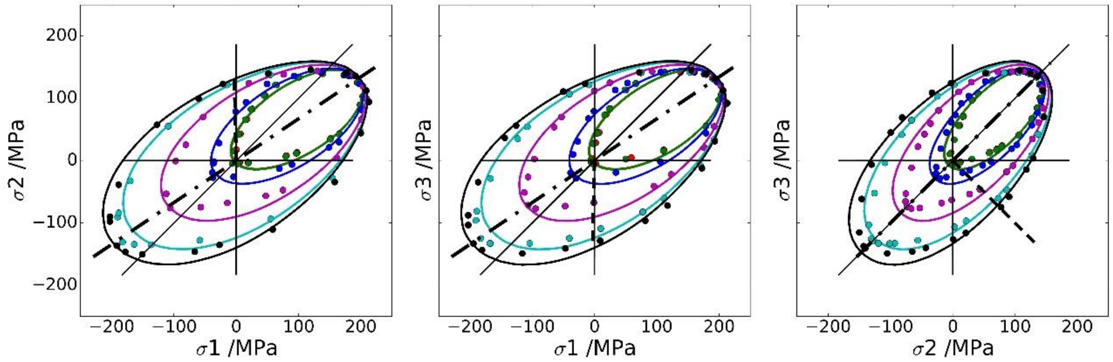

Case C, $\boldsymbol{e} = [5, -1, -1]\bar{e}$

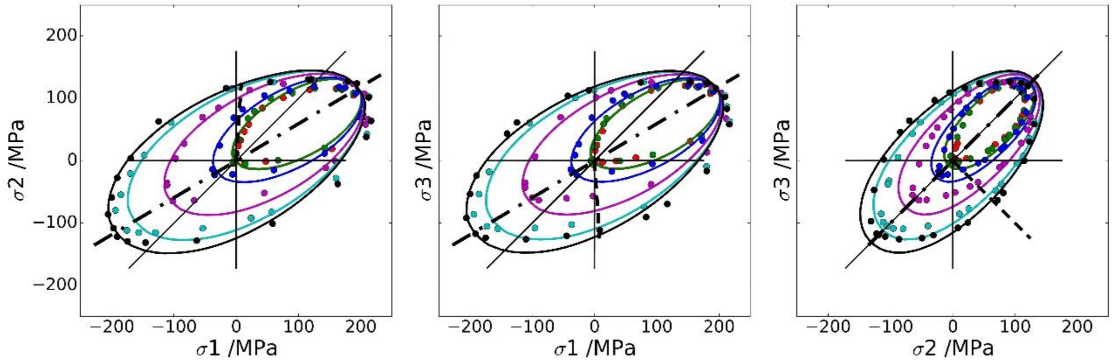

Case D, $\boldsymbol{e} = [0, 1.5, 1.5]\bar{e}$

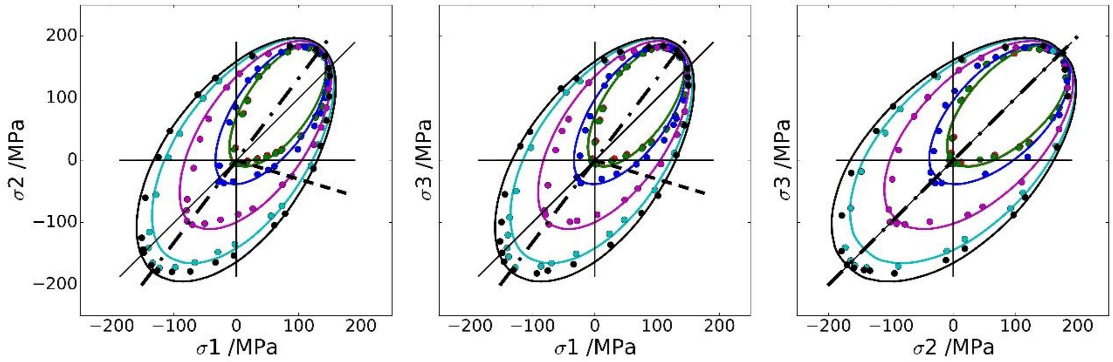

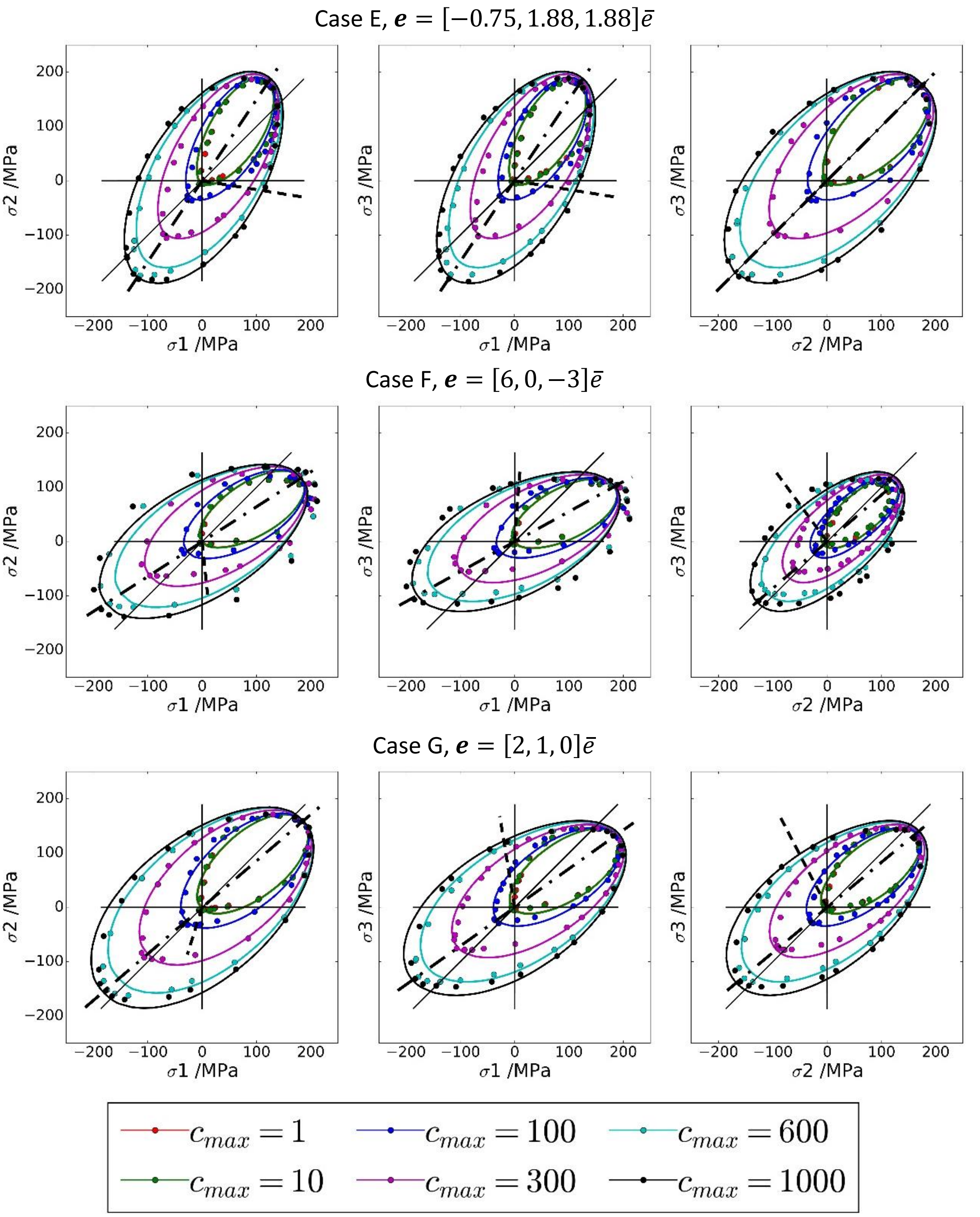
Case E, $\boldsymbol{e} = [-0.75, 1.88, 1.88]\bar{e}$

Case F, $\boldsymbol{e} = [6, 0, -3]\bar{e}$

Case G, $\boldsymbol{e} = [2, 1, 0]\bar{e}$

Figure 43: 2D representation of the yield points in the stress space as a function of the contact cohesion strength for a constant relative density of 0.85. The dot-dashed line indicates the rotation axis of the yield surface while the dashed line points towards the flattest side of the yield surface ($\varphi = 0$).

The mathematical description of the yield surface is performed in cylindrical coordinates: r, φ and z (see Figure 44 and Eq. (37)). The origin of the cylindrical coordinate system coincides with the origin of the Cartesian coordinate system. The components z_i of the unit vector pointing in the z-direction of the cylindrical coordinates are given in Eq. (38), while the axis for $\varphi = 0$ is given in Eq. (39). Eq. (37) determines the radius for each pair of φ and z as a product of three terms. The first two terms describe a 2D cut of the yield surface in the r-z plane which has the shape of an ellipse (first term) modified by a linear equation (second term). The 3D yield surface is obtained by rotating the described shape around the z-axis resulting in an ellipsoid. During rotation the surface is stretched by a factor $(l \cdot \sin(\varphi)^2 + 1)$ with l being a positive number, meaning the yield surface is flattest for $\varphi = 0, \pi$ and thickest for $\varphi = \frac{\pi}{2}, \frac{3\pi}{2}$.

The orientation of the rotation axis of the yield surface is influenced by the compaction conditions (see Eq. (38)). It is aligned with the $[1\ 1\ 1]^T$-space diagonal of the Cartesian coordinate system in case of isostatic compaction and rotated towards the direction of high compaction strain in case of non-isostatic compaction. The orientation of the rotation axis is therefore a measure of the anisotropy of the yield surface. As can be seen, the anisotropy diminishes for increasing relative density. This can, as already stated earlier, be attributed to the formation of contact surfaces which are first formed normal to the main compaction direction and formed parallel to the compaction direction in case of high relative densities. The orientation of the yield surface is not dependent on the contact cohesion according to Eq. (38) and Figure 43.

The orientation of the coordinate axis for $\varphi = 0$ is only influenced by the principal strains during compaction (see Eq. (39) and Figure 43). It always points towards the direction of minimum strain since the yield surface is flattest in this direction.

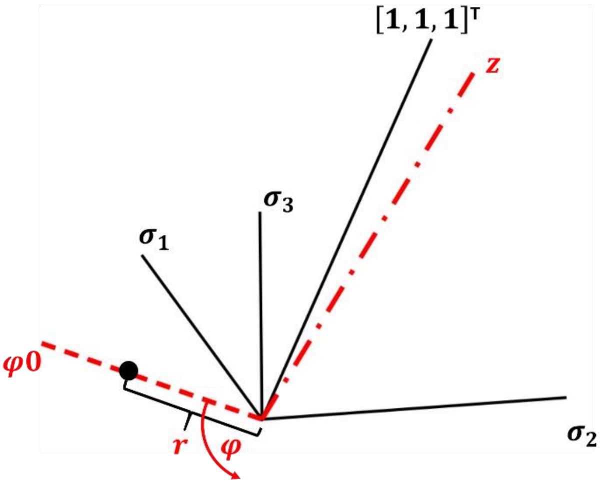

Figure 44: Cylindrical coordinate system of the yield surface

$$r(\varphi, z) = \frac{\sqrt{(a^2 - (z - z_m)^2)}}{q} \cdot (k \cdot (z - z_{max}) + 1) \cdot (l \cdot \sin(\varphi)^2 + 1) \tag{37}$$

$$z_i = \frac{\left(\frac{1}{\sqrt{3}} + 0.397 \cdot atan\left(\frac{e_i}{\bar{e}} - 1\right) \cdot (1 - \rho_{rel})^{0.615}\right)}{\sqrt{\sum_{i=1}^{3} \left(\frac{1}{\sqrt{3}} + 0.397 \cdot atan\left(\frac{e_i}{\bar{e}} - 1\right) \cdot (1 - \rho_{rel})^{0.615}\right)^2}} \tag{38}$$

$$\varphi 0_i = \begin{cases} \dfrac{+\left(1.21 - 1.02 \cdot atan\left(\frac{e_i}{\bar{e}} - 0.753\right)\right)}{\sqrt{\sum_{i=1}^{3} \left(1.21 - 1.02 \cdot atan\left(\frac{e_i}{\bar{e}} - 0.753\right)\right)^2}}, & e_i = \min(\boldsymbol{e}) \\ \dfrac{-\left(1.21 - 1.02 \cdot atan\left(\frac{e_i}{\bar{e}} - 0.753\right)\right)}{\sqrt{\sum_{i=1}^{3} \left(1.21 - 1.02 \cdot atan\left(\frac{e_i}{\bar{e}} - 0.753\right)\right)^2}}, & e_i \neq \min(\boldsymbol{e}) \end{cases} \tag{39}$$

The constants in Eq. (37) are elaborate functions to some degree of the relative density after compaction, the contact cohesion and the standard deviation of the strain ratios during compaction (see Eq. (40) to Eq. (46)). The constants z_{max} and z_{min} describe the maximal extension of the yield surfaces along its rotation axis in positive and negative direction. The respective Eq. (40) and (41) have the same structure except that z_{min} includes the cohesion strength as it describes the extension of the yield surface for tension load. The parameters z_m and a describe the center and the semi-major axis of the ellipse shown in the first term of Eq. (37). The ratio of the major and the minor axes of the ellipse is given by the parameter q. The parameter k describes the slope of the linear equation of the second term in Eq. (37). The last parameter l is used in the third term of Eq. (37) and describes the difference of the ellipsoid's extension in r-direction. As l is zero in case of isostatic compaction and increases for anisotropic compaction it is a primary measure for the anisotropy of the yield surface in addition to the orientation of the rotation axis described in Eq. (38).

It would be fruitful to combine the regression equations of the observed yield surface given in Eq. (37) to (39) with the existing concepts of anisotropic plasticity [85,89] in the literature. However, we refrain from this step in the current work, as it was our goal to best fit the numerically obtained yield surface with flexible analytical equations which describe the anisotropy of the yield surface as a function of the condition of the compacted powder (relative density after compaction, the contact cohesion strength and the strain path during compaction). Our description of the yield surface in cylindrical coordinate systems directly follows from the visual inspection of the yield surface for different compaction conditions of the powder.

$$z_{max} = 3356 \cdot (\rho_{rel} - 0.6)^{1.79 - 0.1 \cdot std\left(\frac{\boldsymbol{e}}{\bar{e}}\right)} \cdot \left(1 - 0.16 \cdot std\left(\frac{\boldsymbol{e}}{\bar{e}}\right)^{0.86}\right) \tag{40}$$

$$z_{min} = -2097 \cdot (\rho_{rel} - 0.6)^{1.79 - 0.1 \cdot std\left(\frac{\boldsymbol{e}}{\bar{e}}\right)} \cdot \left(1 - 0.16 \cdot std\left(\frac{\boldsymbol{e}}{\bar{e}}\right)^{0.86}\right) \cdot \operatorname{atan}\left(\frac{c_{max}}{233}\right)^{1.54} \tag{41}$$

$$z_m = \frac{z_{max} + z_{min}}{2} \tag{42}$$

$$a = \frac{z_{max} - z_{min}}{2} \tag{43}$$

$$q = (2.28 + 7.93 \cdot (1 - \rho_{rel})^{2.05}) \cdot \left(1 + 0.146 \cdot std\left(\frac{\boldsymbol{e}}{\bar{e}}\right)^{0.558}\right) \tag{44}$$

$$k = (0.000447 + 4.98 \cdot 10^{-6} \cdot (\rho_{rel} - 0.6)^{-2.02}) \cdot \left(0.64 - atan\left(\frac{c_{max}}{176.1}\right)\right) \tag{45}$$

$$l = 0.154 \cdot \big(1 + 1.52 \cdot (1.52 - \rho_{rel})\big) \cdot (1 - 0.000256 \cdot coh) \cdot std\left(\frac{\boldsymbol{e}}{\bar{e}}\right)^{0.366} \tag{46}$$

4.5 Conclusion and Outlook

The elastic and plastic properties of compacted powders were investigated in this work during extensive simulation studies based on a MPFEM model including 50 particles in a periodic RVE. The RVE was compacted to different relative densities using different strain paths. Although the initial packing of the particles is random and isotropic, a clear anisotropy of the mechanical properties is observed after compaction. The simulations show a direct correlation of the anisotropy of the principal strains during compaction and the anisotropy of the elastic and plastic properties of the compacted powder. In case of isostatic compaction, the elastic and plastic properties are observed to be isotropic. If the compaction strain in one direction differs from the others, then also a different Young's modulus and yield strength is observed in this direction. A higher compaction strain results in a higher Young's modulus and yield strength, while the opposite is true for lower compaction strain. The properties of the directions with equal strain during compaction are identical leading to a transverse isotropic elastic material model. This is the case for the most often used closed-die compaction. It is therefore an oversimplification to use an isotropic material model for closed-die compaction, as it is widely done for tableting [51,96]. In case of three different compaction strains all three Young's moduli and uniaxial yield strengths are different, leading to an orthotropic elasticity model of the compacted powder. The yield surface, described as a rotated surface, shows the anisotropy of the yield properties as well. The rotational axis is not aligned with the space diagonal, but is rotated towards the direction of highest compaction strain. Furthermore, the yield surface is compressed in the direction of the smallest strain during compaction. The anisotropy is not solely a function of the strain path, but is also influenced by the relative density after compaction. The anisotropy is more important at low relative densities compared to high relative densities, since contact areas are particularly formed normal to the direction of the highest strain in case of low relative densities. This behavior was already reported in [59]. At high relative densities contact surfaces are increasingly formed parallel to the main compaction direction leading to smaller anisotropy.

The contact cohesion has a minor influence on the anisotropy of the compacted powder, but it has a major influence on the mechanical properties of the compacted powder in general. In case of very low contact cohesion the Young's modulus, the shear modulus and the uniaxial strength are negligibly small and the Poisson's ratio is close to 0.5. This indicates a pure plastic behavior of the powder rather than an elastic-plastic behavior. Only in case of a positive pressure noteworthy stresses can be applied to the cohesionless powder as can be seen in Figure 43. In case of cohesion strengths which are in the range or even above the yield strength of the particle material a clear elastic-plastic behavior of the compacted powder can be observed. The powder can furthermore take up substantial tensile load, leading to yield surfaces which are equally extended for positive and negative pressure.

This work clearly reveals the need of an alternative yield surface for powder compaction as the most often used Drucker-Prager/Cap model (see Figure 35) is not able to describe the yield behavior of powders after compaction using different strain paths. Based on the regression equations shown in this work, it is possible to implement an anisotropic yield surface and elasticity model for a macroscopic FEM model of a powder compaction process in a future work. Since the relative density and the strain ratios during compaction are included in the regression equation they are useful to determine the distribution of the material properties of inhomogeneous compacted powder. This allows to model compaction of complex shapes of powder compacts and to model the deformation close to walls and corners. The variety of the contact cohesion strength can be used to model different contact properties, e.g., a low contact cohesion can be used to model cold compaction of powders with weak cohesion interaction and high contact cohesion can be used to model powders after sintering.

Despite the considerable possibilities of the demonstrated model additional improvements are suggested for future work. First of all, it is necessary to adapt the contact model to enhance the physical interpretation of parameters in the modeled contact between particles. To enable comparability to a real powder it will be necessary to use a proper particle size distribution and non-spherical particles. As there are many brittle particle materials it would be a valuable extension to include particle breakage into the model. Furthermore, the flow rule which describes the direction of the flow during yielding of the compacted powder needs to be considered. In case of solid metallic materials, it is often valid to assume plastic flow normal to the yield surface. This assumption is not necessarily applicable for compacted powders. Another different measure which can also be of interest is the fracture energy of the compacted powder. The fracture energy is an important quantity in fracture-mechanics analyses which may be employed during brittle fracture of the compacted powder.

Finally, the material models derived from our micromechanical model have to be implemented in a suitable subroutine of a FEM code (e.g., UMAT/VUMAT in Abaqus) to compute the stress distribution of whole powder parts during compaction and processing. In this way possible failures of the compacted powder can be predicted and process optimization can be performed.

5 Conclusion and Outlook

5.1 DEM Modeling of Powder Compaction

The work presented in section 2 has shown the qualitatively different behavior of free flowing and cohesive powder during the dosator process. The cohesive powders form a loose powder bed which can easily be compressed during dosing as particles only have to rearrange to get densified. The initial powder bed of free flowing powder is already densely packed and therefore the particles are just slightly compressed during dosing. As a consequence, the evolution of the powder mass inside the dosator is different for cohesive and for free flowing powder. To increase the practical applicability of the results in section 2 it is necessary to adjust the DEM contact model in such a way to describe the flow behavior of practical relevant powders quantitatively. Noteworthy effort was spent on contact model calibration at IPPE in the last years [98–100]. The authors use the design of experiments DoE approach to correlate the microscopic contact parameters of the contact models (contact stiffness, coefficient of friction, cohesion force, etc.) and the macroscopic powder properties (bulk density, compressibility, flowability, etc.). The macroscopic powder properties can be obtained during standard experimental tests and have to be reproduced during powder simulation. It is shown, that it is far more challenging to model cohesive powders than free flowing powders. It was not possible to model the measured compressibility and flowability of a certain powder with the same contact model parameters. Kottlan [100] refers this shortcut to the oversimplification of the DEM model which uses spheres to describe non-spherical particles. He proposes to use non-spherical particles to obtain more realistic DEM models.

The work of Madlmeir [101] succeeds the work described in section 2 and deals with the variation of process parameters which also have an influence on the density of the powder after dosing. He was able to qualitatively reproduce the behavior of the moderate cohesive powder Lactohale® 100 as a function of different process conditions. In his work it was also not possible to model strong cohesive powders sufficiently. For future investigations it is suggested to eliminate oversimplification of the DEM model by using non-spherical particles and a sufficient contact model. Only if the model is able to reproduce all important macroscopic powder properties, quantitative predictions based on DEM simulations can be expected.

5.2 MPFEM Modeling of Powder Compaction

The work in section 3 and the subsequent work in section 4 demonstrate the applicability of the proposed MPFEM model. It was possible to obtain elastic and plastic material properties based on a RVE of a small number of particles. The influence of the model parameters (relative density, contact cohesion strength and strain path during compaction) on the mechanical properties was observed. So far, the model is limited to particles which are spherical at the beginning of the compaction process and only deform plastically during compaction. To describe compaction of brittle materials it is necessary to model fracture of the particles. Therefore, a sufficient fracture criterion has to be included in the description of the particle material model and the MPFEM model has to consider the formation of new surfaces during cracking.

Another important step towards a more realistic model of powder compaction is to consider non-spherical particles. In principle the MPFEM method is not restricted to spherical particles since the particles are meshed. If it is possible to mesh a certain particle shape based on hexahedral or tetrahedral elements, then it can be used in the presented RVE. However, the RVE requires a densely packed initial powder bed which can easily be obtained from DEM simulations in case of spherical particles. It is much more challenging to get densely packed beds of non-spherical particles as it was shown by Segner [102] and Huber [103]. They used the glued-sphere approach to generate densely packed beds of non-spherical particles in DEM. The position and orientation of the particles in the DEM model were used to set up a RVE in a MPFEM model. This approach was optimized and applied for elongated particles in the subsequent work of Fiedler [104]. In this thesis similar convergence studies were performed as presented in section 3.3. Figure 45 shows for example a mesh convergence study of 50 elongated particles which are slightly twisted. It is more challenging to get representative properties in case of non-spherical particles than for spheres. Depending on the initial packing of the particles the mechanical properties of the compacted powder vary significantly. For this reason, RVEs consisting of non-spherical particles have to including a higher number of particles.

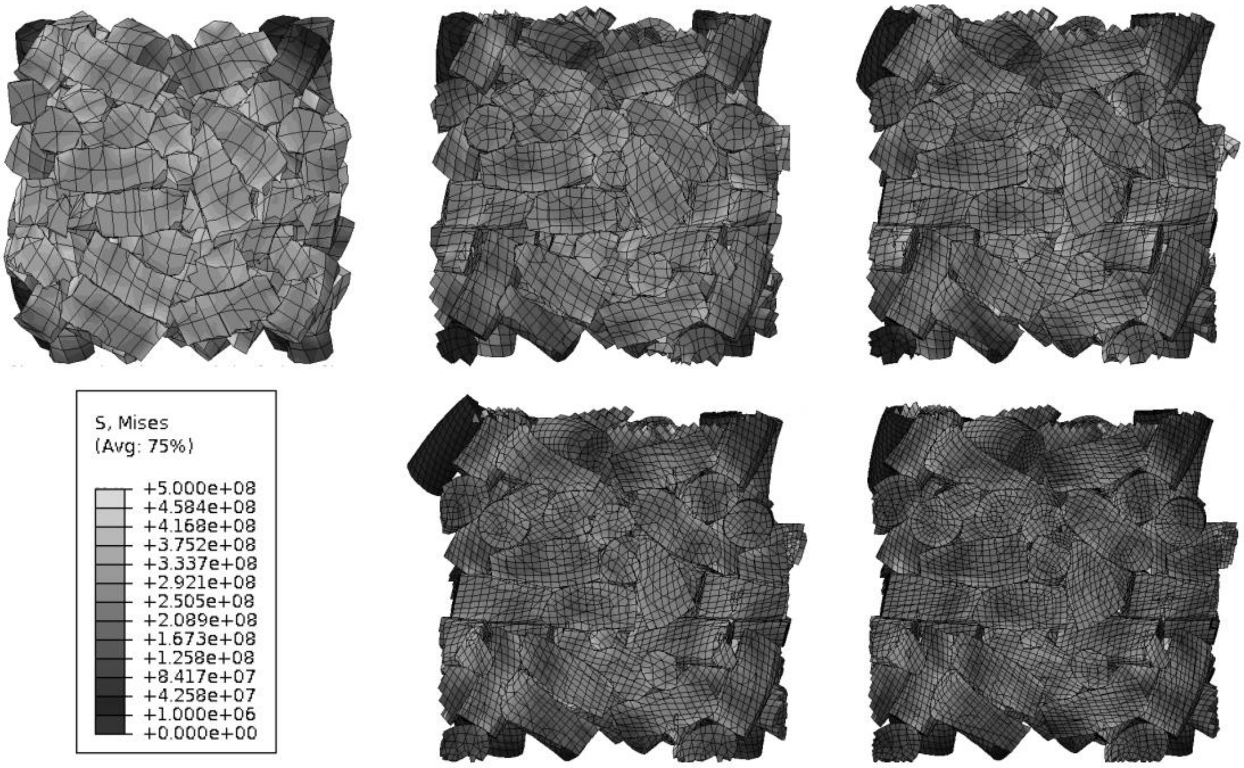

Figure 45: Convergence study of the mesh fineness for elongated particles *[104]*

Another challenge occurring for non-spherical particles is the additional effort required during meshing. The maximum size of the mesh elements must be substantially smaller than the smallest cross section of the particles. Hence, the number of elements needed to sufficiently mesh the particles increases with an increasing aspect ratio of the particles. This is especially problematic for thin needles or fibers. To circumvent this problem it would be beneficial to use

1D elements as it was done in [105]. In this way the particles are only discretized in longitudinal direction leading to significant lower computational costs.

One important aspect of the MPFEM model is the interaction of the particles as it was shown in section 3 and 4. The contact cohesion model is particularly important since it is the key factor to model tension strength of powders. The used cohesion model considers surface cohesion in a simplified fashion. The cohesion strength is used as a parameter to model the range from weak cohesion interaction between surfaces and practically bonded surfaces. Alternative contact models should be used to better reflect the behavior of real particles. First of all, the cohesion model should be adapted to the physical origin of the surface attraction (e.g. van der Waals interaction, solid bonding, etc.). Furthermore, additional phenomena as time-dependent and pressure-dependent cohesion forces should be considered. One step towards more realistic contact models was done in the work of Fiedler [106] and Gschiel [107] who implemented and tested different contact models which could be further used within an advanced MPFEM model.

The final goal of modeling powder compaction is to describe the behavior of whole powder parts of arbitrary shape. This is not possible by means of a MPFEM model, since the computational effort is far too high. Instead a continuum model has to be used which uses the macroscopic material properties obtained from the MPFEM model. Therefore, a sufficient user defined material model has to be implemented in a FEM code. This model has to describe the elastic and plastic deformation behavior on the one hand and has to consider possible brittle fracture of the compacted powder on the other hand. The elastic properties of spherical particles compacted to different relative densities by using different strain paths are already presented in section 4.3. According to this data, it is necessary to use an orthotropic elasticity model in the macroscopic model if general strain paths during compaction are considered. The continuum plasticity model has to take into account the onset of yielding for any loading direction based on a yield surface. The yield surface of powders with different contact cohesion and compaction conditions are already presented in section 4.4. The yield surfaces are not isotropic for general strain paths during compaction and their size and shape depends on the cohesion strength of the particle surfaces in contact. This has to be considered in a sufficient model for the yield surface. In addition to the yield surface which describes the onset of yielding, it is also necessary to define the flow potential which describes the direction of flow during plastic yielding. One possibility is to assume a flow direction normal to the yield surface. This normality rule is usually applied in case of metallic materials, but it is not generally accepted for compacted powder. A small number of trail simulations were conducted for this thesis to obtain the flow direction of the RVE. However, a clear answer regarding the applicability of the normality rule could not be obtained. A more comprehensive simulation study is necessary to get a clear statement of the flow potential of compacted powder. The last mechanism which has to be included in the continuum model is brittle fracture of the compacted powder. During fracture the compacted powder cleaves into two or more parts leading to the formation of new surface area. The energy needed to create new surface area is a measure for the resistance of a material against brittle fracture. This fracture energy could be determined based on the RVE considered in this work by simply pulling apart the RVE of compacted powder and calculate the energy needed to completely separate the fracture area. It is supposed to obtain anisotropic fracture energy after anisotropic compaction similarly as it was observed for the Young's modulus and the yield strength in section 4.3 and 4.4.

One important step in modeling was not addressed in this thesis as no effort was spent on model validation. Model validation has to be performed on the micro and the macro scale. On the micro scale the properties of the particles and their interaction have to be addressed. The material model of the particle has to reflect correctly the deformation behavior of the particles. The contact model has to be adapted for the specific material system. Only if the micromechanics of the MPFEM model reflect the real system it makes sense to make a validation on the macro scale. Since the model so far is only sufficiently tested for spherical particles which deform plastically the validation has to be performed for such an idealized system. Validation on the macro scale means to compare the homogenized quantities of the MPFEM model with real experiments. In these experiments at least, the Young’s modulus and the uniaxial yield strength should be determined as function of the relative density of the powder.

6 Literature

[1] P. Kelly, Anisotropic Elasticity, Solid Mech. Part I An Introd. to Solid Mech. (2014) 1–83. doi:10.1016/B978-0-12-374446-3.50015-7.

[2] D.C. Drucker, W. Prager, Soil Mechanics and Plastic Analysis or Limit Design, Q. Appl. Math. 10 (1952) 157–165. doi:10.1090/qam/48291.

[3] E. Faulhammer, M. Llusa, C. Radeke, O. Scheibelhofer, S. Lawrence, S. Biserni, V. Calzolari, J.G. Khinast, The effects of material attributes on capsule fill weight and weight variability in dosator nozzle machines., Int. J. Pharm. 471 (2014) 332–8. doi:10.1016/j.ijpharm.2014.05.058.

[4] F. Podczeck, S. Blackwell, M. Gold, J.M. Newton, The filling of granules into hard gelatine capsules, Int. J. Pharm. 188 (1999). doi:10.1016/S0378-5173(99)00208-2.

[5] A. Pinzon, Modelling of Dosator Filling and Discharge, Greenwich Acad. Lit. Arch. - Univ. Og Greenwich Open Access Repos. (2012).

[6] M.O. Besenhard, E. Faulhammer, S. Fathollahi, G. Reif, V. Calzolari, S. Biserni, A. Ferrari, S.M. Lawrence, M. Llusa, J.G. Khinast, Accuracy of micro powder dosing via a vibratory sieve-chute system, Eur. J. Pharm. Biopharm. 94 (2015) 264–272. doi:10.1016/j.ejpb.2015.04.037.

[7] M.O. Besenhard, S.K. Karkala, E. Faulhammer, S. Fathollahi, R. Ramachandran, J.G. Khinast, Continuous feeding of low-dose APIs via periodic micro dosing, Int. J. Pharm. 509 (2016) 123–134. doi:10.1016/j.ijpharm.2016.05.033.

[8] B. Jones, The filling of powders into two-piece hard capsules, Int. J. Pharm. 227 (2001) 5–26. doi:10.1016/S0378-5173(01)00781-5.

[9] S.B. Tan, J.M. Newton, Minimum compression stress requirements for arching and powder retention within a dosator nozzle during capsule filling, Int. J. Pharm. 63 (1990) 275–280. doi:10.1016/0378-5173(90)90134-P.

[10] E. Faulhammer, M. Fink, M. Llusa, S.M. Lawrence, S. Biserni, V. Calzolari, J.G. Khinast, Low-dose capsule filling of inhalation products: critical material attributes and process parameters., Int. J. Pharm. 473 (2014) 617–26. doi:10.1016/j.ijpharm.2014.07.050.

[11] I.G. Jolliffe, J.M. Newton, The effect of dosator nozzle wall texture on capsule filling with the MG2 simulator, J. Pharm. Pharmacol. 35 (1983) 7–11. doi:10.1111/j.2042-7158.1983.tb04253.x.

[12] R. Patel, F. Podczeck, Investigation of the effect of type and source of microcrystalline cellulose on capsule filling, Int. J. Pharm. 128 (1996) 123–127. doi:10.1016/0378-5173(95)04231-8.

[13] F. Podczeck, J.M. Newton, Powder filling into hard gelatine capsules on a tamp filling machine, Int. J. Pharm. 185 (1999) 237–254. doi:10.1016/S0378-5173(99)00169-6.

[14] F. Podczeck, J.M. Newton, Powder and capsule filling properties of lubricated granulated cellulose powder, Eur. J. Pharm. Biopharm. 50 (2000) 373–377. doi:10.1016/S0939-6411(00)00100-4.

[15] M. Llusa, E. Faulhammer, S. Biserni, V. Calzolari, S. Lawrence, M. Bresciani, J. Khinast, The effect of capsule-filling machine vibrations on average fill weight., Int. J. Pharm. 454 (2013) 381–7. doi:10.1016/j.ijpharm.2013.07.029.

[16] C. Bierwisch, T. Kraft, H. Riedel, M. Moseler, Die filling optimization using three-dimensional discrete element modeling, Powder Technol. 196 (2009) 169–179. doi:10.1016/j.powtec.2009.07.018.

[17] Y. Tsunazawa, Y. Shigeto, C. Tokoro, M. Sakai, Numerical simulation of industrial die filling using the discrete element method, Chem. Eng. Sci. 138 (2015) 791–809. doi:10.1016/j.ces.2015.09.014.

[18] Y. Guo, C.Y. Wu, Computational modeling of pharmaceutical die filling processes, Predict. Model. Pharm. Unit Oper. (2016) 253–271. doi:10.1016/B978-0-08-100154-

7.00011-9.

[19] O.I. Imole, D. Krijgsman, T. Weinhart, V. Magnanimo, B.E. Chavez Montes, M. Ramaioli, S. Luding, Experiments and discrete element simulation of the dosing of cohesive powders in a simplified geometry, Powder Technol. 287 (2016) 108–120. doi:10.1016/j.powtec.2015.07.051.

[20] I.G. Jolliffe, J.M. Newton, J.K. Walters, Theoretical Considerations of the Filling of Pharmaceutical Hard Gelatine Capsules, Powder Technol. 27 (1980) 189–195.

[21] A. Khawam, Modeling powder encapsulation in dosator-based machines: I. Theory., Int. J. Pharm. 421 (2011) 203–9. doi:10.1016/j.ijpharm.2011.10.021.

[22] R.C. Rowe, P. York, E. a Colbourn, S.J. Roskilly, The influence of pellet shape, size and distribution on capsule filling--a preliminary evaluation of three-dimensional computer simulation using a Monte-Carlo technique., Int. J. Pharm. 300 (2005) 32–7. doi:10.1016/j.ijpharm.2005.05.007.

[23] A.M. Ali, M. de Matas, P. York, R.C. Rowe, Influence of pellet aggregate populations on the variability of pellet filling into hard shell capsules: a comparison of experiment and computer simulation., Eur. J. Pharm. Sci. 38 (2009) 197–205. doi:10.1016/j.ejps.2009.07.001.

[24] P.A. Cundall, O.D.L. Strack, A discrete numerical model for granular assemblies, Géotechnique. 29 (1979) 47–65. doi:10.1680/geot.1979.29.1.47.

[25] C. Kloss, C. Goniva, A. Hager, S. Amberger, S. Pirker, Models , algorithms and validation for opensource DEM and CFD-DEM, Pcfd. 12 (2012) 140–152. doi:10.1504/PCFD.2012.047457.

[26] R.J. Roberts, R.C. Rowe, The relationship between Young's modulus of elasticity of organic solids and their molecular structure, Powder Technol. 65 (1991) 139–146. doi:10.1016/0032-5910(91)80176-J.

[27] C. Kloss, LIGGGHTS(R)-PUBLIC Documentation, Version 3.X, (2016).

http://www.cfdem.com/media/DEM/docu/Manual.html.

[28] A. Baldelli, R. Vehring, Analysis of cohesion forces between monodisperse microparticles with rough surfaces, Colloids Surfaces A Physicochem. Eng. Asp. 506 (2016) 179–189. doi:10.1016/j.colsurfa.2016.06.009.

[29] R.P. Zou, A.B. Yu, The packing of spheres in a cylindrical container: the thickness effect, Chem. Eng. Sci. 50 (1995) 1504–1507. doi:10.1016/0009-2509(94)00483-8.

[30] M. Suzuki, T. Shinmura, K. Iimura, M. Hirota, Study of the Wall Effect on Particle Packing Structure Using X-ray Micro Computed Tomography, Adv. Powder Technol. 19 (2008) 183–195. doi:10.1163/156855208X293817.

[31] S. Inghelbrecht, J.P. Remon, Roller compaction and tableting of microcrystalline cellulose/drug mixtures, Int. J. Pharm. 161 (1998) 215–224. doi:10.1016/S0378-5173(97)00356-6.

[32] S.C. Lee, K.T. Kim, Densification behavior of aluminum alloy powder under cold compaction, Int. J. Mech. Sci. 44 (2002) 1295–1308.

[33] M. Trunec, K. Maca, Compaction and pressureless sintering of zirconia nanoparticles, J. Am. Ceram. Soc. 90 (2007) 2735–2740. doi:10.1111/j.1551-2916.2007.01781.x.

[34] W.R. Mitchell, L. Forny, T. Althaus, D. Dopfer, G. Niederreiter, S. Palzer, Compaction of food powders: The influence of material properties and process parameters on product structure, strength, and dissolution, Chem. Eng. Sci. 167 (2017) 29–41. doi:10.1016/j.ces.2017.03.056.

[35] R.W. Heckel, Density-Pressure Relationships in Powder Compaction, Trans. Metall. Soc. AIME. 221 (1961) 671–675.

[36] K. Kawakita, K.-H. Lüdde, Some considerations on powder compression equations, Powder Technol. 4 (1971) 61–68. doi:10.1016/0032-5910(71)80001-3.

[37] V. Mazel, V. Busignies, S. Duca, B. Leclerc, P. Tchoreloff, Original predictive approach to the compressibility of pharmaceutical powder mixtures based on the Kawakita

equation, Int. J. Pharm. 410 (2011) 92–98. doi:10.1016/j.ijpharm.2011.03.027.

[38] A.S. Persson, J. Nordström, G. Frenning, G. Alderborn, Compression analysis for assessment of pellet plasticity: Identification of reactant pores and comparison between Heckel, Kawakita, and Adams equations, Chem. Eng. Res. Des. 110 (2016) 183–191. doi:10.1016/j.cherd.2016.01.028.

[39] S. Paul, C.C. Sun, The suitability of common compressibility equations for characterizing plasticity of diverse powders, Int. J. Pharm. 532 (2017) 124–130. doi:10.1016/j.ijpharm.2017.08.096.

[40] E. Ryshkewitch, Compression Strength of Porous Sintered Alumina and Zirconia, J. Am. Ceram. Soc. 36 (1953) 65–68. doi:10.1111/j.1151-2916.1953.tb12837.x.

[41] K.J. Wilkinson, A. Reinhardt, A simple predictive model for the tensile strength of binary tablets, (2005). doi:10.1016/j.egypro.2016.11.209.

[42] A. Michrafy, M. Michrafy, M.S. Kadiri, J.A. Dodds, Predictions of tensile strength of binary tablets using linear and power law mixing rules, Int. J. Pharm. 333 (2007) 118–126. doi:10.1016/j.ijpharm.2006.10.008.

[43] N.A. Fleck, L.T. Kuhn, R.M. McMeeking, Yielding of metal powder bonded by isolated contacts, J. Mech. Phys. Solids. 40 (1992) 1139–1162. doi:10.1016/0022-5096(92)90064-9.

[44] N.A. Fleck, On the cold compaction of powders, J. Mech. Phys. Solids. 43 (1995) 1409–1431. doi:10.1016/0022-5096(95)00039-L.

[45] E. Arzt, The influence of an increasing particle coordination on the densification of spherical polders, Acta Metall. 30 (1982) 1883–1890. doi:10.1016/0001-6160(82)90028-1.

[46] A.T. Procopio, A. Zavaliangos, Simulation of multi-axial compaction of granular media from loose to high relative densities, J. Mech. Phys. Solids. 53 (2005) 1523–1551. doi:10.1016/j.jmps.2005.02.007.

[47] B. Harthong, J.-F. Jérier, P. Dorémus, D. Imbault, F.-V. Donzé, Modeling of high-density compaction of granular materials by the Discrete Element Method, Int. J. Solids Struct. 46 (2009) 3357–3364. doi:10.1016/j.ijsolstr.2009.05.008.

[48] J.-F. Jerier, B. Hathong, V. Richefeu, B. Chareyre, D. Imbault, F.-V. Donze, P. Doremus, Study of cold powder compaction by using the discrete element method, Powder Technol. 208 (2011) 537–541. doi:10.1016/j.powtec.2010.08.056.

[49] Y. He, Z. Wang, T.J. Evans, A.B. Yu, R.Y. Yang, DEM study of the mechanical strength of iron ore compacts, Int. J. Miner. Process. 142 (2015) 73–81. doi:10.1016/j.minpro.2015.05.005.

[50] A.S. Persson, G. Frenning, An experimental evaluation of discrete element simulations of confined powder compression using an extended truncated-sphere model, Powder Technol. 284 (2015) 257–264. doi:10.1016/j.powtec.2015.06.053.

[51] L.H. Han, J.A. Elliott, A.C. Bentham, A. Mills, G.E. Amidon, B.C. Hancock, A modified Drucker-Prager Cap model for die compaction simulation of pharmaceutical powders, Int. J. Solids Struct. 45 (2008) 3088–3106. doi:10.1016/j.ijsolstr.2008.01.024.

[52] T. Sinha, R. Bharadwaj, J.S. Curtis, B.C. Hancock, C. Wassgren, Finite element analysis of pharmaceutical tablet compaction using a density dependent material plasticity model, Powder Technol. 202 (2010) 46–54. doi:10.1016/j.powtec.2010.04.001.

[53] A. Mazor, L. Perez-Gandarillas, A. de Ryck, A. Michrafy, Effect of roll compactor sealing system designs: A finite element analysis, Powder Technol. 289 (2016) 21–30. doi:10.1016/j.powtec.2015.11.039.

[54] K.H. Roscoe, J.B. Burland, On the generalized stress-strain behavior of wet clay, Eng. Plast. (1968) 535–609. doi:10.1016/0022-4898(70)90160-6.

[55] H. Diarra, V. Mazel, V. Busignies, P. Tchoreloff, Comparative study between Drucker-Prager/Cap and modified Cam-Clay models for the numerical simulation of die compaction of pharmaceutical powders, Powder Technol. 320 (2017) 530–539.

doi:10.1016/j.powtec.2017.07.077.

[56] V.S. Deshpande, N.A. Fleck, Isotropic constitutive models for metallic foams, J. Mech. Phys. Solids. 48 (2000) 1253–1283. doi:10.1016/S0022-5096(99)00082-4.

[57] V.S. Deshpande, N.A. Fleck, Multi-axial yield behaviour of polymer foams, Acta Mater. 49 (2001) 1859–1866. doi:10.1016/S1359-6454(01)00058-1.

[58] A.L. Gurson, Continuum Theory of Ductile Rupture by Void Nucleation and Growth: Part I—Yield Criteria and Flow Rules for Porous Ductile Media, J. Eng. Mater. Technol. 99 (1977) 2. doi:10.1115/1.3443401.

[59] B. Harthong, D. Imbault, P. Dorémus, The study of relations between loading history and yield surfaces in powder materials using discrete finite element simulations, J. Mech. Phys. Solids. 60 (2012) 784–801. doi:10.1016/j.jmps.2011.11.009.

[60] G. Gustafsson, H.Å. Häggblad, P. Jonsén, Multi-particle finite element modelling of the compression of iron ore pellets with statistically distributed geometric and material data, Powder Technol. 239 (2013) 231–238. doi:10.1016/j.powtec.2013.02.005.

[61] P. Han, X. An, Y. Zhang, F. Huang, T. Yang, H. Fu, X. Yang, Z. Zou, Particulate scale MPFEM modeling on compaction of Fe and Al composite powders, Powder Technol. 314 (2017) 69–77. doi:10.1016/j.powtec.2016.11.021.

[62] N. Abdelmoula, B. Harthong, D. Imbault, P. Dorémus, A study on the uniqueness of the plastic flow direction for granular assemblies of ductile particles using discrete finite-element simulations, J. Mech. Phys. Solids. 109 (2017) 142–159. doi:10.1016/j.jmps.2017.07.021.

[63] S. Saeb, P. Steinmann, A. Javili, Aspects of Computational Homogenization at Finite Deformations: A Unifying Review From Reuss' to Voigt's Bound, Appl. Mech. Rev. 68 (2016) 050801. doi:10.1115/1.4034024.

[64] R. Hill, Elastic properties of reinforced solids: Some theoretical principles, J. Mech. Phys. Solids. 11 (1963) 357–372. doi:10.1016/0022-5096(63)90036-X.

[65] I.M. Gitman, H. Askes, L.J. Sluys, Representative volume: Existence and size determination, Eng. Fract. Mech. 74 (2007) 2518–2534. doi:10.1016/j.engfracmech.2006.12.021.

[66] K.K. Mandadapu, A. Sengupta, P. Papadopoulos, A homogenization method for thermomechanical continua using extensive physical quantities, Proc. R. Soc. A Math. Phys. Eng. Sci. 468 (2012) 1696–1715. doi:10.1098/rspa.2011.0578.

[67] C. Miehe, J. Dettmar, D. Zäh, Homogenization and two-scale simulations of granular materials for different microstructural constraints, Int. J. Numer. Methods Eng. 83 (2010) 1206–1236. doi:10.1002/nme.2875.

[68] C. Miehe, J. Dettmar, D. Zäh, Homogenization and Multiscaling of granular Media for Different Microscopic Constraints, Multiscale Methods Comput. Mech. (2011) 155–177. doi:https://doi.org/10.1007/978-90-481-9809-2_9.

[69] J. Liu, E. Bosco, A.S.J. Suiker, Formulation and numerical implementation of micro-scale boundary conditions for particle aggregates, Granul. Matter. 19 (2017). doi:10.1007/s10035-017-0757-y.

[70] A. Javili, S. Saeb, P. Steinmann, Aspects of implementing constant traction boundary conditions in computational homogenization via semi-Dirichlet boundary conditions, Comput. Mech. 59 (2017) 21–35. doi:10.1007/s00466-016-1333-8.

[71] © Dassault Systèmes, Abaqus 6.14 Online Documentation, (2014). http://130.149.89.49:2080/v6.14/index.html.

[72] I. Schmidt, A. Trondl, T. Kraft, A. Wonisch, Simulation of the material behaviour of metal powder during compaction, Proc. Inst. Mech. Eng. Part E-Journal Process Mech. Eng. 224 (2010) 187–194. doi:10.1243/09544089jpme325.

[73] Z. Yuan, J. Fish, Toward realization of computational homogenization in practice, Int. J. Numer. Methods Eng. 73 (2008) 361–380. doi:10.1002/nme.

[74] K. Schneider, K. Benjamin, S. Bargmann, Fully periodic RVEs for technological

relevant composites: Not worth the effort, J. Mech. Mater. Struct. 12 (2017).

[75] W.J. Chung, J.W. Cho, T. Belytschko, On the dynamic effects of explicit FEM in sheet metal forming analysis, Eng. Comput. 15 (1998) 750–776. doi:10.1108/02644409810231880.

[76] S.F. Miller, A.J. Shih, Thermo-Mechanical Finite Element Modeling of the Friction Drilling Process, J. Manuf. Sci. Eng. 129 (2007) 531. doi:10.1115/1.2716719.

[77] F. Ducobu, E. Rivière-Lorphèvre, E. Filippi, On the introduction of adaptive mass scaling in a finite element model of Ti6Al4V orthogonal cutting, Simul. Model. Pract. Theory. 53 (2015) 1–14. doi:10.1016/j.simpat.2015.02.003.

[78] J.E. Flinn, D.P. Field, G.E. Korth, T.M. Lillo, J. Macheret, The flow stress behavior of OFHC polycrystalline copper, Acta Mater. 49 (2001) 2065–2074. doi:10.1016/S1359-6454(01)00102-1.

[79] M.H. Shih, C.Y. Yu, P.W. Kao, C.P. Chang, Microstructure and flow stress of copper deformed to large plastic strains, Scr. Mater. 45 (2001) 793–799. doi:10.1016/S1359-6462(01)01098-3.

[80] A.R. Akisanya, T. Street, The yield behaviour of metal powders, 39 (1997) 1315–1324.

[81] S. Galen, A. Zavaliangos, Strength anisotropy in cold compacted ductile and brittle powders, Acta Mater. 53 (2005) 4801–4815. doi:10.1016/j.actamat.2005.06.023.

[82] C.A. Radeke, B.J. Glasser, J.G. Khinast, Large-scale powder mixer simulations using massively parallel GPUarchitectures, Chem. Eng. Sci. 65 (2010) 6435–6442. doi:10.1016/j.ces.2010.09.035.

[83] P. Loidolt, S. Madlmeir, J.G. Khinast, Mechanistic modeling of a capsule filling process, Int. J. Pharm. 532 (2017) 47–54. doi:10.1016/j.ijpharm.2017.08.125.

[84] J.C. Simo, T.J.R. Hughes, Computational Inelasticity, Springer Verlag New York, 1998.

[85] R. Hill, The Mathematical Theory of Plasticity, Oxford University Press, 1950.

[86] R.M. Caddell, R.S. Raghava, A.G. Atkins, A yield criterion for anisotropic and pressure

dependent solids such as oriented polymers, J. Mater. Sci. (1973). doi:10.1007/BF00754900.

[87] V.S. Deshpande, N.A. Fleck, M.F. Ashby, Effective properties of the octet-truss lattice material, J. Mech. Phys. Solids. 49 (2001) 1747–1769. doi:10.1016/S0022-5096(01)00010-2.

[88] Z. Xue, J.W. Hutchinson, Constitutive model for quasi-static deformation of metallic sandwich cores, Int. J. Numer. Methods Eng. 61 (2004) 2205–2238. doi:10.1002/nme.1142.

[89] F. Barlat, D.J. Lege, J.C. Brem, A six-component yield function for anisotropic materials, Int. J. Plast. (1991). doi:10.1016/0749-6419(91)90052-Z.

[90] F. Bron, J. Besson, A yield function for anisotropic materials Application to aluminum alloys, Int. J. Plast. 20 (2004) 937–963. doi:10.1016/j.ijplas.2003.06.001.

[91] F. Barlat, J.W. Yoon, O. Cazacu, On linear transformations of stress tensors for the description of plastic anisotropy, Int. J. Plast. 23 (2007) 876–896. doi:10.1016/j.ijplas.2006.10.001.

[92] F. Yoshida, H. Hamasaki, T. Uemori, A user-friendly 3D yield function to describe anisotropy of steel sheets, Int. J. Plast. 45 (2013) 119–139. doi:10.1016/j.ijplas.2013.01.010.

[93] J.W. Yoon, Y. Lou, J. Yoon, M. V. Glazoff, Asymmetric yield function based on the stress invariants for pressure sensitive metals, Int. J. Plast. 56 (2014) 184–202. doi:10.1016/j.ijplas.2013.11.008.

[94] H. Altenbach, A. Öchsner, eds., Plasticity of Pressure-Sensitive Materials, Springer Verlag Heidelberg, 2014.

[95] P. Loidolt, M.H. Ulz, J. Khinast, Modeling yield properties of compacted powder using a multi-particle finite element model with cohesive contacts, Powder Technol. 336 (2018) 426–440. doi:10.1016/j.powtec.2018.06.018.

[96] I.C. Sinka, J.C. Cunningham, A. Zavaliangos, The effect of wall friction in the compaction of pharmaceutical tablets with curved faces: A validation study of the Drucker-Prager Cap model, Powder Technol. 133 (2003) 33–43. doi:10.1016/S0032-5910(03)00094-9.

[97] C. Wu, Continuum Mechanics and Plasticity, Chapman & Hall/CRC, Boca Raton, USA, 2005.

[98] A. Bramböck, Calibration of DEM Simulation Parameter by Standardized Experiments, Graz University of Technology, 2016.

[99] A. Bramböck, Correlation of Bulk Properties and DEM Contact Models for Cohesive Powders, Graz University of Technology, 2017.

[100] A. Kottlan, DEM Contact Model Parameter Calibration based on Experimental Bulk Property Analysis, Graz University of Technology, 2018.

[101] S. Madlmeir, DEM simulation of the dosator capsule filling process, Graz University of Technology, 2018.

[102] G. Segner, Generieren dichter Packungen von verschieden förmiger Partikeln mit der DEM-Methode, Graz University of Technology, 2017.

[103] R. Huber, Modellierung und Vernetzung von Laktose- und Zellulosepartikeln für die Multiple-, Graz University of Technology, 2017.

[104] D. Fiedler, Simulation of compaction behaviour of non-spherical particles with Multi Particle Finite Element Method, Graz University of Technology, 2018.

[105] U. Kaindlbauer, Modellierung von faserförmigen Partikeln mittels 1D Elemente in Abaqus/CAE, Graz University of Technology, 2018.

[106] D. Fiedler, Implementation of Contact Model Subroutines in Abaqus / CAE, Graz University of Technology, 2017.

[107] M. Gschiel, Review and Verification of Contact Model Subroutines and Parameter Study in Abaqus/CAE and Matlab, Graz University of Technology, 2018.

7 Research Output

Publications in refereed journals:

- P. Loidolt, S. Madlmeir, J. G. Khinast, Mechanistic modeling of a capsule filling process. International Journal of Pharmaceutics, Volume 532, Issue 1, 30 October 2017, Pages 47-54
- P. Loidolt, M. H. Ulz, J. G. Khinast, Modeling yield properties of compacted powder using a multi-particle finite element model with cohesive contacts. Powder Technology, Volume 336, August 2018, Pages 426-440
- P. Loidolt, M. H. Ulz, J. G. Khinast, Prediction of the anisotropic mechanical properties of compacted powders. Powder Technology, Submitted July 2018
- S. Madlmeir, P. Loidolt, J. G. Khinast, Investigation of the dosator process for capsule filling with calibrated DEM simulation, in preparation

Conference talks:

- P. Loidolt, M. H. Ulz, J. G. Khinast, Multi-particle finite element method of powder compaction, 12th Minisymposium Verfahrenstechnik, Graz 2016
- P. Loidolt, J. G. Khinast, Mechanistic Modeling of Capsule Filling Processes, PARTEC conference, Nürnberg 2016
- P. Loidolt, J. G. Khinast, Anisotropic Mechanical Properties of Compacted Powders with Cohesive Contacts, AIChE Annual Meeting 2018, Pittsburgh 2018, accepted

Master's thesis (supervised):

- A. Bramböck, Correlation of Bulk Properties and DEM Contact Models for Cohesive Powders, Graz University of Technology, Graz 2017
- S. Madlmeir, DEM simulation of the dosator process for capsule filling, Graz University of Technology, Graz 2018
- D. Fiedler, Simulation of compaction behaviour of non-spherical particles with Multi Particle Finite Element Method, Graz University of Technology, Graz 2018
- A. Kottlan, DEM Contact Model Parameter Calibration based on Experimental Bulk Property Analysis, Graz University of Technology, Graz 2018

Bachelor’s thesis and project thesis (supervised):

- A. Bramböck, Calibration of DEM Simulation Parameter by Standardized Experiments, Graz University of Technology, Graz 2016
- D. Fiedler, Implementation of Contact Model Subroutines in Abaqus/CAE, Graz University of Technology, Graz 2017
- G. Segner, Generieren dichter Packungen von verschieden förmiger Partikeln mit der DEM-Methode, Graz University of Technology, Graz 2017
- L. Puttinger, Investigation of the Elastic Properties of Compacted Powder using a Multi Particle Finite Element Model, Graz University of Technology, Graz 2017
- R. Huber, Modellierung und Vernetzung von Laktose- und Zellulosepartikeln für die Multiple-Partikel-Finite-Elemente-Methode, Graz University of Technology, Graz 2017
- S. Rustige, Regression of 2D and 3D Yieldpoints of Powder Compaction Simulations, Graz University of Technology, Graz 2017
- M. Gschiel, Review of Contact Model Subroutines and Parameter Study in Abaqus/CAE and Matlab, Graz University of Technology, Graz 2018
- U. Kaindlbauer, Modellierung von faserförmigen Partikeln mittels 1D Elemente in Abaqus/CAE, Graz University of Technology, Graz 2018